Monitoring glacier parameters on the Antarctic Peninsula

- a centerline approach combining satellite and GIS data -

Thesis submitted in partial fulfillment of the requirements of

the degree Doctor rer. nat. of the

Faculty of Forest and Environmental Sciences,

Albert-Ludwigs-Universität

Freiburg im Breisgau, Germany

submitted by

Jorge Arigony Neto

from Porto Alegre (Brazil)

Freiburg im Breisgau

2006

Dean:	Prof. Dr. Heinz Rennenberg
Supervisor:	Prof. Dr. Hermann Goßmann
2nd Reviewer:	Prof. Dr. Barbara Koch

Date of thesis' defense: 31 January 2007

Acknowledgements

This work is made possible by a four-year grant from the Brazilian National Council for Scientific and Technological Development (CNPq, process 290015/02-2). Furthermore, many people helped me along this journey, and I wish to express my gratitude to all of you:

My supervisor, Professor Hermann Goßmann, for always encouraging me and for his confidence in my ability in carrying out an autonomous work. Dr. Helmut Saurer has given me the opportunity for developing the subject of this thesis. Additionally, his friendly comments and constructive criticism on my work were invaluable for the improvement of this thesis.

I owe my warmest gratitude to my colleagues Ricardo, Frank and Steffen, for many fruitful scientific discussions or simply for finding time to have a coffee or a beer. Frank's knowledge in SAR and remote sensing in general, together with his openness for discussions were quite useful in all moments of my work. In special, I would like to say *muchas gracias* to my officemate Ricardo and his family, Ingrid, Renate and Gabriel, for the fantastic moments we have spent together.

Still at IPG I also warmly thank: Susana and Angelica who always helped me to solve small problems, Dr. Klaus Braun who maintained the computer network, and all Professors and colleagues who contributed for a good atmosphere at the institute.

I could not forget to say many thanks to Professor Jefferson Simões and his determined efforts for building the first Brazilian research group on glaciology. He was always in touch and kept me motivated for the future, and also supported my attendance of international conferences. My extensive thanks to all Brazilian

colleagues at NUPAC. In particular to Ronaldo, Rafael Cabelo, Ulisses, Chico, Candida, Rose, Claudinha, Charlote, Dani and Siclério.

Several institutions supported me in many ways: the German Academic Exchange Service gave me the opportunity to learn German; the German Federal Agency for Cartography and Geodesy kindly make available some Landsat TM scenes; the European Space Agency supplied ERS-1/2 and ENVISAT ASAR data within the CryoSat Data AO Project 2658, "Evaluating Cryosat's potential contribution to the quantification of mass balance and mass balance variations on the Antarctic Peninsula", and supported a conference attendance in Beijing; the National Snow and Ice Data Center at the University of Colorado and the Inter-American Institute for Global Change Research also supported my attendance to conferences in Boulder and Beijing respectively.

I am grateful to many friends in Germany for the unforgettable moments, but I will not list names here because I fear to forget someone. Also *muito obrigado* for my friends in Brazil, who despite of the distance were always in touch by email or phone.

Finally, I wish to express my deepest gratitude to:

My mother Magali, my sisters Melisa and Milene, and my brother Diego. As well as to my grandparents Elio and Vilma. Thank you for believing in me, and continuously supporting my initiatives.

My wife and best friend, Mix, who offered her love and support every day. I could not have done it without you. Thank you for being there for me during all beautiful and difficult moments of living abroad.

Abstract

Drastic changes were detected in glacial systems of the Antarctic Peninsula in the last decades. The observed phenomena comprise a significant warming trend, changes in precipitation patterns, reduction of seasonal sea ice, disintegration of ice shelves, retreat of glacier fronts, upward shift of the dry snow line, and increasing trend in duration of melting conditions. Although the time response of such processes to climate change remains uncertain, the dependence of the detected glacial changes on variations in climate parameters seems to be evident. However, due to the lack of consistent systematic observations in particular of the higher parts of the glacial systems, it is difficult to predict further responses of glaciers to climate change.

This thesis focuses on the development of methods for semi-automatic extraction of glacier parameters (i.e., boundaries between glacier zones and glacier frontal position) on the Antarctic Peninsula using multi-temporal and multi-sensor remote sensing datasets. To expand the current monitoring of a few glaciers unevenly distributed along the peninsula to a representative set in the near future, a new methodological approach is proposed. The so-called centerline approach simplifies the current methodology based on analyses of entire glacier catchments, facilitating the pre-processing and classification of remote sensing data acquired on glaciers.

A multi-sensor processing chain to extract the above mentioned glacier parameters from satellite imagery using the centerline approach is described. Routines are implemented to reduce the analyst interaction with image processing

software and database system, resulting in an application called IceTools. In addition, the developed algorithms for the classification of SAR (i.e., ERS-1/2 SAR and Envisat ASAR) and optical imagery (i.e., Landsat TM/ETM+ and Terra ASTER) are explained. The modular structure of the implemented processing chain enables an unproblematic integration of algorithms for classifying datasets from future sensors.

A preliminary analysis of spatial and temporal distribution of satellite derived glacier parameters on the Antarctic Peninsula shows that climate related boundaries between glacier zones (i.e., the dry snow line and the snow line) as well as glacier fronts have different spatial patterns of change on this region. These patterns vary within the covered time period of the study (1986-2005), confirming the assumption that changes in climatological and glaciological conditions on a relatively short time scale are usual for this region. Furthermore, the widespread persistence of a wet snow radar zone is proved even when the air temperature sinks below 0^{o}C. As a consequence it can be stated that simple models of snow melting or mass balance based on positive degree-days from temperature measured at nearby stations tend to underestimate the energy available for melting in the snow pack.

Zusammenfassung

An den Gletschersystemen der Antarktischen Halbinsel wurden in den letzten Jahrzehnten drastische Veränderungen festgestellt. Die beobachteten Phänomene umfassen einen signifikanten Erwärmungstrend, Veränderungen des Niederschlagsmusters, eine Verringerung der saisonalen Meereisbedeckung, den Zerfall von Schelfeisen, den Rückzug der Gletscherfronten, die Aufwärtsverlagerung der Trockenschneelinie und eine Verlängerung der Zeiträume mit Schneeschmelze. Auch wenn die Antwortzeiten der einzelnen Prozesse auf klimatische Veränderungen noch ungewiss sind, so ist die Abhängigkeit des Wandels glazialer Systeme von klimatischen Parametern unumstritten. Jedoch ist es aus Mangel an zuverlässigen klimatologischen Beobachtungen insbesondere für die höheren Lagen der Gletschersysteme schwer, die künftige Reaktion von Gletschern auf klimatische Veränderungen vorherzusagen.

Der Schwerpunkt dieser Dissertation liegt auf der Entwicklung von Methoden zur halbautomatischen Gewinnung von Gletscherparametern (Grenzen zwischen Gletscherzonen und Lage der Gletscherfront) anhand multitemporaler und multisensoraler Fernerkundungsdaten. Untersuchungsraum ist die Antarktische Halbinsel. Um das bisher gängige Monitoring von wenigen, auf die Halbinsel verstreute Gletscher auf eine repräsentative Anzahl zu erweitern, wird eine neue Methode, die sogenannte „centerline approach“, verwendet. Sie vereinfacht die Auswertung, die bisher auf der Analyse der ganzen Gletschereinzugsgebiete basierte, durch eine Konzentration auf die zentralen Längsbereiche der einzelnen Gletscher. Damit werden Vorverarbeitung und Klassifizierung der Fernerkundungsdaten erleichtert und die Voraussetzungen für eine Automatisierung geschaffen.

Eine Prozessierungskette für die Extraktion der oben erwähnten Gletscherparameter aus Satellitenbildern verschiedener Sensoren mit Hilfe des „centerline approach“ wird vorgestellt. Die zur Verringerung der Interaktion von Software und Auswerter nötigen Computerroutinen und ihre Implementation in der Applikation „IceTools“ werden beschrieben. Zusätzlich werden spezifische Algorithmen zur Klassifizierung von SAR (ERS-1/2 SAR und Envisat ASAR) und optischen Bildern (Landsat TM/ETM+ und Terra ASTER) diskutiert. Die modulare Struktur der Prozessierungskette ermöglicht die problemlose Erweiterung um Algorithmen zur Einbeziehung von zukünftigen Sensoren.

Eine erste Analyse der räumlichen und zeitlichen Verteilung der aus Satellitenbilder gewonnenen Gletscherparameter zeigt, dass im Untersuchungsgebiet die Grenzen zwischen den Gletscherzonen, d.h. die Trockenschneelinie und die Schneelinie, wie auch die jeweilige Lage der Gletscherfront unterschiedliche räumliche Veränderungsmuster aufweisen. Diese Muster variieren innerhalb des Untersuchungszeitraums (1986-2005) und bestätigen die Aussage, dass die in kurzen Zeiträumen ablaufende Veränderung der klimatischen und glaziologischen Bedingungen typisch für die Region ist.

Darüber hinaus wird belegt, dass die Verbreitung der Nassschneezone nicht an Temperaturen von 0°C und mehr gebunden ist. Das weist darauf hin, dass einfache Schneeschmelz- oder Massenbilanzmodelle, die aus Messwerten benachbarter Stationen positive Gradtagszahlen ableiten und damit die Schmelzbedingungen modellieren, eine Tendenz zur Unterschätzung der Schmelzmengen aufweisen.

Contents

Index of tables

Index of figures

Abbreviations

ADC	Analogue-to-digital converter
ADD	Antarctic Digital Database
ALOS	Advanced Land Observing Satellite
AMI	Active Microwave Instrument
AntPenDB	Antarctic Peninsula Glacier Database
AntSDI	Antarctic Spatial Data Infrastructure
AO	Announcement of Opportunity
AOI	Area Of Interest
AP	Antarctic Peninsula
ASAR	Advanced Synthetic Aperture Radar
ASTER	Advanced Spaceborn Thermal Emission and Reflection Radiometer
BAS	British Antarctic Survey
BEST	Basic Envisat (and ERS) SAR Toolbox
BIRZ	Bare Ice Radar Zone
BIOZ	Bare Ice Optical Zone
CBERS	China-Brazil Earth Resources Satellite
CCRS	Canada Centre for Remote Sensing
CV	Coefficient of Variation
DEM	Digital Elevation Model
DLR	*Deutsches Zentrums für Luft- und Raumfahrt*
DN	Digital Number
DSRZ	Dry Snow Radar Zone
DSOZ	Dry Snow Optical Zone
ELA	Equilibrium Line Altitude

Envisat	Environmental Satellite
EOS	Earth Observation System
ERS-1/2	European Remote Sensing satellite
ERTS	Earth Resources Technology Satellite
ESA	European Space Agency
ETM+	Enhanced Thematic Mapper Plus
FPRZ	Frozen Percolation Radar Zone
GARS	German Antarctic Receiving Station at the Chilean Antarctic Station Bernardo O'Higgins
GCP	Ground Control Point
GIA	Geoscientific Information System Antarctica
GIS	Geographic Information System
GLIMS	Global Land Ice Measurements from Space
GTK	The GIMP Toolkit
GUI	Graphical User Interface
HDRF	Hemispherical-Directional Reflectance Factor
ID	Identifier
IPG	*Institut für Physische Geographie* of the *Universität Freiburg*
IPY	International Polar Year
IR	Infrared
ISO	International Organization for Standardization
ISODATA	Iterative Self-Organizing Data Analysis Technique
JPL	Jet Propulsion Laboratory
Landsat	Land Remote Sensing Satellite
MAPSAR	Multi-Application Purpose SAR
MIR	Middle-Infrared
MSS	Multi-Spectral Scanner
NASA	National Aeronautics and Space Administration
NCEP/NCAR	National Centers for Environmental Prediction/National Center for Atmospheric Research
NIR	Near-Infrared
NM	Normalised Mean
OGC	Open GIS Consortium
PAN	Panchromatic
PDD	Positive Degree-Day
PHP	recursive acronym for PHP: Hypertext preprocessor

Radar	Radio Detection And Ranging
Radarsat	Radar satellite
RAMP	Radarsat Antarctic Mapping Project
RBV	Return Beam Vidicon
RC	Regional Center
RMSE	Root Mean Square Error
SAR	Synthetic Aperture Radar
SCAR	Scientific Committee on Antarctic Research
SD	Standard Deviation
SML	Spatial Modeler Language
SSI	South Shetland Islands
SQL	Structured Query Language
SWIR	Short-Wave Infrared
TIR	Thermal Infrared
TM	Thematic Mapper
TPE	Trinity Peninsula
USGS	United States Geological Survey
UTM	Universal Transverse Mercator
VIS	Visible
VNIR	Visible and Near Infrared
WFS	Web Feature Service
WGS84	World Geodetic System 1984
WSRZ	Wet Snow Radar Zone
WSOZ	Wet Snow Optical Zone

Symbols

$1 - P$	Proportion of glaciers estimated to be misclassified
B	Offset value for each band
C	Factor for updating the gain due to the elevation antenna pattern
c	Confidence Level
D	c divided by Z
DN	Digital number
$DN_{i,j}$	Pixel intensity value at location (i,j)
d	Earth-Sun distance
E_0	Exoatmospheric solar spectral irradiance
G	Sensor gain
K	Absolute calibration constant for ERS-1/2 data
L_{max}	Maximum radiance detected at sensor
L_{min}	Minimum radiance detected at sensor
L_{sat}	Radiance at sensor
N	Population
N	Number of pixels within an area of interest
Ns_i	Number of glaciers in each stratum
n	Sub-sample size
ns_i	Number of sub-samples per stratum i
P	Proportion of glaciers estimated to be classified precisely
Z	Z value for the confidence level required
α	Average incidence angle within a distributed target
α_{ref}	Reference incidence angle (i.e., 23^o)
θ_z	Solar zenith angle
ρ_{sat}	Reflectance at sensor
σ^0	Backscattering coefficient (dB)
σ^0_{linear}	Backscattering coefficient (linear value)

1 Introduction

1.1 Motivation

Recent studies indicate a changing climate on the Antarctic Peninsula (AP) over the last several decades (King and Harangozo, 1998; Skvarca et al., 1998; Vaughan et al., 2003). For this region, climatic change has been documented through various observations and facts such as a significant warming trend (King, 1994; Stark, 1994; Marshall et al., 2002; Morris and Vaughan, 2003), changes in precipitation patterns (Turner et al., 1997), reduction of seasonal sea ice (Parkinson, 2002; Zwally et al., 2002a), disintegration of ice shelves (Doake and Vaughan, 1991; Rott et al., 1996; Skvarca et al., 1999a; Rack and Rott, 2004), retreat of glacier fronts (Simões et al., 1999; Braun and Gossmann, 2002; Rau et al., 2004; Cook et al., 2005), upward shift of the dry snow line (Rau, 2003), and increasing trend in duration of melting conditions (Fahnestock et al., 2002; Torinesi et al., 2003; Vaughan, 2006). Figure 1.1 summarises the main indicators of climate change and related phenomena observed on the AP.

The statistically significant warming trend on the AP was detected using different datasets. For instance, investigations of monthly mean surface air temperature from stations on the AP (Rothera and Faraday/Vernadsky) and South Shetland Islands (SSI) (Bellingshausen) identified positive trends from 0.038 to 0.067^{o}C year^{-1} over the period 1947-1990 (King, 1994). Moreover, radiosonde temperature observations complemented by NCEP/NCAR reanalysis data revealed a mean annual tropospheric (850-300 hPa) warming of 0.027 ± 0.022^{o}C year^{-1} above

Faraday/Vernadsky between 1956 and 1999 (Marshall et al., 2002). Finally, a database of more than 500 mean annual temperatures derived from measurements of snow temperature at around 10-m depth and air temperature measured at meteorological stations and automatic weather stations allowed Morris and Vaughan (2003) to estimate the trend in temperature for the whole AP in 3.8 ± 0.7°C over the last 100 years.

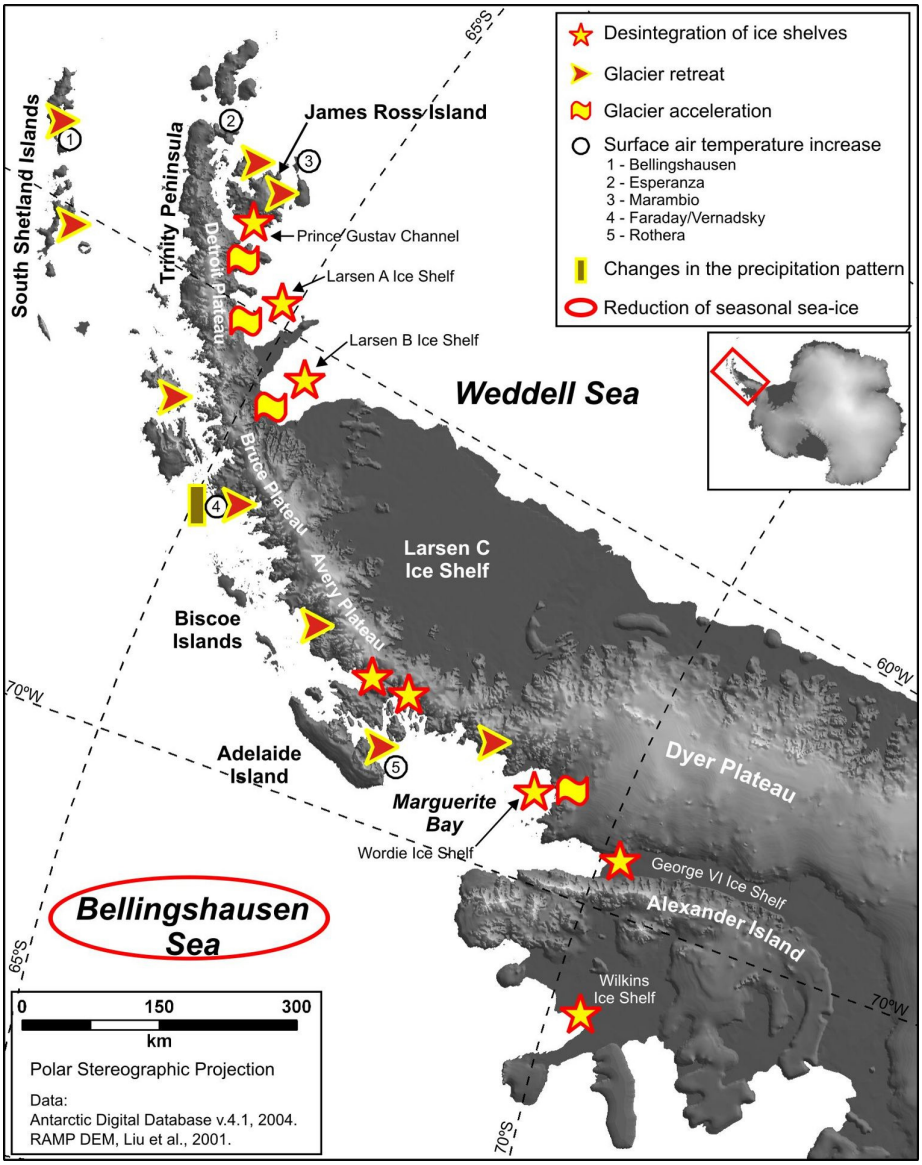

Figure 1.1: *Indicators of climate change on the Antarctic Peninsula. Modified after Braun and Rau (2001) and Rau (2003).*

In addition to atmospheric warming, a statistically significant rise in number of precipitation events (about 50%) during winter was reported from observations at Faraday/Vernadsky since 1956 (Turner et al., 1997). It appears to be related to the more frequent arrive of cyclones from Bellingshausen Sea (Turner et al., 1995), wherefrom this precipitation is originated (Turner et al., 1998). Furthermore, data from ice cores (Peel, 1992; Thompson et al., 1994; Raymond et al., 1996) indicated an increase in accumulation on the plateaus of the AP in the last decades.

Satellite passive-microwave data was used to map the length of the sea-ice season between 1979 and 1999 using algorithms and procedures developed by Gloersen et al. (1992) and Cavalieri et al. (1999). The results showed a shortening of the sea-ice season in almost the entire Bellingshausen Sea (Parkinson, 2002), but an increase in extension was observed for the Weddel Sea. These results agree with previous work from Stammerjohn and Smith (1997). Furthermore, considering the period from 1979 to 1998, Zwally et al. (2002a) estimated the trends in sea-ice extension as -9.7 ± 1.5% decade^{-1} for the entire sector of Bellingshausen-Amundsen Seas and 1.4 ± 0.9% decade^{-1} for the Weddel Sea.

Receiving extensive attention from the general public and media, successive disintegration and retreat of ice shelves has taken place on the AP over the last two decades. After the break-up of the Wordie Ice Shelf in the late 1980s (Doake and Vaughan, 1991; Vaughan and Doake, 1996), the marked retread of the northern margins of George VI and Wilkins ice shelves was detected (Lucchitta and Rosanova, 1998), followed by a rapid sequence of disintegration events on the eastern side of the peninsula: the Prince Gustav and Larsen A ice shelves disappeared in 1995 (Rott et al., 1996; Rott et al., 2002); and the Larsen B started calving in 1995 and collapsed completely in 2002 (Skvarca et al., 1999a; Rack and Rott, 2004). The progressive thinning (Shepherd et al., 2003; Skvarca et al., 2004), the formation of melt ponds (Scambos et al., 2000; Scambos et al., 2003), and extended melt seasons (Fahnestock et al., 2002; Van den Broeke, 2005) linked to break-up of ice shelves are strong evidences that these events occurred in response to climate warming. Furthermore, Morris and Vaughan (2003) indicated the -9^{o}C isotherm of mean annual temperature as the new limit of ice shelf distribution in 2002, updating the -5^{o}C limit previously proposed by Reynolds

(1981).

An overall trend of glacier front recession was detected on the AP (Rau et al., 2004; Cook et al., 2005), James Ross Island (Skvarca et al., 1995; Skvarca and De Angelis, 2003) and SSI (Park et al., 1998; Calvet et al., 1999; Simões et al., 1999; Braun and Gossmann, 2002). As suggested by Cook et al. (2005), floating glaciers may be reacting to the progressive atmospheric warming detected on the AP (Vaughan et al., 2003), like do the ice shelves (Morris and Vaughan, 2003; Scambos et al., 2003). However, as they are influenced by other external factors (e.g., oceanic temperature and circulation), it is difficult to distinguish a clear climate signal (Rau et al., 2004). Tidewater glaciers with their fully grounded marine termini are influenced by a complex set of forcings composed by atmospheric temperature, oceanographic parameters and subglacial topography (Van der Veen, 2002), and can not be used directly for understanding influence of short time climate change on ice masses (Pfeffer, 2003).

ERS-1/2 Synthetic Aperture Radar (SAR) data was used by Rau (2003) for investigating the dry snow line position on the AP between 65° and 68°S. This author detected an upward shift of the dry snow line on Avery Plateau and interpreted this as a direct response to the increasing number of high temperature events recorded at San Martin during the 1991-2000 decade.

A rising trend in duration of melt periods on the AP was detected by using two different methods. Fahnestock et al. (2002) and Torinesi et al. (2003) examined the duration of melt seasons over 22 and 20 year periods respectively, using satellite-based passive microwave data processed with the melt-detection algorithm proposed by Abdalati and Steffen (1997). Both studies found a high variability in duration of the melt season, but also a slightly positive trend in melt-season length. Vaughan (2006) used an approach based on positive degree-days (PDDs) as predictor of ablation conditions. By using temperature trends from Morris and Vaughan (2003), annual PDDs were calculated for the whole AP over the period 1950-2050. Results indicated a strong positive trend in annual PDDs, mainly concentrated on the northeastern sector of the AP.

The dependence of cryospheric changes on variations in climate parameters seems to be evident (Vaughan and Doake, 1996; Rott et al., 1998; Skvarca et al.,

1999b; Scambos et al., 2000; Rott et al., 2002; Scambos et al., 2003; Shepherd et al., 2003; Skvarca and De Angelis, 2003). In addition, some glacial processes are further influenced by such detected changes. For instance, glacier tributaries from Larsen Ice Shelf A and B, accelerated and thinned after the ice shelves' disintegration (De Angelis and Skvarca, 2003; Rignot et al., 2004; Scambos et al., 2004). Moreover, Rignot et al. (2005) showed that similar phenomenon also occurred subsequent to the disintegration of the Wordie Ice Shelf on the other side of the AP. Earlier assessments (Drewry and Morris, 1992; Vaughan, 1992) on the contribution of the AP ice masses to sea level rise have been re-evaluated (Rignot et al., 2005), and the lather authors concluded that the mass loss is not negligible at the present. Indeed, the potential ice loss estimated for this region for the period after the break-up of the Larsen B in 2002 is sufficient to raise the sea level by 0.1 mm $year^{-1}$ (Rignot et al., 2005).

Although the exact time response of the above described glaciological processes to climate change remains uncertain, it is becoming increasingly apparent that variations on relatively short time scale are usual (Rignot and Thomas, 2002). However, the lack of consistent systematic observations (e.g., multi-year observations covering a statistically representative set of glaciers on the AP) generate extensive data gaps (Turner et al., 2002; Alley et al., 2005), which make difficult the modelling of further glacial responses to climate change. It is still more complicated for the high parts of the glacial systems, where only sporadic measurements are made.

The development of glacier facies (Williams et al., 1991; Ramage and Isacks, 1998) and fluctuations of ice fronts (Rau et al., 2004; Cook et al., 2005) are also affected by local and regional climatic and meteorological settings. Thus, their time-dependent variations are considered as particularly sensitive indicators of climatic changes (Rau et al., 2001). In addition, several authors demonstrated that these parameters can be monitored by using remote sensing data from radar (Forster et al., 1996; Partington, 1998; Ramage and Isacks, 1998; Rau and Saurer, 1998; Braun et al., 2000; Ramage et al., 2000; Rau et al., 2001; König et al., 2001) and optical sensors (Williams et al., 1991; Boresjö-Bronge and Bronge, 1999; Sidjak and Wheate, 1999; König et al., 2001; Heiskanen et al., 2003). The large number of Earth observation programs carried out in the last two decades

generated plenty of satellite datasets for the AP. In this context, a major challenge is the development of semi-automatic methods for analysing the existing and future data.

1.2 Study purpose

The just above mentioned demand for an automatisation of data processing is the starting point for this study. Consequently, its main objective is:

- the development of methods for semi-automatic extraction of glacier parameters (i.e., boundaries between glacier zones and glacier frontal position) on the Antarctic Peninsula using multi-temporal and multi-sensor remote sensing datasets.

Based on that, the focus of the work is on:

- the development of a new methodological approach for analysis of glacier parameters using satellite sensor data;
- the development of algorithms for classifying radar and optical imagery;
- the implementation of a semi-automatic workflow for processing of multi-sensor datasets and evaluation of its use in a productive environment;
- the application of developed methods for analysing a multi-temporal dataset available at the IPG; and
- a preliminary analysis of spatial and temporal variations on glaciers parameters of the AP.

1.3 Outline of the thesis

This thesis is divided in three main parts:

(1) the **conceptual framework** consists of chapters 2 and 3. Chapter 2 gives background on development of different facies or zones on glaciers. Furthermore, this chapter describes the remote sensing and GIS datasets

used for developing image analysis methods discussed in further chapters. In chapter 3 a new method, the so-called *centerline approach*, for monitoring spatial and temporal changes in the extent of glacier facies and in glacier frontal position using satellite imagery is described;

(2) the **development of methods** is explained in chapters 4, 5 and 6. Chapter 4 describes the semi-automatic processing chain developed to extract glacier parameters from satellite imagery using the centerline approach, whereas details about specific processes used for analyses of SAR and optical data are given in chapters 5 and 6 respectively; and

(3) the **potential and applications** of the centreline approach are described in chapters 7, 8, and 9. In chapter 7 the potential of the developed centerline approach and its computational implementation (i.e., IceTools) is discussed. Furthermore, there is explained how the processing workflow is prepared for additional datasets. Chapter 8 presents a multi-temporal analysis carried out using methods developed in this work. The work concludes with the perspectives for future work (chapter 9).

2 Theory and data

As mentioned above (chapter 1.2), the present study aims to develop semi-automatic methods for monitoring spatial and temporal patterns of glacier changes on the Antarctic Peninsula (AP) by means of remote sensing techniques. This chapter presents the glacier parameters to be monitored and their main characteristics. Furthermore, it describes the remote sensing and GIS datasets used for developing the methods of data analysis explained in chapters 4, 5, and 6.

2.1 Time dependent glacier parameters

The concept of superficial facies or zones on glaciers was first presented by Benson (1996) and Müller (1962), and reviewed by Paterson (1994). In this work, we use the reviewed concept from Paterson (1994) illustrated by figure 2.1. This author described the occurrence of five distinct zones on glaciers:

(1) dry snow zone;

(2) percolation zone;

(3) wet snow zone;

(4) superimposed ice zone; and

(5) ablation area.

As outlined in chapter 1.2, methods are developed in this study for analysing

spatial and temporal patterns of glacier changes on the AP by monitoring the **boundaries between glacier facies or zones** (i.e., **snow line, transient wet snow line, and dry snow line**) and their altitudinal changes, as well as variations of **glacier frontal positions**. Because local and regional climatic and meteorological settings affect the development of zones on glaciers (Williams et al., 1991; Ramage and Isacks, 1998) and fluctuations of their ice fronts (Rau et al., 2004; Cook et al., 2005), the time-dependent variation of these parameters are considered as good indicators of climatic changes (Rau et al., 2001).

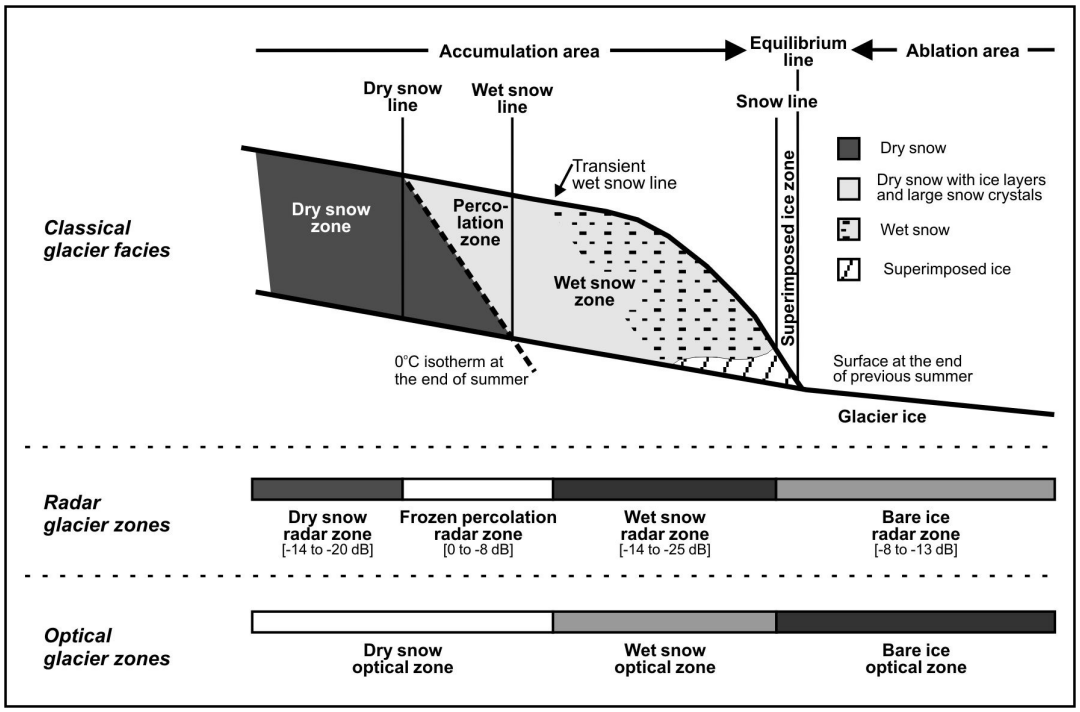

Figure 2.1: *Classical glacier facies as described by Paterson (1994) and corresponding glacier zones as detected by SAR and optical sensors. Modified after Rau et al. (2001).*

2.1.1 Dry snow zone

In the dry snow zone of a glacier, melting is even in summer not present (Paterson, 1994). This zone is restricted to areas in the interior of Antarctica and Greenland, where the surface air temperature never rises above the melting point. As a result, morphological changes in snow structure are dominated by processes

of dry snow metamorphism (Colbeck, 1983; Singh and Singh, 2001). Starting during the snowfall, snow is compacted under its own weight and further metamorphosed under the effect of wind (equitemperature or destructive metamorphism; Singh and Singh, 2001). When a temperature gradient exists in the snow cover, it is accompanied by a vapour pressure gradient which causes mass transport and recrystallization (temperature gradient of constructive metamorphism; Singh and Singh, 2001). Small grain sizes are characteristic here, excepting when the formation of depth hoar crystals occurs (Partington, 1998). The boundary between this zone and the percolation zone is called the dry snow line.

2.1.2 Percolation zone

The percolation zone is characterised by some surface melting (Partington, 1998). In events of high energy input, the meltwater in this zone can percolate down through the snow before it refreezes. If it occurs in vertical structures like canals, ice glands are formed. But when the water reaches an impermeable layer, it flows laterally and forms ice layers or lenses when refreezes. Besides this kind of structures, the snowpack in this zone is characterized by large grain sizes resulting from melt-freeze metamorphism (Colbeck, 1982). The wet snow line separates the percolation zone from the wet snow zone.

2.1.3 Wet snow zone

In this zone, all snow deposited during the previous accumulation season has been raised to 0^{o} C by the end of the summer (Paterson, 1994). In addition, some meltwater percolates into deeper layers which were deposited in previous years. The lower parts of the wet snow zone are separated from the superimposed ice zone by the snow line, also called firn line or annual snow line.

2.1.4 Superimposed ice zone

When the refrozen meltwater is so abundant at lower elevations, it can merge ice structures like ice layers, lenses and glands, forming a continuous mass of superimposed ice zone. This term is restricted to areas where there is an annual increment of superimposed ice at the surface. The limit between the superimposed ice zone and the ablation area is the equilibrium line.

2.1.5 Ablation area

This is the area below the equilibrium line (Paterson, 1994). Here, all snow deposited during the previous winter has melted by the end of the ablation season (Partington, 1998), resulting in an irregular surface of exposed glacier ice. However, the presence of some remaining snow and/or firn patches is common in this zone.

2.1.6 Boundaries between glacier facies

Spatial and temporal measurements of glacier mass balance and derivation of actual and recent meteorological parameters are of special interest for glaciological and climatological research (Rau et al., 2001). As the position of the boundaries between glacier facies are variable in time (Paterson, 1994), responding to changes in energy and mass balance, they provide information on both parameters stated above (Forster et al., 1996):

(1) changes in the **dry snow line** altitude indicate singular extreme melt events impacting high altitude areas (Rau et al., 2000), when it moves upwards. In addition, backscatter modelling (Rau and Braun, 2002) shows that a progression downwards would indicate increased accumulation rates;

(2) the **transient wet snow line** is often regarded as coinciding with the position of the actual 0°C isotherm (Williams et al., 1991; Partington, 1998). Furthermore, Vaughan (2006) showed the importance of the surface melting on the AP for runoff modelling. Thus, by monitoring the duration of surface

melting it is possible to estimate changes in runoff; and

(3) the position of the **snow line** documents the current extension of the ablation area, which depends on energy available for melting. Moreover, the snow line altitude at the end of the ablation season is considered a proxy to the equilibrium line altitude (ELA) (Williams et al., 1991; Engeset and Weydahl, 1998; Rau et al., 2001; Bardel et al., 2002). Its variations upwards or downwards indicate negative or positive mass balance respectively.

Consequently, the monitoring of borders between glacier facies is of special value for the AP, where glacier mass balance measurements are carried out only for a few glaciers unevenly distributed along this region, and logistical requirements limit the implementation of a dense network of meteorological stations.

Several authors demonstrate the potential of remote sensing data from radar (Jezek et al., 1994; Forster et al., 1996; Albright et al., 1998; Partington, 1998; Ramage and Isacks, 1998; Rau and Saurer, 1998; Braun et al., 2000; Ramage et al., 2000; Rau et al., 2001; König et al., 2001) and optical sensors (Hall et al., 1987; Hall et al., 1988; Williams et al., 1991; Bronge and Bronge, 1999; Sidjak and Wheate, 1999; König et al., 2001; Heiskanen et al., 2003) to identify distinct zonal boundaries within glaciers. The analogous radar glacier zones in figure 2.1 correspond to the classification scheme proposed by Rau et al. (2001), and the optical glacier zones (Figure 2.1) are based on Hall et al. (1988), Williams et al. (1991), Sidjak and Wheate (1999), and Heiskanen et al. (2003). Chapters 5.2 and 6.2 describe the glacier zones as detected by radar and optical sensors respectively.

2.1.7 Glacier frontal position

Spectacular events of disintegration of ice shelves (Vaughan and Doake, 1996; Skvarca et al., 1999a; Rott et al., 2002; Rack and Rott, 2004) and a general trend of recession from glacier fronts (Rau et al., 2004; Cook et al., 2005) have occurred on the AP in the last five decades. Events of ice shelf break-up are directly linked to the rising air temperatures (Morris and Vaughan, 2003) and extended melt seasons (Scambos et al., 2000). Although variations of glacier frontal positions are

also interpreted as responses to the rapid changing climate in the region (Rau et al., 2004), the detected glacier retreat do not show simple correlation with environmental parameters (e.g., air temperature, sea-ice concentration) recorded on this area (Cook et al., 2005).

Recent studies have shown that the loss of ice shelves at the AP has caused acceleration of their tributary glaciers (De Angelis and Skvarca, 2003; Rignot et al., 2004; Scambos et al., 2004; Rignot et al., 2005), creating locally a high negative balance. The removal of floating ice in other areas could increase the imbalance and therefore intensify the contribution to sea level rise (Cook et al., 2005). Thus, variations of glacier frontal positions on the AP indicate not only areas which are responding to climatic changes and consequent effects on accumulation and ablation patterns (Rau et al., 2004), but it also shows glaciers which by cumulative loss of ice at the fronts can be contributing to an increased drainage of the AP (Cook et al., 2005).

Summary 2.1:

The development of zones on glaciers and the variations of glacier frontal positions are greatly influenced by local and regional climatic and meteorological settings. Their variations as response to changes in energy or mass balance are considered as good indicators of climatic changes. In this investigation, glacier changes are analysed by monitoring: (1) altitudinal variations in the limits between glacier facies (i.e., snow line, transient wet snow line, and dry snow line); and (2) changes in glacier frontal positions.

2.2 Remote sensing data and sensors platforms

The large number of Earth observation programs carried out in the last two decades generated plenty of satellite datasets for the AP. It was particularly supported by special missions (e.g., the Radarsat Antarctic Mapping Project) or dedicated ground receiving stations (e.g., the German Antarctic Receiving Station (GARS) at the Chilean Antarctic Station Bernardo O'Higgins, AP). Furthermore, additional satellite missions are planned within the next two or three years (e.g., ALOS, CBERS-2b and 3, Radarsat-2, Cryosat, MAPSAR), and will increase not

only the amount of existing data, but also the rate of data acquisition. Due to its comprehensive coverage in space and time, the available datasets constitute an unique tool for climate research. However, the systematic investigation of existing and future data is not feasible if only analyst-based analyses are considered. In this context, **a major challenge** is

> *the development of (semi-)automatic methods for analysing the existing and future datasets*.

In this work, a subset of data archived at the IPG is used for the development of semi-automatic methods for classification of glacier parameters, and a preliminary analysis. Almost all scenes from the IPG archive were acquired for north of 70º S. Radar data consist of around 68 images acquired from 1991 to 2005 by the sensors ERS-1/2 SAR and Envisat ASAR. Optical data consist of about 59 scenes from the sensors Landsat 4/5 TM, Landsat 7 ETM+ and Terra ASTER, acquired in the time period 1986 to 2003.

2.2.1 SAR systems – platforms and specifications

The launch of the **first European Remote Sensing** satellite (ERS-1) in July 1991, followed by the similar ERS-2 and the improved Envisat, **started the longest record of active microwave data ever acquired**. Among a comprehensive set of instruments for Earth observation, the ERS-1 carried an Active Microwave Instrument (AMI) consisting of a Synthetic Aperture Radar (SAR) sensor and a Wind Scatterometer (both in the C-band). The ERS-1 SAR was the first satellite sensor to produce high resolution imagery of the Earth's surface day and night and in all weather conditions. A second satellite (**ERS-2**) was launched in April 1995. ERS-2 carries a SAR system similar to the ERS-1 AMI SAR (see table 2.1). Both spacecrafts were placed in sun-synchronous polar orbit, enabling the acquisition of data on high latitudes. Due to the small storage capacity on board the ERS-1/2, SAR data from instruments on board these platforms is only acquired within the reception zone of an equipped ground receiving station. The highly dynamic climatic and glaciological processes occurring on the AP, and the suitability of SAR data for polar studies, generated the need for a receiving station in this area.

So, the GARS was installed in the Chilean station O'Higgins at the northern tip of the AP (Reiniger and Zimmer, 2000).

Table 2.1: *Main characteristics of the SAR systems on board the platforms ERS-1, ERS-2, and Envisat.*

Platform	ERS-1	ERS-2	Envisat
Sensor	AMI SAR	AMI SAR	ASAR
Launch date	Jul. 1991	Apr. 1995	Mar. 2002
Operation end	Mar. 2000	still operating	still operating
Bands (wave length)	C (5.6 cm)	C (5.6 cm)	C (5.6 cm)
Polarisation	VV	VV	VV or HH (Image Mode); HH/VV, HH/HV or VV/VH (Alternating Polarisation Mode)
Range resolution (m)	26	26	30 (Image Mode); 150 (Wide Swath Mode)
Azimuth resolution (m)	28	28	30 (Image Mode); 150 (Wide Swath Mode)
Number of looks	6	6	4
Incident angle (°)	23	23	20-50
Nominal altitude (km)	785	785	800
Inclination (°)	98.5	98.5	98.5
Repeat cycle (days)	3, 35, 176	35	35
Swath width (km)	100	100	100 (Image Mode); 405 (Wide Swath Mode)

In order **to extend the mission** of the ERS-1/2 SAR, the Advanced Synthetic Aperture Radar (**ASAR**) sensor was launched in March 2002 on board the **Envisat** satellite. The Envisat is a multi-instruments platform, flying in a sun-synchronous polar orbit of 800 km altitude. In addition to ERS-1/2 SAR imaging capabilities, ASAR was enhanced in terms of polarisation, range of incidence angles, coverage, and modes of operation (Table 2.1). However, ASAR Alternating Polarisation products acquired on the AP consist of only 12 images at all, obtained with the configuration HH/VV (i.e., two co-registered images: a HH-polarised image, and a VV-polarised image). At C-band, backscatter signatures of glacier zones from HH-polarised data are similar to those from data acquired with VV polarisation (Rau and Saurer, 1998; Ramage et al., 2000). So, the Alternating Polarisation data available for the AP is not appropriated to be used as a new dataset for developing and testing automatic methods for glacier monitoring.

Because of SAR Image Mode data is available for the AP since 1991, this kind of data is used in this work. It enables a 15-years record of changes in position of boundaries between glacier facies. Nevertheless, the modular structure of the developed classification algorithm (see chapter 4) easily enables to adapt the processing chain for other acquisition modes (e.g., Wide Swath Mode, Alternating Polarisation Mode). In the Image Mode, SAR sensors provide two-dimensional images with a spatial resolution of 26 m in range (across track) and between 6 and 30 m in azimuth (along track), covering a strip of about 100 km in width (Figure 2.2). Pulses of electromagnetic radiation are transmitted and received by the antenna of the SAR, which is aligned along the satellite's orbit path to direct a narrow beam to the right, downwards on the Earth's surface. Imagery is built up from the time delay and strength of the return signals, which depend primarily on the roughness and dielectric properties of the surface and its range from the satellite. More information on SAR imaging, processing and applications can be found in Ulaby et al. (1986) and Henderson and Lewis (1998).

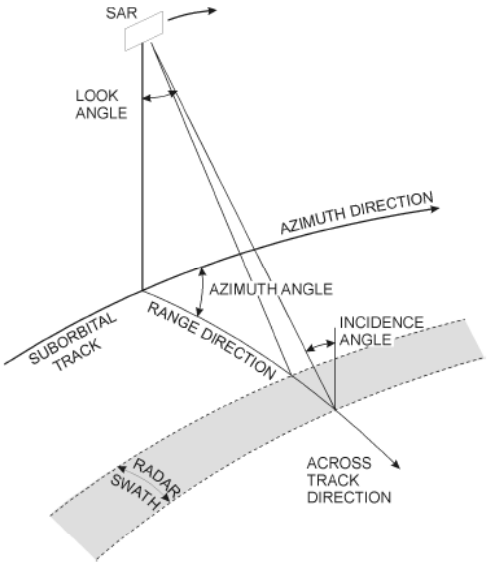

Figure 2.2: *Acquisition geometry of SAR data (modified after Henderson and Lewis, 1998).*

2.2.2 Optical scanners – platforms and specifications

Datasets from imaging sensors in the optical range of the electromagnetic spectrum with high-resolution and multispectral capabilities (e.g., Landsat MSS, TM, and ETM+; SPOT; Terra ASTER) are available since the launch of the first satellite of the **Landsat** series in 1972. Since then, the Landsat missions form **the longest-running program** for acquisition of imagery of the Earth from space. During the last 34 years the sensors were improved but they were kept compatible too. Landsat 1-3 (originally called Earth Resources Technology Satellite – ERTS)

carried two sensor systems: the Return Beam Vidicon (RBV) and the Multi-Spectral Scanner (MSS). However, the RBV failed early on the Landsat 1 and never came into routine use. The MSS sensor was able to acquire four bands of imagery, two in the visible spectrum and two in the near-infrared spectrum, with 80 m spatial resolution. The Landsat 4 was launched in 1984 carrying besides the old MSS, a new instrument called Thematic Mapper (**TM**). Instrument upgrades included improved ground resolution (30 meters) and 3 new bands. With the same configuration as Landsat 4, Landsat 5 was launched in 1984 and is still acquiring data. In 1993, the Landsat 6 failed to achieve orbit during launch. The last satellite of the Landsat series (Landsat 7), was launched in April 1999, carrying an Enhanced Thematic Mapper Plus (**ETM+**) sensor (see table 2.2 and figure 2.3). Initially, the Landsat program was developed and maintained by the National Aeronautics and Space Administration (NASA). Nowadays, it is supported and coordinated by the United States Geological Survey (USGS) in cooperation with the NASA.

The TM and ETM+ sensors are multi-spectral, nadir-viewing sensors, scanning the Earth's surface by oscillating a mirror perpendicularly to the flight direction (across track) (Figure 2.4). The incoming reflected or emitted radiation passes through a telescope and hits the focal planes holding detectors, which sense the intensity of the radiation received by the sensor and convert into 256 discrete levels (digital numbers).

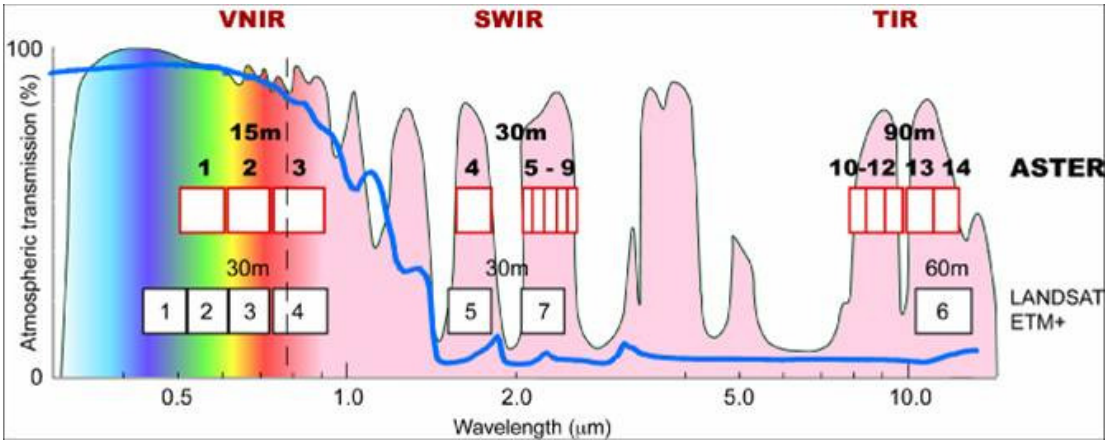

Figure 2.3: *Spectral bands of the sensors Landsat ETM+ and ASTER along the electromagnetic spectrum (JPL, 2006). The rectangular boxes indicate the sensor channels (black: Landsat ETM+, red: ASTER).*

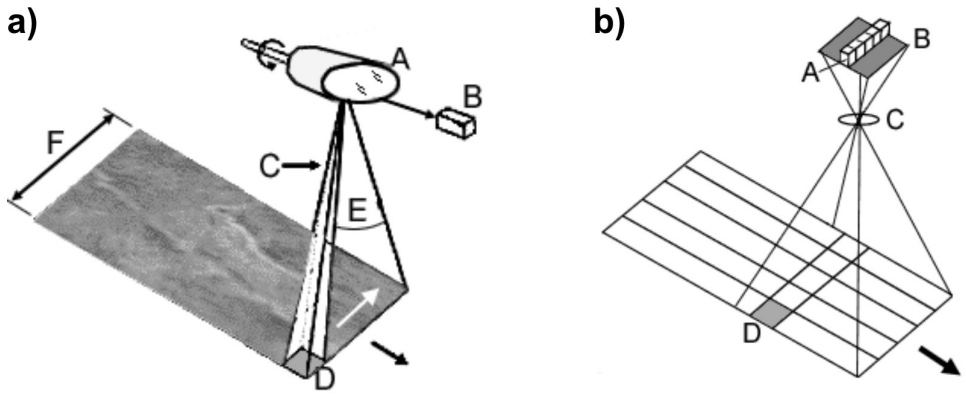

Figure 2.4: *a) Imaging principles of across-track (Landsat TM and ETM+) and b) along-track scanners (Terra ASTER) (CCRS, 2006).*

Complementing the Landsat program, the Advanced Spaceborn Thermal Emission and Reflection Radiometer (**ASTER**) is a multi-spectral sensor **on board** the satellite **Terra**, launched in December 1999. This spacecraft is part of a series of multi-instruments satellites forming NASA's Earth Observation System (EOS). The sensor ASTER was developed in a cooperation of Japan's Ministry of Economy Trade and Industry and NASA. It consists of three subsystems (the visible and near infrared - **VNIR**; the short-wave infrared - **SWIR**; and the thermal infrared - TIR), scanning the Earth's surface during the satellite motion (along track) (Figure 2.4). ASTER products result in 60 x 60 km images, with spatial resolution between 15 and 60 m (see table 2.2 and figure 2.3). Contrasting with the sensors on board the Landsat satellites which acquire data during all the time, the ASTER sensor works only upon user request.

Optical data used in this study consist of systematically corrected imagery (i.e., Landsat TM/ETM+ level 1G and Terra ASTER level 1B). It includes both radiometric and geometric correction. Image data is provided in rescaled digital number (DN) values; noise, interference, banding, artefacts, and other spectral anomalies are corrected. Furthermore, the scene is rotated, aligned, and projected to Universal Transverse Mercator (UTM). Geometric accuracy of systematically corrected product is within 250 or 150 m in case of TM/ETM+ or ASTER data respectively (JPL, 2001; NASA, 2006). The sun-synchronous orbits of the Landsat and Terra platforms ensure that the satellite always passes over a point at the same local time, minimizing the variations in solar illumination. More information on Terra and Landsat programs can be found in JPL (2001), Abrams et al. (2002), and NASA (2006).

Table 2.2: *Main characteristics of the Landsat 4 and 5 TM, 7 ETM+, and Terra ASTER sensors.*

Platform	Landsat 4	Landsat 5	Landsat 7	Terra
Sensor	TM	TM	ETM+	ASTER
Launch date	Jul. 1982	Mar. 1984	Apr. 1999	Dec. 1999
Operation end	Aug. 1993[1]	still operating	still operating	still operating
Bands (wave length in µm)	1 (0.45-0.52) ***2 (0.52-0.60)*** ***3 (0.63-0.69)*** ***4 (0.76-0.90)*** ***5 (1.55-1.75)*** 6 (10.4-12.5) 7 (2.08-2.35)	1 (0.45-0.52) ***2 (0.52-0.60)*** ***3 (0.63-0.69)*** ***4 (0.76-0.90)*** ***5 (1.55-1.75)*** 6 (10.4-12.5) 7 (2.08-2.35)	1 (0.45-0.52) ***2 (0.53-0.61)*** ***3 (0.63-0.69)*** ***4 (0.78-0.90)*** ***5 (1.55-1.75)*** 6 (10.4-12.5) 7 (2.09-2.35) 8 (0.52-0.90)	***1 (0.52-0.60)*** ***2 (0.63-0.69)*** ***3 (0.76-0.86)*** ***4 (1.60-1.70)*** 5 (2.145-2.185) 6 (2.185-2.225) 7 (2.235-2.285) 8 (2.295-2.365) 9 (2.260-2.430) 10 (8.125-8.475) 11 (8.475-8.825) 12 (8.925-9.275) 13 (10.25-10.95) 14 (10.95-11.65)
Ground resolution (m)	VIR 30 TIR 120	VIR 30 TIR 120	PAN 15 VIR 30 TIR 60	VNIR 15 SWIR 30 TIR 90
Dynamic range (bits)	8	8	8	VNIR 8 SWIR 8 TIR 12
Repeat cycle (days)	16	16	16	16
Altitude (km)	705	705	705	705
Swath width (km)	185	185	185	60
Cross track Pointing (degrees)	0	0	0	VNIR ± 24 SWIR ± 8.55 TIR ± 8.55

[1] *TM data transmission failed.*

Summary 2.2:

Resulting from several Earth observation programs carried out in the last two decades, a huge amount of data is available for the Antarctic Peninsula. Furthermore, additional satellite missions are scheduled to be operational within the next two or three years, and will increase not only the amount of existing data, but also the rate of data acquisition. Due to its comprehensive coverage in space and time, the available datasets constitute an unique tool for climate research. However, the systematic investigation of existing and future data is not feasible if only analyst-based analyses are considered. In this context, a major challenge is the development of automatic methods for analysing the existing and future datasets.

2.3 Value added remote sensing data

2.3.1 Geospatial reference data

To provide a common spatial reference for both SAR and optical datasets, and to ensure the compatibility of the resulting analyses data with the international project Global Land Ice Measurements from Space (GLIMS, http://www.glims.org) (see chapter 2.3.3), the UTM-projected version of the Landsat TM mosaic from the Geoscientific Information System Antarctica (GIA; Bennat et al., 1998) was chosen. The mosaic of the AP comprises more than 40 Landsat TM scenes acquired in the period 1986 to 1990. The **GIA Landsat TM mosaic** (Figure 2.5) has a spatial resolution of 30 m, with a given high spatial accuracy (standard deviation of ± 75 m in northing and easting).

In the processing chain of the GLIMS Regional Center (RC) *Antarctic Peninsula*, satellite imagery is projected to UTM, datum World Geodetic System 84 (WGS84). So, they generated a common geospatial reference by rigorously re-projecting the original files of the GIA Landsat TM mosaic from the original projection (Lambert Conformal Conic) to UTM (WGS84 datum). In order to standardise the pre-processing steps used in this work with the activities of the GLIMS RC *Antarctic Peninsula*, images used as input for image classification (chapters 5 and 6) are co-registered to the UTM-projected GIA Landsat mosaic. Furthermore, it enables the

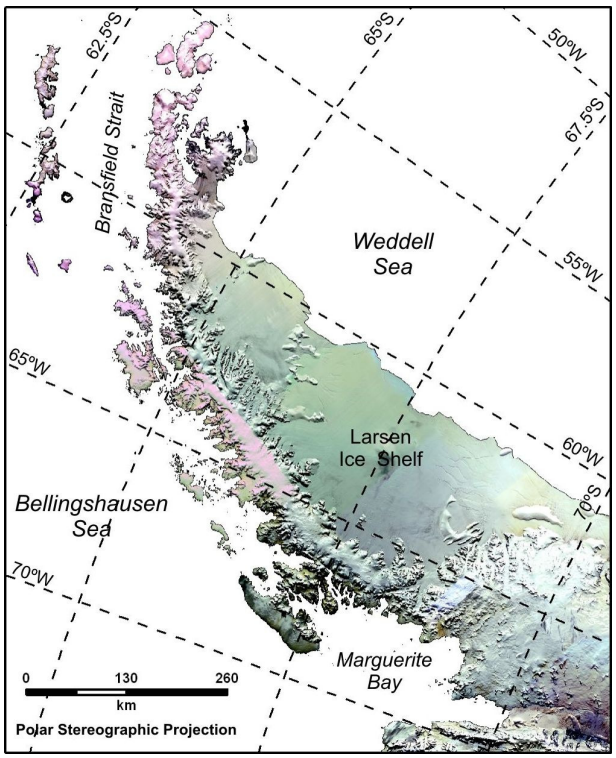

Figure 2.5: *Landsat TM mosaic of the Geoscientific Information System Antarctica (Bennat et al., 1998). It comprises more than 40 Landsat TM scenes acquired in the period 1986 to 1990, and is used as spatial reference for several international projects.*

compatibility with the SCAR Antarctic Digital Database (ADD, http://www.add.scar.org/) and the 'Coastal-Change and Glaciological Maps of the Antarctic Peninsula' which are actually in preparation by the USGS and British Antarctic Survey (BAS) (USGS Fact Sheet FS-017-02; http://pubs.usgs.gov/fs/fs17-02/).

2.3.2 Topographic data

Digital elevation data was used from the Radarsat Antarctic Mapping Project (RAMP) Digital Elevation Model (DEM) version 2 (Liu et al., 2001). The **RAMP DEM** was created from various datasets with the objective of orthorectifying Radarsat images used in RAMP (Liu et al., 1999; Liu et al., 2001). At the AP, data from the Antarctic Digital Database (ADD) and ERS altimetry were used on land and ice shelves respectively. It resulted in a product with a spatial resolution of 200 m (Figure 2.6), having a root mean square error (RMSE) of ± 1 pixel (200 m) of positional accuracy and 100-130 m of vertical accuracy on rough terrain and 2 m on ice shelves (Liu et al., 1999).

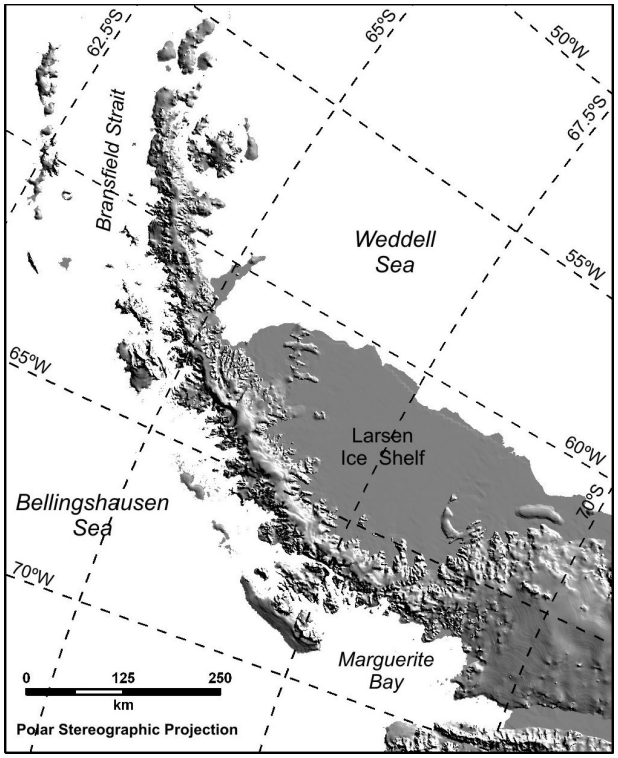

Figure 2.6: *Shaded relief image of the RAMP DEM for the Antarctic Peninsula north of 70° S. This DEM was generated from various datasets with the objective of orthorectifying Radarsat images used in RAMP.*

Furthermore, DEM with better spatial resolution (15 m), as well as positional (15 m) and vertical accuracies (60 m RMSE on rough terrain and 15 m on smooth terrain) can be generated from Terra ASTER scenes (Kääb et al., 2003). However, the incomplete coverage of cloud-free scenes on the AP (R. Jaña, personal

communication, 2006) is the major restriction to the use of ASTER DEMs as standard digital elevation reference for this study.

In order to standardise the pre-processing of satellite images in this work with the activities of the GLIMS RC *Antarctic Peninsula*, the RAMP DEM was re-projected from the original Polar Stereographic projection to UTM (WGS84). For that, the original pixel size was resampled to 100 m by using bilinear interpolation.

2.3.3 Glacier data

Within the project **Global Land Ice Measurements from Space** (GLIMS), a global set of glaciological data is collected and available for further investigations. GLIMS objective is to monitor glaciers on the Earth using primarily satellite data. For the AP, the Regional Centre (RC) located at the IPG supplies data on 950 glaciers. It forms the **Antarctic Peninsula glacier inventory**. Each glacier is represented in the geospatial format as a point feature (with known X and Y coordinates) related to attributes holding glacier static information (e.g., glacier name; identifier code) and parameters used to characterise the morphological shape of glaciers (Table 2.3). Rau et al. (2005) describe the glacier parameters used in the GLIMS RC *Antarctic Peninsula*. The GLIMS based morphological classification was done using satellite imagery, ground truth data, and expertise from several research groups working under the coordination of the RC *Antarctic Peninsula*.

The glacier data used in this work consists of a subset (560) of glaciers selected from the AP glacier inventory for the area north of 70º S. The selection of a subset of glaciers was required because almost all scenes from the IPG satellite data archive were acquired for north of 70º S. However, soon as the satellite data archived in international data centres becomes available, the developed methods can be easily expanded for remaining glaciers.

Table 2.3: *Parameters used by the GLIMS project to characterise the morphological shape of glaciers (Rau et al., 2005).*

GLIMS code	Primary classification	Form	Frontal characteristic	Longitudinal profile	Major source of nourishment	Activity of tongue	Moraine code 1	Moraine code 2	Debris coverage of tongue
0	Uncertain or miscellaneous	Uncertain or miscellaneous	Normal or miscellaneous	Uncertain or miscellaneous	Unknown	Uncertain	No moraines	No moraines	Uncertain
1	Continental ice sheet	Compound basins	Piedmont	Even, regular	Snow / Drift snow	Marked retreat	Terminal moraines	Terminal moraines	Debris free
2	Ice - field	Compound basin	Expanded	Hanging	Avalanche	Slight retreat	Lateral and/or medial moraine	Lateral and/or medial moraine	Partly debris covered
3	Ice cap	Simple basin	Lobed	Cascading	Superimposed ice	Stationary	Push moraine	Push moraine	Mostly debris covered
4	Outlet glacier	Cirque	Calving	Ice-fall		Slight advance	Combination of 1 and 2	Combination of 1 and 2	Completely debris covered
5	Valley glacier	Niche	Coalescing, non contributing	Interrupted		Marked advance	Combination of 1 and 3	Combination of 1 and 3	
6	Mountain Glacier	Crater				Possible surge	Combination of 2 and 3	Combination of 2 and 3	
7	Glacieret and snowfield	Ice apron				Known surge	Combination of 1, 2 and 3	Combination of 1, 2 and 3	
8	Ice shelf	Group				Oscillating	Debris, uncertain if morainic	Debris, uncertain if morainic	
9	Rock glacier	Remnant					Moraines, type uncertain or not listed	Moraines, type uncertain or not listed	
10	Ice stream		Calving & Piedmont						
11			Calving & Expanded						
12			Calving & Lobed						
13			Ice shelf nourishing						
14			Floating						
15			Terrestrial calving						
16			Terrestrial calving						

2.3.4 The Antarctic Peninsula glacier database

To record and manage results from satellite image analyses and to administer metadata describing such analyses, a relational glacier database was implemented. The relational database design (Figure 2.7) is compatible with the GLIMS data transfer standards (Raup and Khalsa, 2003) and was developed using free and open source software (i.e., the relational database system PostgreSQL installed with the geospatial extension PostGIS). The semantics (e.g., data type, geospatial data model) are compliant with the GLIMS data dictionary and the SCAR Feature Catalogue. It enables full compatibility with the GLIMS central database and the emerging Antarctic Spatial Data Infrastructure (AntSDI).

Furthermore, the relational structure of the database facilitates the record of additional cryospheric data resulting from further projects. For example, data from the Antarctic Peninsula glacier inventory described in chapter 2.3.3 was incorporated to the Antarctic Peninsula glacier database (AntPenDB), facilitating the data management at the GLIMS RC *Antarctic Peninsula*. Currently, the AntPenDB is composed of 11 tables:

- the table **glacier_static** holds time-independent glacier information, like glacier name, parent ice mass, the GLIMS glacier identifier (ID) and the local glacier ID as attributed for each glacier and used to relate glaciers to complementary data (e.g., glacier centerlines, input data for image classification) or data derived from analyses. Spatial features of type point represent the geographic location of the glaciers;
- the data recorded in the table **analysis** describe the processing applied to images in order to derive glacier dynamic parameters for the GLIMS project or the type of analysis used to extract the limits between glacier zones (this work). Furthermore, it relates results of analyses to the corresponding analysed images;
- the **ancillary** table stores metadata about supporting information used for analysis (e.g., scientific papers, additional raster datasets, meteorological data, ground truth data);
- the **glacier_dynamic** contains time-dependent glacier information resulting from GLIMS analyses. It consists of morphological information (see table 2.3; Rau et al., 2005) and measured attributes of glaciers, including its outline, speed, etc., which can be represented as polygons, lines or points;
- **images** holds general metadata of the analysed imagery. Image footprints are stored as polygons;
- the **cenline** stores glacier centerlines (vector lines) as digitised for each glacier studied in this work. The glacier centerlines are analyst-interpreted lines that approximately follows the main flow line of glaciers and constitute a key parameter for the method developed in this work;
- as support to image analyses (chapters 4, 5 and 6), a version of centerlines

converted to points is stored in two tables: **cenline_point15** and **cenline_point30**. The points are plotted each 15 and 30 m respectively. A special field (*point_seq*) holds the number of each point in sequence along the glacier centerlines, from glacier fronts to ice divisors;

- the **sar_thresholds** contains thresholds in altitude used as input to SAR classifier algorithms (see chapter 5.5), and to validate classification results;
- a list of glaciers which can be classified by images from a specific sensor, acquired in a defined frame/track (SAR data) or path/row (optical images) is stored in the table **img_glaciers**. Furthermore, this table holds information on the possible type of analysis (i.e., complete analysis, glacier front only, and glacier zones only);
- the **glacier_zones** table holds classes of glacier facies as extracted from classified images using points from the table cenline_point30; and
- final results in the form of points representing boundaries between glacier zones along the centerlines are stored in the table **glacier_zones_limits**. Each point is related to an analysis and has information on the type of the boundary (i.e., glacier front, snow line, wet snow line, dry snow line) and altitude of the point as extracted from RAMP DEM.

Web access interfaces were developed both for human interaction and for machine to machine communication. A browser-based interface allows users to query the glacier data base using text search or through interactive maps. The machine-to-machine accessibility is based on open web services implementing Open GIS Consortium (OGC) specifications and relevant ISO TC211 standards. Querying and retrieving spatial features and their attributes through an OGC Web Feature Service (WFS) interface for example enables interoperability with other OGC compliant applications such as GIS packages or spatially enabled data mining tools at the feature level.

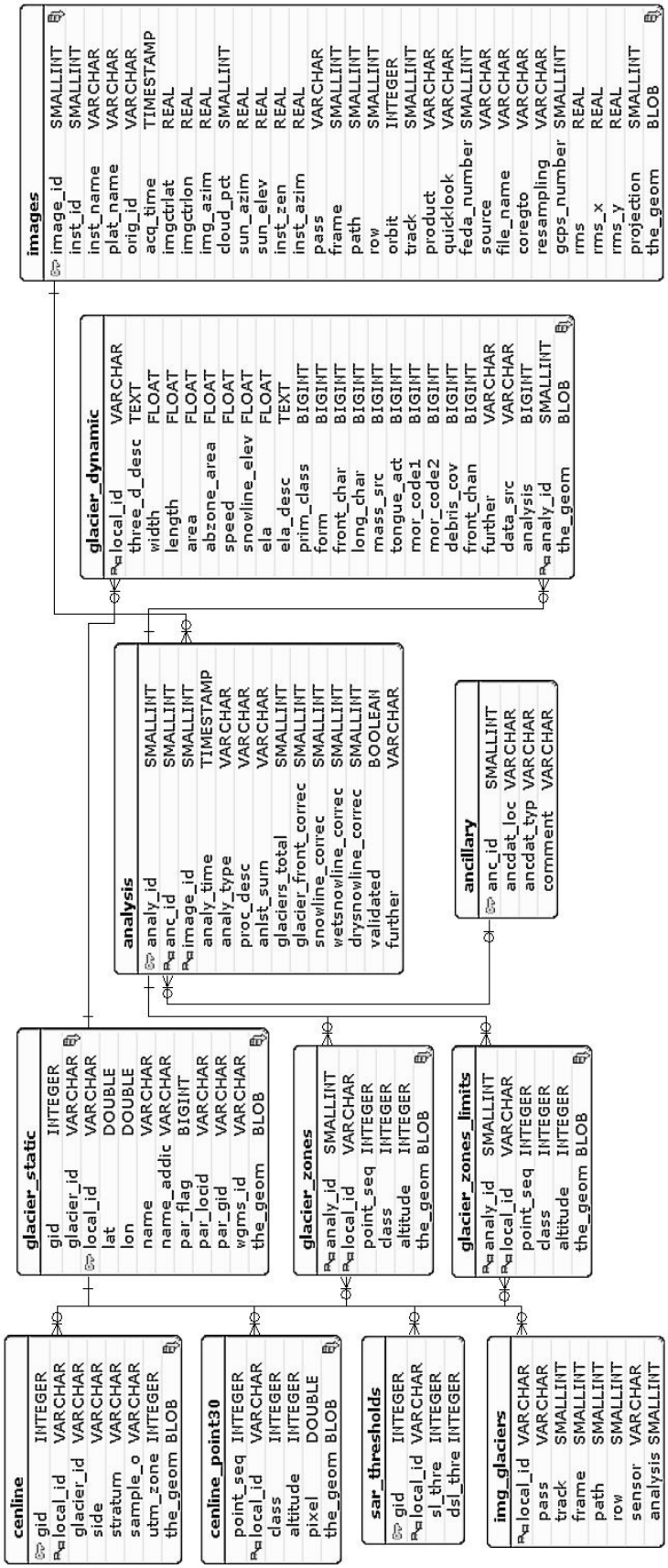

Figure 2.7: *Entity relation diagram of the Antarctic Peninsula Glacier Database. Boxes correspond to tables and its fields, and lines connecting tables represent table relationships. The relational structure of the database facilitates the record of additional cryospheric data resulting from further projects.*

3 The centerline approach

As outlined in chapter 2.1, distinct facies or zones are observed on glaciers. The development of these glacier facies are influenced by local and regional climatic and meteorological settings (Williams et al., 1991; Ramage and Isacks, 1998). Therefore, their time-depending variations are considered as good indicators of climatic changes (Rau et al., 2001). The present chapter describes a new method for monitoring spatial and temporal changes in the extent of glacier facies and in glacier frontal position using satellite imagery.

3.1 Method overview

Current glaciological studies on the Antarctic Peninsula (AP) are based on a few glaciers unevenly distributed along this region. Nevertheless, as stated in chapter 2.2, a huge amount of satellite data is available for the peninsula and would enable the study of many glaciers with reduced logistics costs. To allow the processing of such satellite datasets and the monitoring of a representative set of glaciers in a regional context for the AP, automatic procedures for image analysis are required. Hereby, glacier variations can be analysed by using groups of glaciers selected for different regions of the peninsula (see chapter 8), while changes detected for one glacier alone are not considered representative.

The analysis of complete glacier catchments in an automatic workflow is complicated by geometric distortions and the topographic effects of snow and ice

reflectance and backscattering. In addition, such level of detail is not essential for regional studies. Therefore, the simplification of the current methodology based on analyses of entire glacier surfaces is required. In this work, the classification of remotely sensed data is proposed to be limited to a small area along the glaciers centerline (Figure 3.1). A glacier's centerline is the analyst-interpreted line that approximately follows the main flow line of the glacier (Figure 3.1 and Chapter 3.3). Proposed by Saurer and Goßmann (2002), the so-called **centerline approach** consists of using the glacier centerline to select a 600 m wide buffer zone (centerline image) which is used for image analyses. The width of the centerline images (600 m) was defined so as to include enough neighbours for each pixel along the centerline, which enable filtering processes and multispectral classification. In a further step, the centerlines are used to extract the classes (glacier facies) from the raster file. The extent of the glacier facies along the centerline can be regarded as representative for the glaciers and are incorporated in the AP glacier database (see chapters 4, 5 and 6).

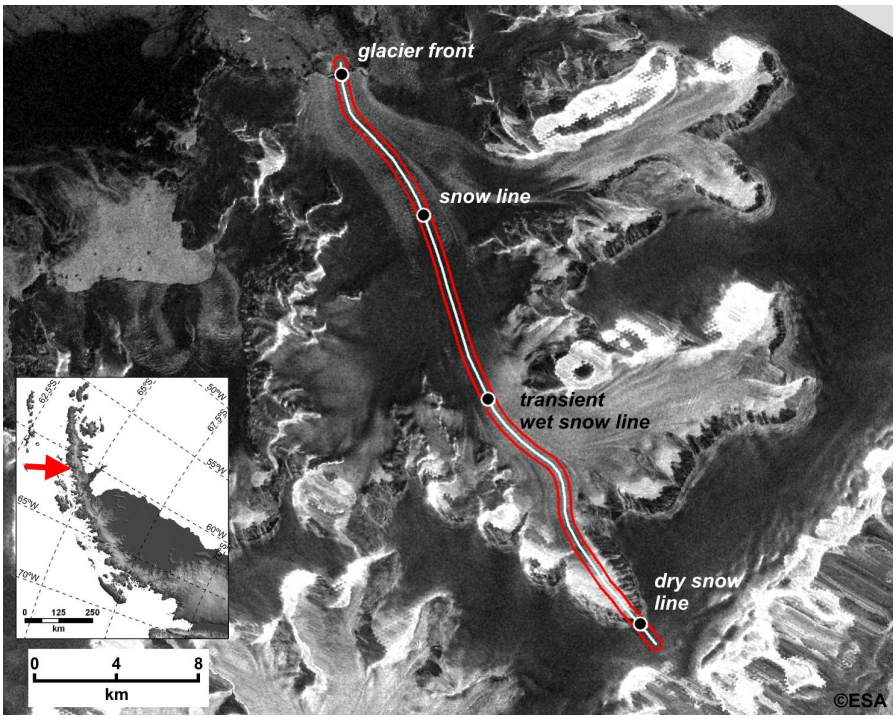

Figure 3.1: *Subset of an ERS-2 SAR image acquired on 23 February 2000 (orbit: 25328, frame: 4941) showing the glacier centerline (white line), the area used for image analysis in the centerline approach (red polygon), and the position of boundaries between glacier facies along the glacier centerline (black points).*

3.2 Facilitation of classification process

Some characteristics inherent to SAR and optical imagery cause problems when processing data acquired on glaciers. For example, geometric displacements caused by terrain relief are difficult to be corrected without a high-resolution DEM (Kwok et al., 1987). Furthermore, the radiometric information is affected by pixel saturation, shadowed illumination (Sidjak and Wheate, 1999), and anisotropic reflectance of snow surfaces (Dozier and Painter, 2004). By segmenting the images to be analysed, the centerline approach minimises many of these problems.

3.2.1 SAR data

SAR images have characteristic relief displacements (Figure 3.2a, see Lewis and Henderson (1998) or Lillesand and Kiefer (2000) for a comprehensive description about SAR geometry and inherent distortions) which causes problems to occur during the interpretation and classification of the data. These relief-introduced geometric distortions are grave in areas with rough topography, like the AP, where typical images look similar to figure 3.2a. Hence, the use of SAR images without terrain correction limits the integration of this data with other kinds of geospatial information (e.g., vector data, optical imagery).

To correct for relief displacements, a DEM containing a spatial resolution and accuracy compatible with terrain features is necessary (Kwok et al., 1987). As stated in chapter 2.3.2, a high resolution DEM is not available to be used in a productive workflow of orthorectifying SAR images on the AP. By using the RAMP DEM, the results are not satisfactory if we consider the whole glacier catchment area. Figure 3.2b depicts remaining distortions at the north and south divisors of the Victory Glacier. However, considering the glaciers selected for analysis (chapter 3.3), the terrain slope along the centerline is normally smooth (less than 10 degrees, Figure 3.2c). An exception is the stepped transition between the plateau and glacier valleys. Thus, using the centerline of images to analyse

altitudinal changes of boundaries between glacier facies, high positional errors resulting from the use of RAMP DEM are restricted to areas where the plateau breaks down to the glaciers (see chapter 5.3.3).

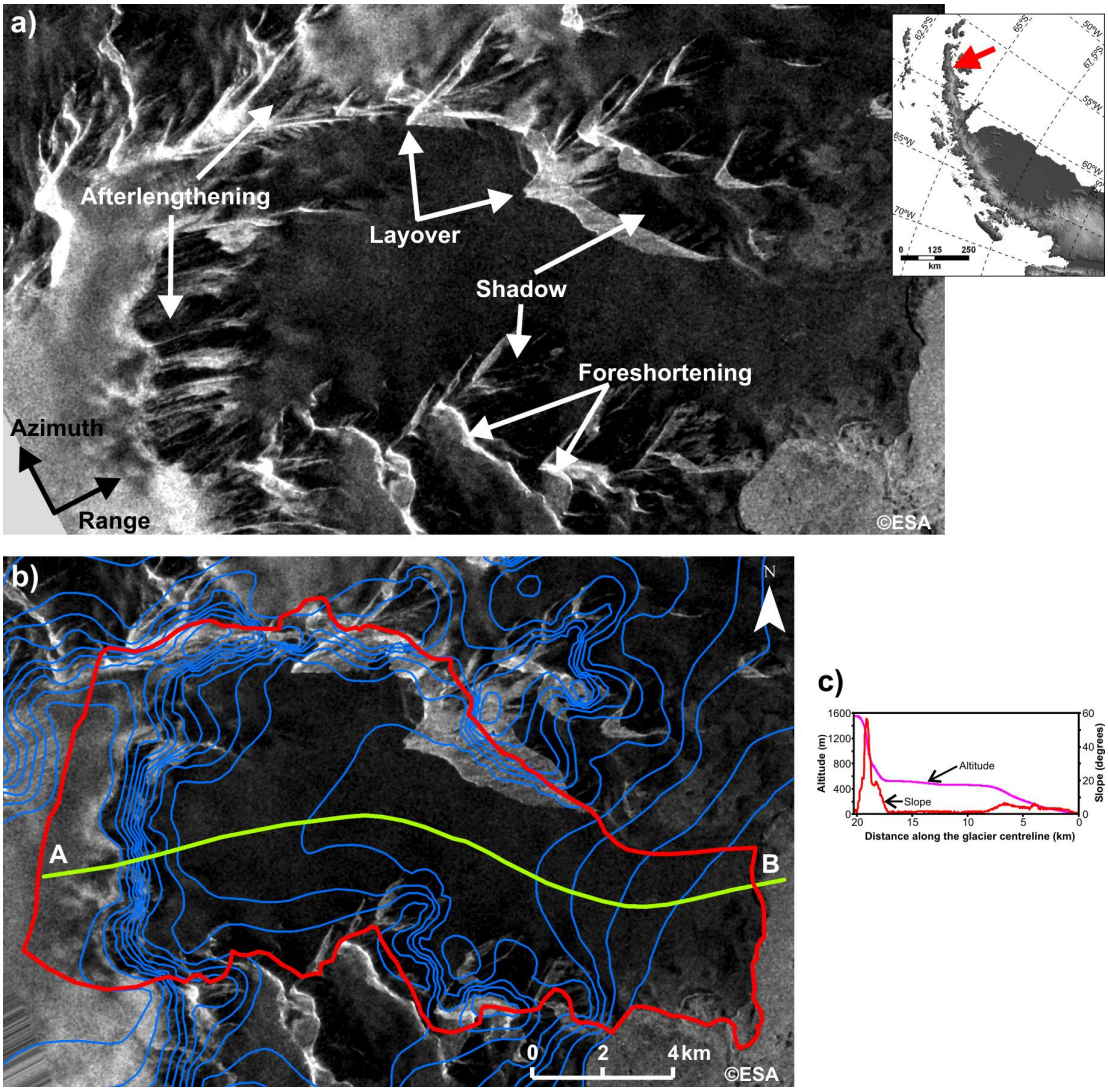

Figure 3.2: *Subset of an ERS-2 SAR image acquired on 18 January 2002 (orbit: 35271, frame: 5877). a) Examples of relief displacements occurring in SAR data due to the rough topography of the Antarctic Peninsula. b) Image subset orthorectified using the RAMP DEM. The red line are boundaries of the Victory Glacier, the blue lines are contour lines at intervals of 100 m, and the green line is the glacier centerline. The flow direction is from A to B. c) Profiles of altitude and slope along the glacier centerline shown in b.*

Besides dependence on sensor parameters and sensor-target geometry, the backscatter signal recorded on glaciers and ice sheets depends on snowpack parameters (e.g., liquid water contend, snow density, stratigraphy, grain size, and

surface roughness) (Foster et al., 1996; Ramage and Isacks, 1998). As the backscatter values of dry snow and frozen percolation radar zones are resulting from volume scattering (Fahnestock et al., 1993), small changes in terrain slope and aspect along the centerlines will not affect the classification of these zones. The adjacent wet snow radar zone and bare ice radar zone, whose thresholds in backscatter values are relatively near (Figure 2.1), will profit from the restriction of the analysis to areas with smooth slopes near the centerline.

3.2.2 Optical data

Geometric distortions in optical images are dependent on the distance to the nadir line and altitudinal variations. Seidel and Martinec (2004) showed a good numerical example of horizontal displacements in a Landsat TM scene covering an area with altitudinal gradient of about 3000 m. According to the authors, the highest root mean square error (RMSE) values range between 176-252 m and are found in areas of high topographic variation which occur mainly near the borders of the scene (distant from the nadir line at the centre of the image). On the AP north of 70º S, the highest areas on the plateau are lower than 2500 m a.s.l., with exception of some peaks in northern Palmer Land (Figure 1.1). So, expected positional errors by not considering topographic effects on optical imagery are about 1 pixel of the RAMP DEM (200 m) in the worst cases. Furthermore, by limiting the analysis to the central area of the glaciers, terrain distortions on ridges and peaks are eliminated.

The radiation reflected by glacier surfaces and detected at satellite level is strongly affected by the sun-surface-satellite geometry (Dozier and Painter, 2004). Figure 3.3a depict two main effects resulting from the terrain influence: (1) saturation; and (2) shadowed illumination. Saturation and high values of reflectance (Figure 3.3a, red arrows) are detected on sun-oriented surfaces with steep slopes, due to the forward component of the anisotropic reflectance on snow surfaces (Dozier and Painter, 2004). Shadowed illumination are characteristics from surfaces without direct solar illumination (Figure 3.3a, blue arrows), and is considered a challenge in the classification of glacier surfaces (Sidjak and Wheate, 1999; Heiskanen et al.,

2003). Painter and Dozier (2004) showed that the variability in the hemispherical-directional reflectance factor (HDRF) for near-nadir sensors is negligible. As Landsat TM and ETM+ are nadir viewing sensors, and Terra ASTER data is operationally acquired within an angular range of ± 10° from nadir (Terra ASTER has an off-nadir scan of ± 24°), we are able to neglect the anisotropic reflectance by analysing areas with smooth slopes near the centerline.

Simply by using the centerline image, many areas affected by topographic effects are not considered in the analysis (Figure 3.3b). Figure 3.3c-d show products from unsupervised classification (ISODATA algorithm, 6 classes) performed on the image subsets depicted in figure 3.3a-b respectively. Two classes correspond directly to the bare ice and dry snow zones, whereas the last one represents the freshly-fallen and slightly-metamorphosed snow. As found by Williams et al. (1991), the wet snow zone was further classified as two distinct zones (Figure 3.3.c-d): (1) a zone of snow supposed to be saturated with water (slush zone); and (2) snow highly metamorphosed by melting and refreezing cycles. Some pixels of the bare ice zone were misclassified as rock using the whole glacier basin, but accurately classified as bare ice with the centerline image. Areas affected by the topography or classification errors correspond to 26.18% of the glacier basin in figure 3.3c, while it corresponds to only 9.12% of the centerline image in figure 3.3d.

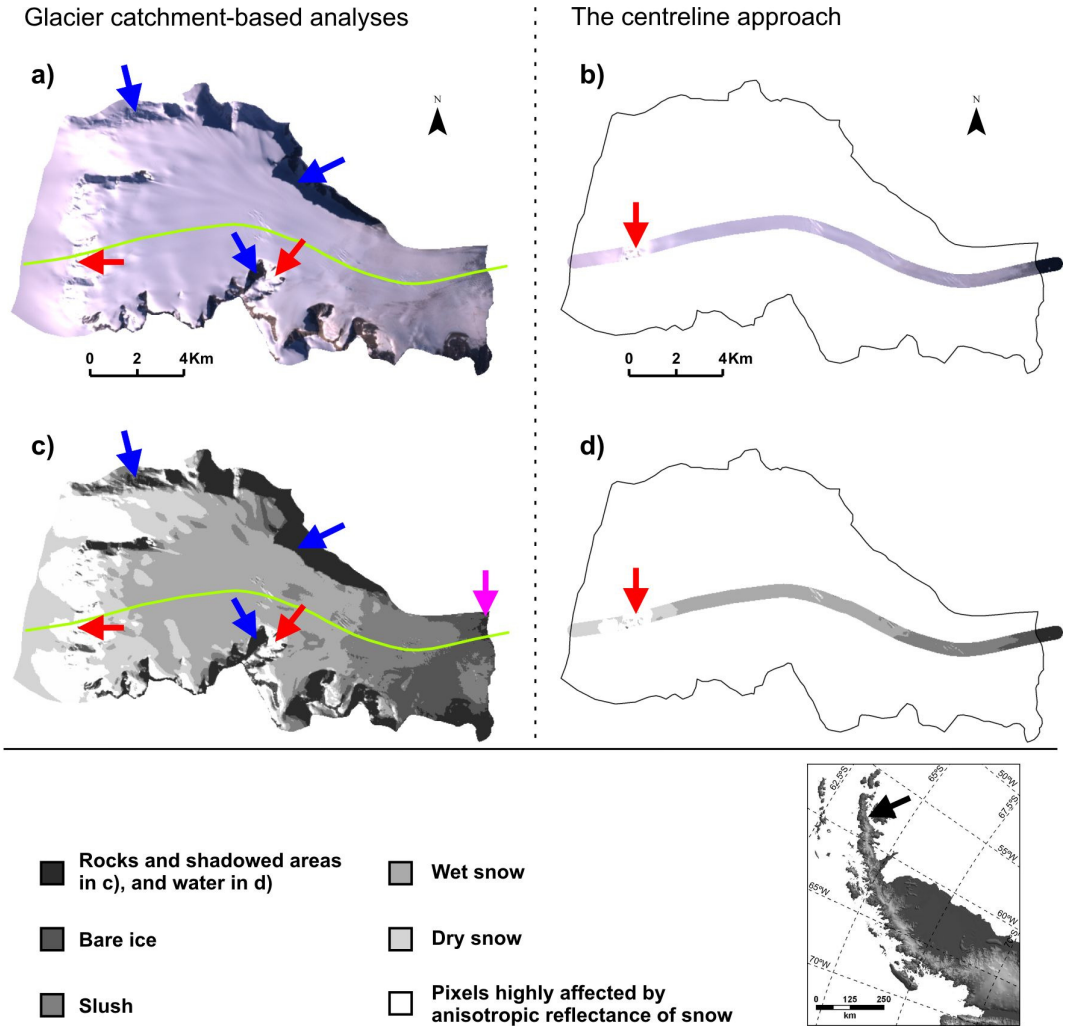

Figure 3.3: *Subsets of the Landsat ETM+ scene acquired on 21 February 2000 (path: 216, row: 105, sun elevation angle: 26.4º, solar azimuth: 56.5º) and respective products of unsupervised classification. a) Subset of the ETM+ scene covering the whole Victory Glacier, the green line is the glacier centerline, b) Subset of the ETM+ image covering a buffer area of 300 m around the glacier centerline on Victory Glacier, c) and d) Products of unsupervised ISODATA classification applied on a and b respectively. The red arrows show areas of pixel saturation resulting from topographic effects (a and b), and misclassification due to topographic effects on snow reflectance (c and d); the blue arrows show areas shadowed (a) and misclassified (c) because of topographic effects; and the magenta arrow shows some pixels of the bare ice zone misclassified as rock.*

Besides visual interpretation and simple statistical measures, scatter diagrams (Figure 3.4a-b) yield a two-dimensional representation of the spectral classes. The scatter diagram of the centerline image (Figure 3.4b) shows better delimitation among classes in comparison with the diagram generated from the whole basin area (Figure 3.4a). It indicates the reduction of pixels located on the boundaries or in overlapping regions between classes.

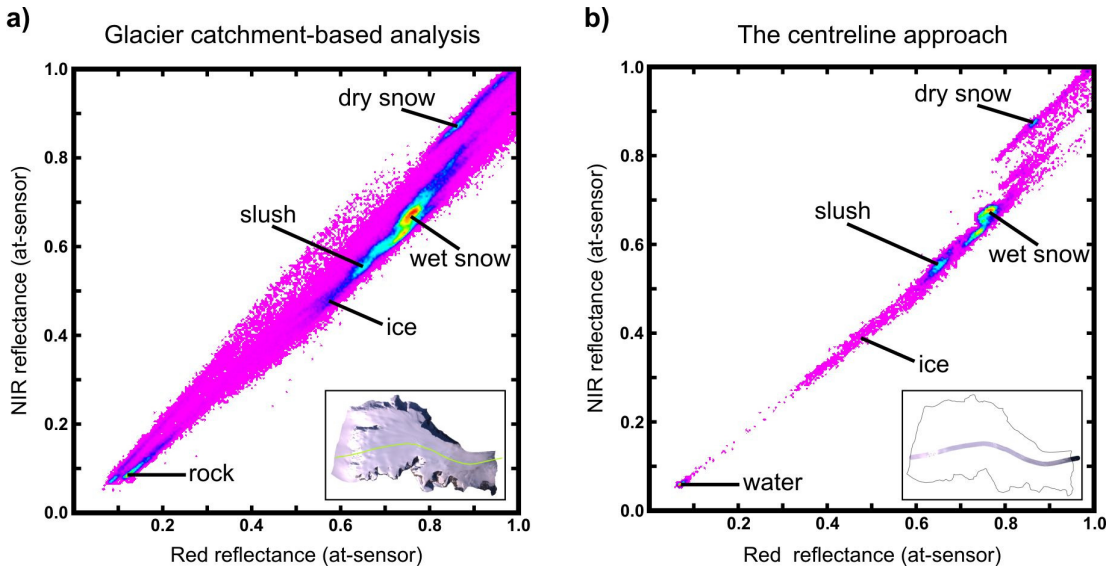

Figure 3.4: *Scatter diagrams showing the delineation of spectral classes using the red and near infrared bands of the images depicted in figure 3.3a-b. a and b correspond to 3.3a and 3.3b respectively. Hot colours represent higher concentration of pixels. The clusters of pixels with low values of reflectance correspond to different classes in each diagram. It occurs because the centerline approach exclude rock outcrops from the analyses, but to detect changes in glacier frontal positions, this approach analyses areas beyond glacier fronts.*

3.3 Digitalisation of glacier centerlines

As stated in chapters 2.2 and 2.3.3, the ice masses selected initially for analyses consist of 560 glaciers located north of 70°S. However, due to relief displacements caused in satellite images by the rough topography of the AP, it is not possible to monitor superficial zones in the complete population (i.e., all 560 glaciers). To define the glaciers for investigation, the selection was made based on practicality of analysis. Therefore, glaciers were selected when they are wide enough so as to avoid layover effects or shadows occurring in SAR and optical data respectively. A spatially representative sample of 240 glaciers resulted from this process (Figure 3.5). It corresponds to 42.86% of the glaciers catalogued on the Antarctica Peninsula north of 70ºS.

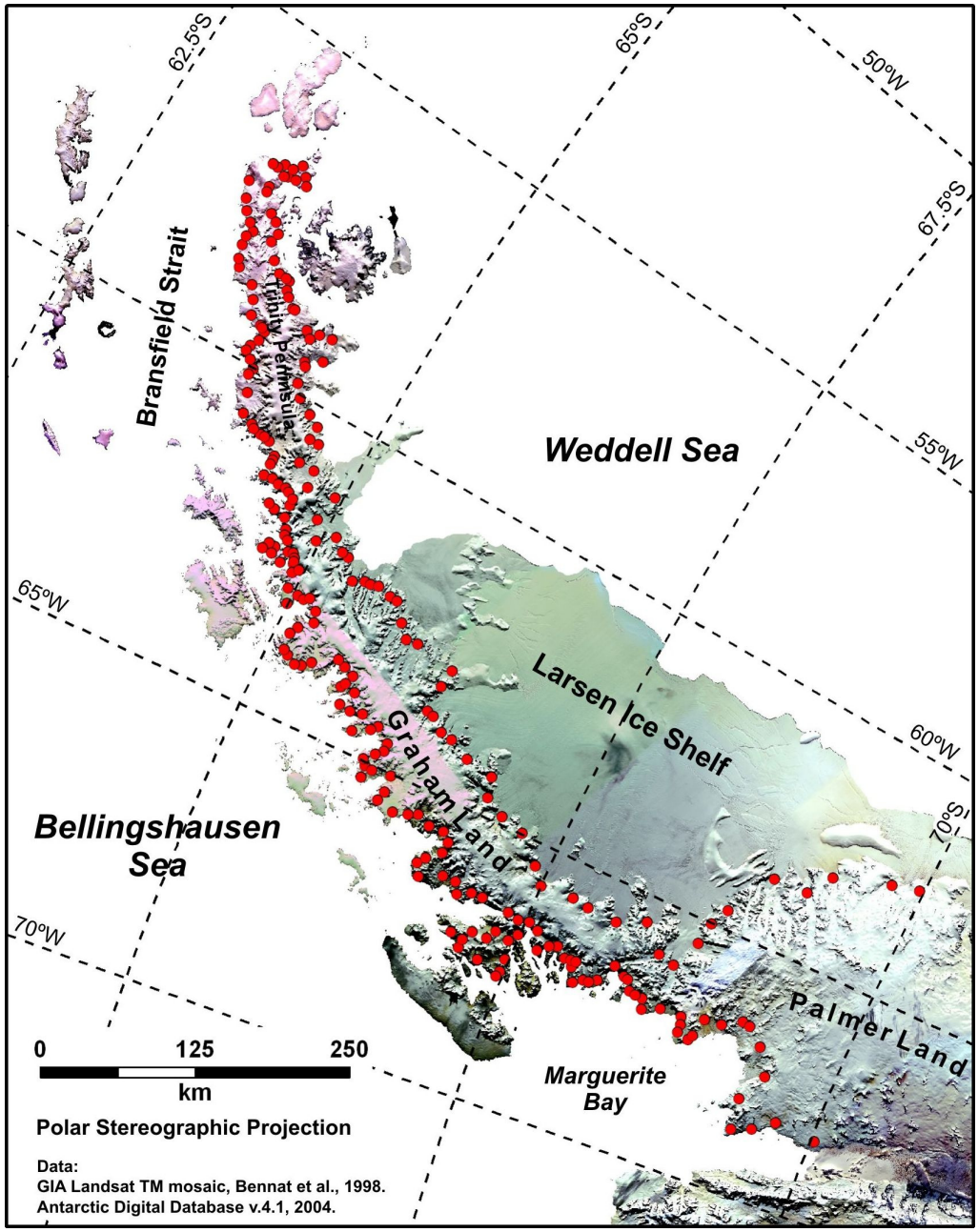

Figure 3.5: *Glaciers selected for analysis (240 at total). The red circles correspond to glaciers as represented in the Antarctic Peninsula glacier inventory. Note the good spatial distribution of the sample along the Antarctic Peninsula north of 70º S.*

Using the GIA Landsat TM mosaic and contour lines derived from RAMP DEM, glacier centerlines were digitised for each selected glacier. As stated in chapter 3.1:

> *a glacier's centerline is the analyst-interpreted line that approximately follows the main flow line of the glacier.*

Therefore, the centerlines position was determined by choosing a glacier-flow line located approximately at the centre of each glacier (see figures 3.1, 3.2b, and 3.6). In order to use vector topology in the classification algorithms, the lines were always digitised in the same direction, inverse to the glacier flow (Figure 3.6). To store the glacier centerlines in the AP database, a table called *cenline* was created.

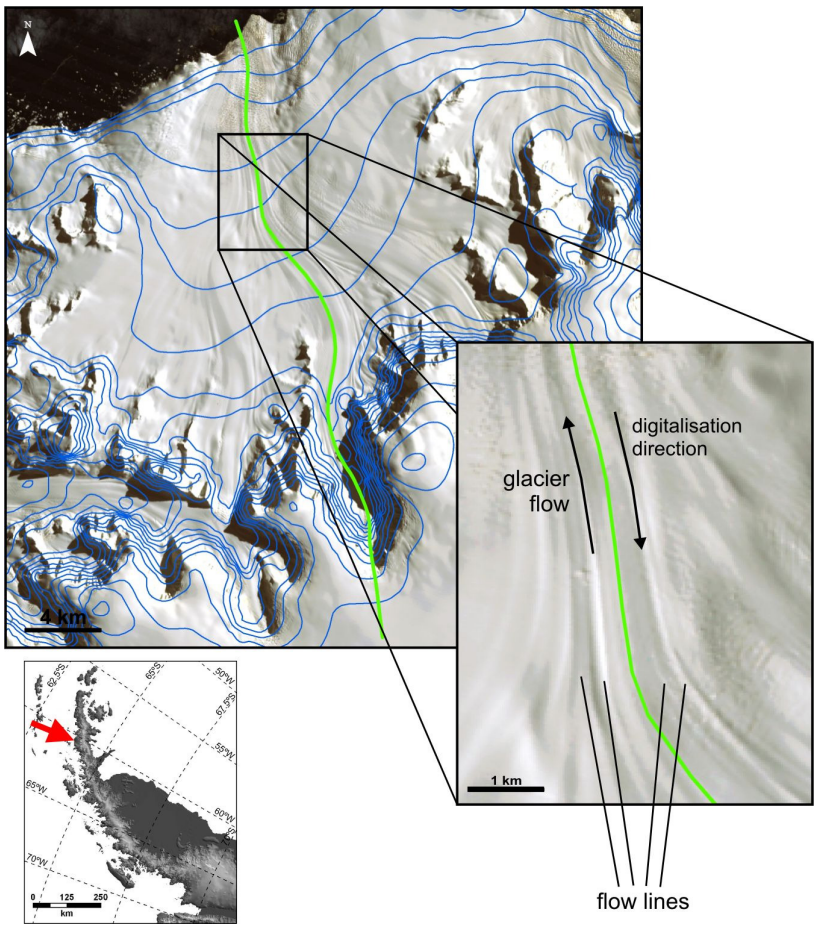

Figure 3.6: *Subset of the GIA Landsat TM mosaic (Landsat TM original scene acquired on 1st March 1986) with contour lines (blue lines) derived from RAMP DEM at intervals of 100 m. It corresponds to the settings used for digitalisation of the glacier centerlines. The green line is the glacier centerline of Victory Glacier.*

3.4 Advantages and limitations of the centerline approach

The use of the GIA Landsat TM mosaic as base for digitalisation of the glacier centerlines contribute to include the maximum extension of the glaciers in study during the last two decades. It is ensured by the fact that the oldest images to be analysed correspond to GIA's original scenes and the AP had a general pattern of glacier-front retreat in the time period considered (Rau et al., 2004; Cook et al., 2005). Although the digitalisation of the glacier centerlines was strongly depending on the analyst, as analyses for each glacier are always realized on the same centerline, any change detected will be related to the same reference.

By reducing the glacier area to be analysed to areas along the centerlines, we minimised the need of a high resolution DEM for orthorectification of SAR and optical data, and contributed to reduce topographic effects on glacier reflectance. It facilitates pre-processing and analysis of not only the multi-temporal image database available for this study, but also additional datasets archived at international data centres and those which will be acquired in the future.

On the other hand, due to relief-introduced geometric distortions on SAR and optical images, glaciers flowing through narrow valleys (up to1000 m wide) will not be analysed. It corresponds to almost 57% of the glaciers catalogued on the Antarctica Peninsula north of 70º S, and could mask or bias the statistical analysis to be carried out.

Glacier facies resulting from analyses of centerline images will consist of documented digital data to be incorporated in the AP glacier database. Nevertheless, these products correspond only to a small area along glacier centerlines, and do not meet the initial requirements of international projects of glacier inventorying and monitoring (e.g., the GLIMS project) based on analyses of complete catchment areas.

3.5 Selection of glaciers for validation of classification algorithms

The evaluation and development of algorithms for automatic classification of glaciers zones does not require all 240 glaciers selected for analysis. A sub-sample is sufficient if it represents the data variability of the main sample. So, in order to select a set of representative glaciers, it was decided on a stratified sampling. In this kind of sampling, the glaciers in study are divided into homogenous groups, before simple random sampling (Tryfos, 1996). It ensures the representation of each stratum in the sample, and reduces sampling variation due to possible dominance of some strata in the sample. The strata were based on geographic localisation and GLIMS glacier classification parameters (i.e.; frontal characteristics and longitudinal profile) stored in the AP glacier inventory (Table 2.3; Rau et al., 2005). The steps were as follows:

(1) the AP was divided in eastern and western sides;

(2) a coarse filter was applied to define strata. For this, matrixes of glacier frontal characteristics and longitudinal profiling (Table 3.1) were used.

(3) glaciers were divided into 18 strata, 9 strata on each side of the AP. Table 3.2 shows the strata defined and the number of glaciers for each strata;

Table 3.1: *Example of coarse filter (matrix) applied to define strata for stratified sampling. Each glacier was classified according to its frontal characteristic and longitudinal profiling. Only morphological classes with glaciers are represented here. For an overview about the GLIMS parameters to characterise morphological shape of glaciers see table 2.3.*

West Antarctic Peninsula		**Longitudinal profile**			
		Uncertain or miscellaneous	Even, regular	Cascading	Interrupted
Frontal characteristic	Normal or miscellaneous	1	1	0	0
	Piedmont	0	2	0	0
	Calving	0	15	23	3
	Calving and Piedmont	0	1	0	0
	Calving and Expanded	0	8	7	2
	Calving and Lobed	0	2	2	2
	Ice shelf nourishing	0	2	2	0
	Floating	0	30	44	11

Table 3.2: *Final strata defined by using geographic localisation, glacier frontal characteristics and longitudinal profiling. The number of samples for each stratum was calculated proportionally to the size of the sub-sample.*

Strata	West Antarctic Peninsula		East Antarctic Peninsula	
	Number of glaciers	Samples per stratum	Number of glaciers	Samples per stratum
Calving + Even, regular	15	3	5	1
Calving + Cascading	23	5	5	1
Calving + Interrupted	3	1	0	0
Calving and Lobed + Even, regular	0	0	3	1
Calving and Expanded + Even, regular	8	2	0	0
Calving and Expanded + Cascading	7	2	0	0
Ice shelf nourishing + Even, regular	0	0	15	3
Ice shelf nourishing + Cascading	0	0	27	6
Floating + Even, regular	30	7	8	2
Floating + Cascading	44	10	10	2
Floating + Interrupted	11	2	5	1
Others	17	4	4	1

(4) the size of the sub-sample was defined by using the formula (Tryfos, 1996):

$$n = \frac{NP(1-P)}{(N-1)D^2 + P(1-P)} \quad (1)$$

where n is the sub-sample size, N the population, *P* is the proportion of glaciers estimated to be classified precisely, 1 – *P* is the proportion of glaciers estimated to be misclassified, *D* is *c* divided by *Z*, *c* is the confidence level, and *Z* is the Z value for the confidence level required. For example, supposing the algorithm classifies accurately 90% of the sub-samples, and the confidence level and confidence interval are defined as 90% and ± 6% respectively. Thus, the size of the sub-sample is 54 glaciers;

(5) using proportionate allocation, a sampling fraction in each of the strata was calculated. It is proportional to that of the total population. For this, the following equation was used:

$$ns_i = \frac{n}{N} Ns_i \quad (2)$$

where ns_i is the number of sub-samples per stratum i, and Ns_i is the number of glaciers in each stratum (Table 3.3); and

(6) finally, the calculated amount of glaciers was selected inside each stratum by using simple random sampling. Figure 3.7 shows the glaciers selected to test and validate algorithms of image classification.

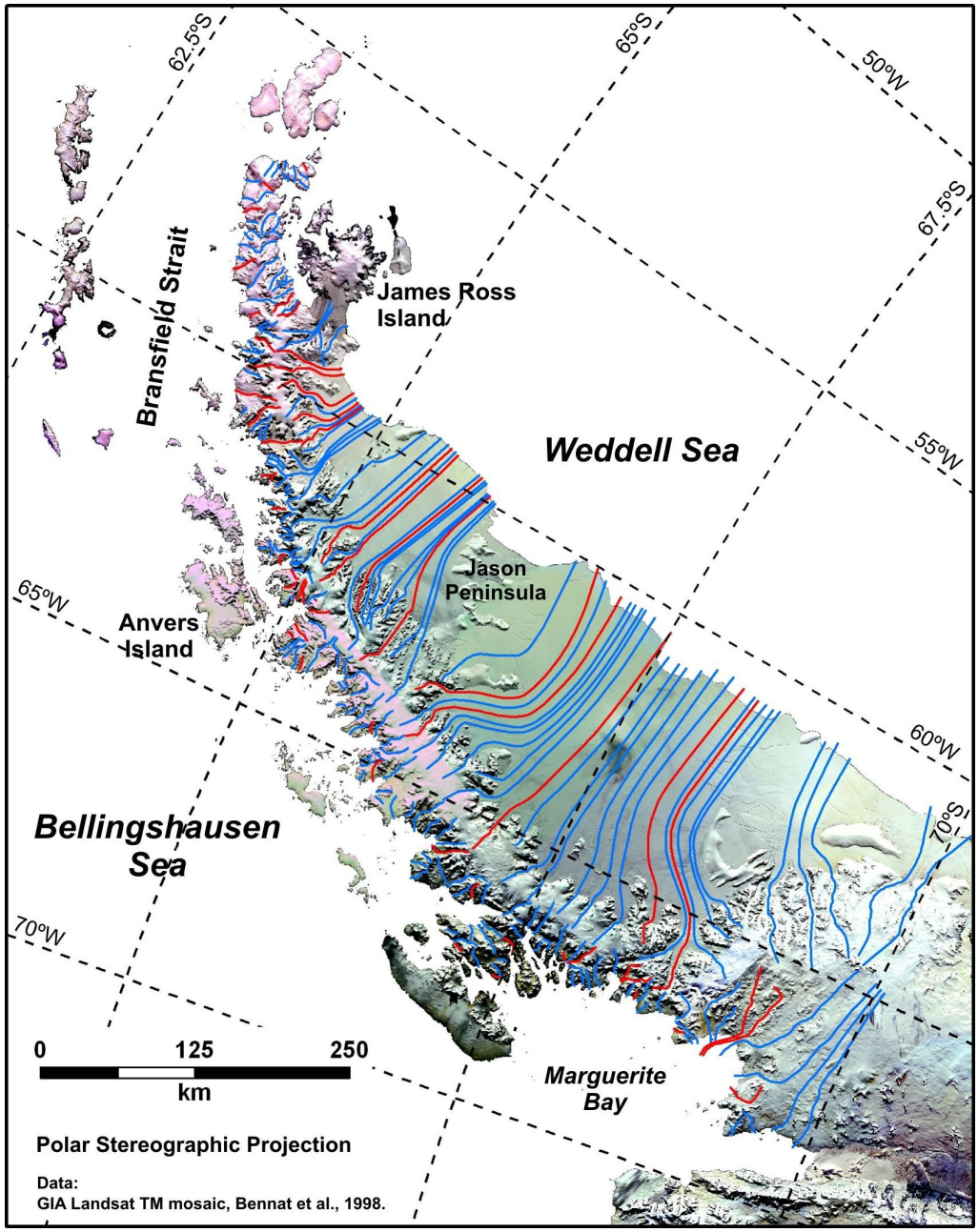

Figure 3.7: *Centerlines digitised on the 240 glaciers selected for this study. Red centerlines represent a sub-sample of glaciers (22.5%) selected for validation of algorithms for classification of glacier facies. The length of the centerlines corresponds to the maximum extent of the glaciers during the time period of analysis.*

Summary 3:

Chapter 3 describes a new method for monitoring spatial and temporal changes in glacier parameters using satellite imagery. The centerline approach facilitates the pre-processing and classification of remote sensing data acquired on glaciers. Furthermore, this approach enables the integration of remote sensing data from different sources, and minimises the needs of high resolution DEMs for terrain correction. Analysis resulting from the centerline approach will generate data for testing the initial hypothesis of spatial and temporal patterns of changes in glaciers facies in the Antarctic Peninsula.

A sampling method has also been described. It helps to select a representative subset of glaciers for evaluation of algorithms for classification of remote sensing data.

4 A multi-sensor data processing chain

This chapter describes the processing chain developed to extract glacier parameters from satellite imagery using the centerline approach proposed in chapter 3. In fact, only procedures valid for data from different sensors are explained here. Details about specific processes used for analyses of SAR and optical data are given in chapters 5 and 6 respectively.

4.1 Overview

In order to allow the processing of the huge satellite database described in chapter 2.2.1, an operational routine for classifying the boundaries between glacier facies was developed. It consists of five main steps (Figure 4.1):

(1) pre-processing of satellite sensor data;

(2) generation of centerline images;

(3) classification of glacier frontal position (a) and glacier facies (b);

(4) extraction of glacier frontal position (a) and glacier facies boundaries (b); and

(5) evaluation of classification and data ingestion in the Antarctic Peninsula glacier database (AntPenDB).

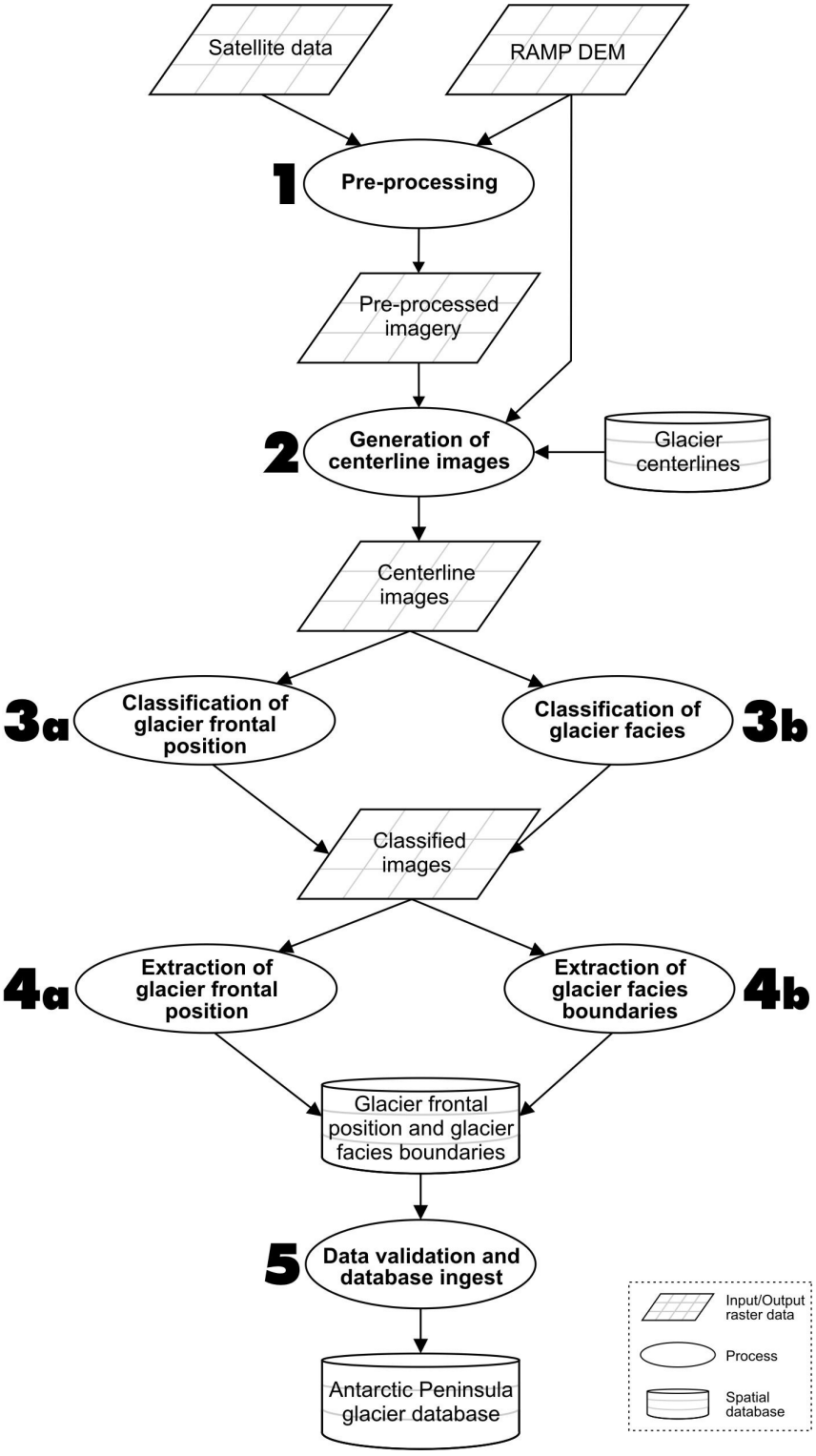

Figure 4.1: *Processing chain developed for classifying boundaries between glacier facies and glacier frontal position using satellite data. The numbers indicate the order of each step in the processing sequence.*

The implementation of the processing chain is based on three main software packages:

- the ESA **Basic Envisat (and ERS) SAR Toolbox (BEST)** version 4.0.3;
- the image processing software **Erdas IMAGINE** 8.7; and
- the open source relational database system **PostgreSQL** version 8.1 installed with the geospatial extension **PostGIS** 1.0.4.

In order to reduce the analyst's interaction with these softwares, automatic routines were developed using the programming language **PHP** (recursive acronym for PHP: Hypertext preprocessor) (http://www.php.net). PHP is a widely-used general-purpose scripting language initially developed for web applications. The extension **PHP-GTK2** (http://gtk.php.net) expands the functions of PHP by providing an object-oriented interface to GTK+ classes and functions (http://www.gtk.org). It greatly simplifies writing client side cross-platform graphical user interface (GUI) applications.

PHP-GTK2 was used for developing a GUI for input of images and complementary information for their processing (chapters 4.2-4.6). Then, PHP scripts write and execute batch files and SQL (Structured Query Language) queries respectively using the image processing softwares and database system mentioned above. The developed GUI and PHP scripts constitute an application called **IceTools**. It enables not only the classification, but also the management of tables from the AntPenDB used in this study (see chapters 4.3, 4.5 and 4.6). As a general rule, IceTools uses applications from PostgreSQL/PostGIS or Erdas IMAGINE when working with vector or raster data respectively. For radiometric correction and co-registering of SAR data, applications from BEST are used. So, IceTools requires a local installation of Erdas IMAGINE and BEST. PostgreSQL/PostGIS can run locally on the workstation used for image processing, or remotely on a server. The visualisation and evaluation of classification results can be done using any GIS package able to read shapefiles and the Erdas IMAGINE raster format. In this study study, ArcGIS is used for that. Figure 4.2 illustrates the corresponding software and programming tools used for each processing step described above.

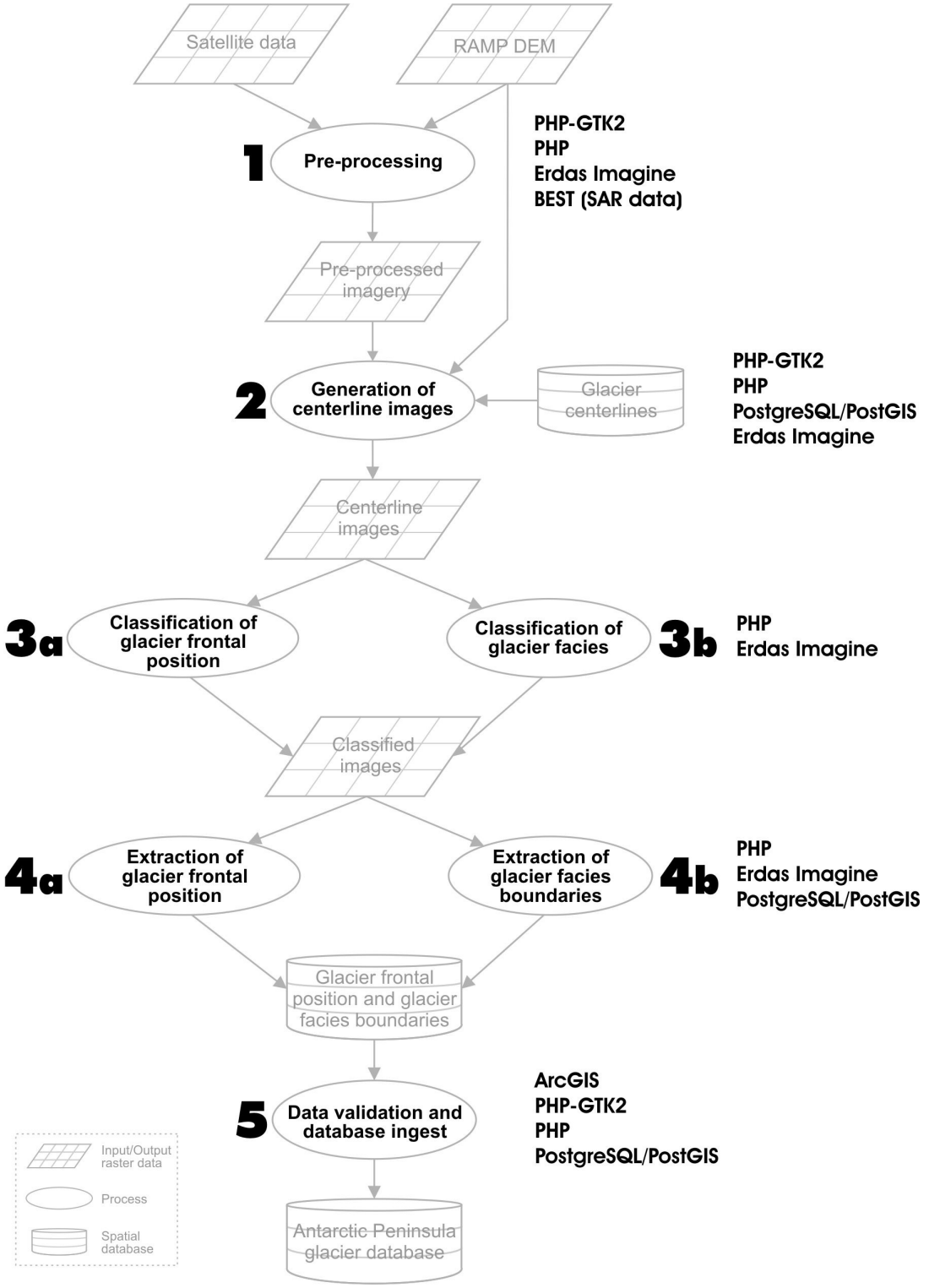

Figure 4.2: *Software packages and programming tools used for the implementation of the semi-automatic processing chain for classifying boundaries between glacier facies and glacier frontal position using satellite data. The numbers indicate the order of each step in the processing sequence. Details of processing for steps 2, 4 and 5 are described in this chapter. Steps 1 and 3 are sensor specific and therefore presented in chapters 5 and 6.*

By using the IceTools, **analyst's interaction** is almost restricted to data input and validation of results. Actually, it is required only on four occasions during the complete processing chain:

(1) input of satellite images to be pre-processed (see chapter 4.2);

(2) input of ground control points (GCPs) for geometric correction of satellite imagery (chapters 5.3.3 and 6.3.1);

(3) input of pre-processed imagery, RAMP DEM, and information on image acquisition for running the generation of centerline image and classification processes (chapters 4.3-4.5); and

(4) evaluation of classification results (based on the classification report) and correction of misclassified results (see chapter 4.6).

The next chapters provide a comprehensive description of the processing steps presented above.

4.2 Pre-processing of satellite imagery

This step of the processing chain prepares the data for classification. Basically, it consists in standardising the radiometric values and geospatial reference of the datasets, and comprises the following parts:

(1) radiometric calibration;

(2) speckle filtering (SAR data only); and

(3) geometric correction (i.e., co-registering and orthorectification).

The use of the developed IceTools enables batch processing of multiple images. The only exception is the geometric correction of satellite imagery, because this process requires the interactive input of GCPs. However, for data acquired on the same satellite orbit position (i.e., track/frame or path/row for radar or optical data respectively), GCPs are selected only for the first image analysed. As the pre-processing procedures are not the same for SAR and optical data, they are explained in detail in chapters 5.3 and 6.3 respectively.

4.3 Generation of centerline images

In this step, glaciers are selected for analysis and satellite images are segmented into smaller imagettes for classification purposes. It is done automatically after selecting the image to be analysed, the version of the RAMP DEM with the corresponding UTM zone, and giving some image information (Figure 4.3). Furthermore, by using the IceTools modules called *SAR Classifier* and *Optical Classifier*, the whole classification process is carried out in sequence (i.e., generation of centerline and glacier front images, classification of the limits between glacier facies and classification of glacier frontal position). Figure 4.3 illustrates the GUI of the application *SAR Classifier*. In contrast to information on pass, frame and track required here, the path and row numbers are needed when using the *Optical Classifier*.

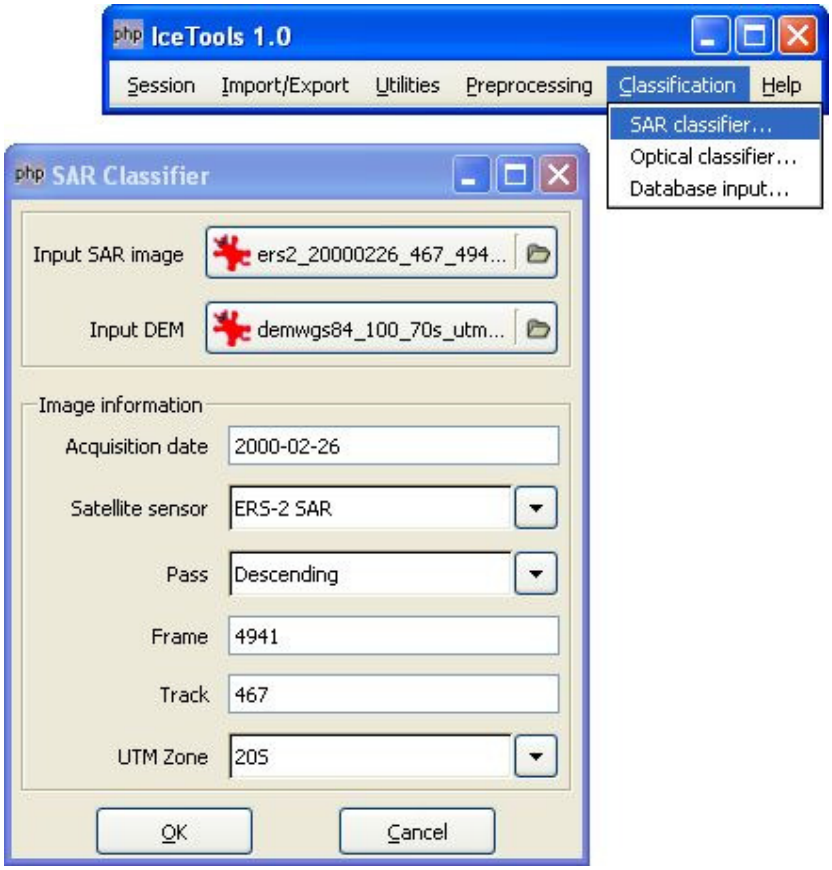

Figure 4.3: *Grafical user interface of the IceTools module for generation of centerline images and classification of radar glacier zones and glacier frontal position.*

The selection of glaciers is based on information previously recorded in the AntPenDB. Thus, before processing the first image from a specific frame and track (SAR images) or path and row (optical images), it is necessary to update the table *img_glaciers* with the glaciers that can be classified in this scene and the type of analysis (i.e., complete analysis, glacier front only, or glacier zones only). The type of analysis is defined as *glacier front* or *glacier zones* respectively when the central part or the front of a glacier is affected by image geometric distortions.

The sequence of steps for generation of glacier centerline and glacier front imagettes is as follows (Figure 4.4):

(1) the GUI of the *SAR* or the *Optical Classifier* is filled with the required information (e.g., Figure 4.3) and the process is started. Here, it is the only step that needs the analyst interaction;

(2) based on image information (e.g., satellite sensor, pass, frame and track, path and row, acquisition date), glaciers and their corresponding vector data are selected for analysis. In order to do that, the IceTools sends two SQL queries to PostgreSQL/PostGIS. The first selects the glacier centerlines from the *cenline* table, and the second selects the points representing glacier frontal positions for the nearest timestamp. Query results are temporarily stored as tables in the AntPenDB. A first set of glacier frontal positions was digitised for the 240 glaciers using the GIA Landsat TM mosaic as reference;

(3) using PostGIS geospatial functions, IceTools creates the masks for image segmentation. A first SQL query calculates buffer areas of 300 m around the selected glacier centerlines, generating 600-m wide strips (see figures 3.1 and 3.3). An additional SQL query also creates buffer areas (500 m) around the glacier fronts and computes the overlap areas with the centerline strips (Figure 5.7). The resulting polygons are then exported to shapefile using the PostGIS *pgsql2shp* program executed by IceTools; and

(4) by running a series of batch processes with Erdas IMAGINE applications, the IceTools converts the shapefiles to raster, and segments satellite images and DEMs. The results are glacier centerline and glacier front imagettes used for classification.

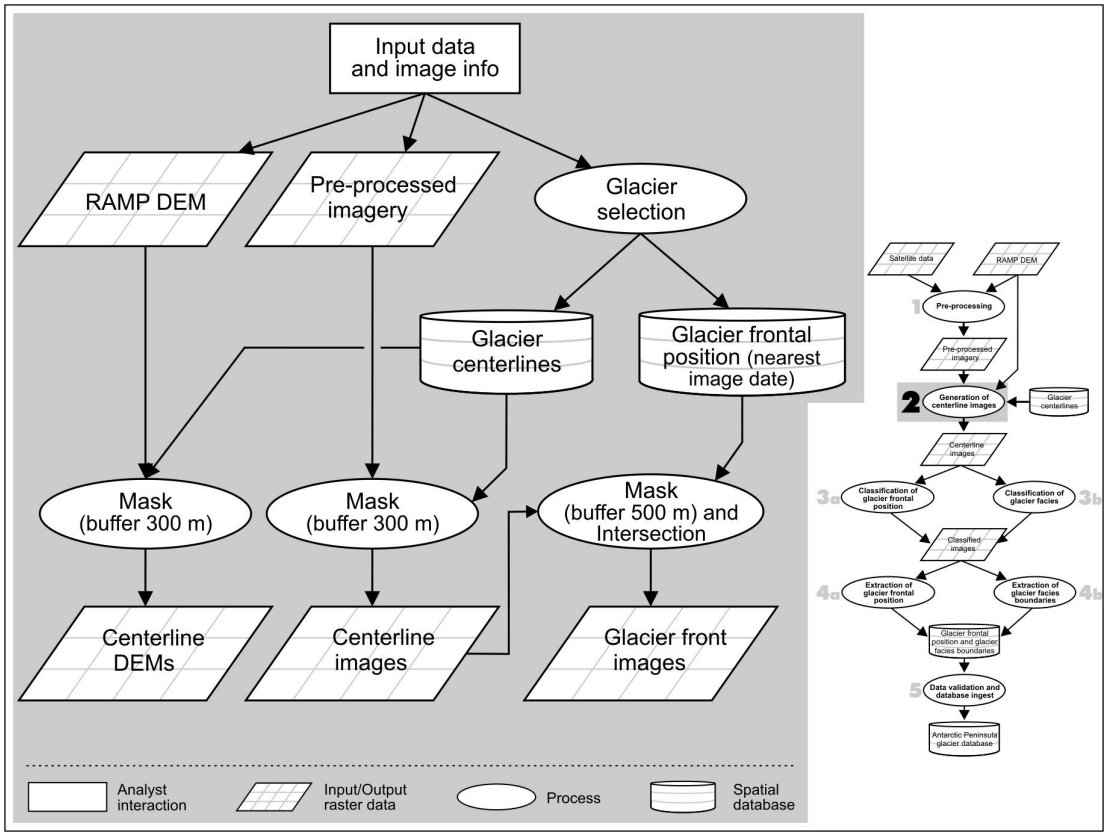

Figure 4.4: *Diagram illustrating the processing steps for generation of centerline and glacier front images .*

4.4 Classification of glacier frontal position and glacier facies

The classification processes are carried out in the same routine triggered by the IceTools modules *SAR Classifier* and *Optical classifier*. So, they are executed automatically after the generation of the centerline and glacier front imagettes. The modular design of the processing chain illustrated in figure 4.1 enables the use of specific classification methods for each kind of data. In this work, two methods are used for classifying glacier frontal position: texture analysis; and unsupervised classification. The first method determine the glacier front location, and the second one is used for automatic validation of the results. Furthermore, a knowledge-based algorithm was developed for classifying glacier facies using radar data and

multispectral supervised classification is used for optical data. The procedures are covered in detail in further parts of this thesis. Chapters 5.4 and 5.5 describe the algorithms implemented for classification of glacier frontal position and glacier facies using radar data, while chapters 6.4 and 6.5 present the corresponding algorithms used for data from optical sensors. The products of the classification are glacier frontal positions (point features) as determined by two different methods for each glacier analysed and classified imagettes (raster data) representing the glacier facies.

4.5 Extraction of glacier frontal position and limits between glacier facies

This processing step is the last automatic procedure of the routine started with the IceTools modules for image classification. At this point, the final glacier frontal positions are defined, the limits between glacier facies are extracted from the classified imagettes, and the classification report is written. The classification report indicates the glaciers whose glacier fronts or zonal boundaries possibly have to be corrected.

After the classification, the final **position of the glacier fronts** is determined as follows:

(1) glacier frontal positions are considered to be the data resulting from the texture analysis (see chapters 5.4 and 6.4). It is stored in a temporary table in the AntPenDB and exported to a shapefile to enable the validation of the classification results using a GIS package; and

(2) for each glacier, the glacier frontal positions as detected by both methods are compared. Whenever they are located two pixels or more from each other, a record is added to the classification report in order to enable the revision by the analyst (Chapter 4.6).

The determination of the **limits between glacier facies** consists of four parts:

(1) the classes from each classified imagette are extracted to the corresponding

points along the glacier centerline (table *cenline_point30*). In *cenline_point30*, points are plotted each 30 m, corresponding to the spatial resolution of TM, ETM+ and ASTER SWIR data (Table 2.2), and approximately to the nominal resolution of the SAR data (Table 2.1). Points on each glacier centerline are numerated by sequential identifier numbers (IDs) starting from the sea to the upper part of the glacier. The field *point_seq* holds the IDs;

(2) subsequently, starting after the glacier front, the algorithm searches the position of class boundaries. For example, the algorithm classifies the first point after the bare ice zone as the *snow line position* (Figure 4.5). If there is a wet snow zone on the glacier analysed, the algorithm searches the last point of this class and attributes it as the *transient wet snow line*. Furthermore, the first point of an existing dry snow zone is classified as the *dry snow line*;

(3) for each glacier, the altitude of the detected glacier zonal boundaries is compared with the thresholds in altitude from the table *sar_thresholds* (see chapter 5.5 or figure 5.8a for an overview on the altitude thresholds for classifying radar data). Whenever a snow line, wet snow line or dry snow line is located within 50 m of the corresponding threshold, a record is added to the classification report in order to enable the revision by the analyst (Chapter 4.6); and

(4) the derived glacier parameters are stored in a temporary table in the AntPenDB, and exported to a shapefile to make possible the validation of the classification results using almost any GIS package.

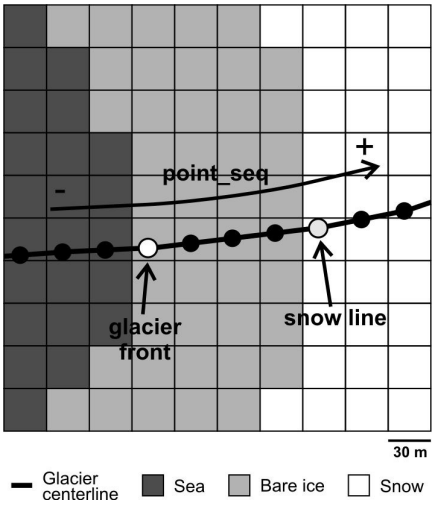

Figure 4.5: *Idealised representation of a centerline image subset. Starting after the glacier front, the algorithm classifies the first point after the bare ice zone as snow line. Points on each glacier centreline are numerated by sequential identifier numbers (IDs) starting from the sea to the upper part of the glacier. They are used to indicate the direction to be followed by the algorithm. The field point_seq holds the IDs.*

4.6 Data validation and database ingest

Although the algorithms implemented are quite robust, a brief visual inspection is suggested after the automatic classification. It validates the results and ensures the data consistency. The first procedure for that consists of displaying the classification results on the input image and can be done with any GIS package able to read shapefiles and the Erdas IMAGINE raster format. The classification report generated by IceTools indicates the glaciers whose zonal boundaries or glacier fronts possibly have to be corrected. Figure 4.6 illustrates the visual inspection of classification results using the software ArcGIS.

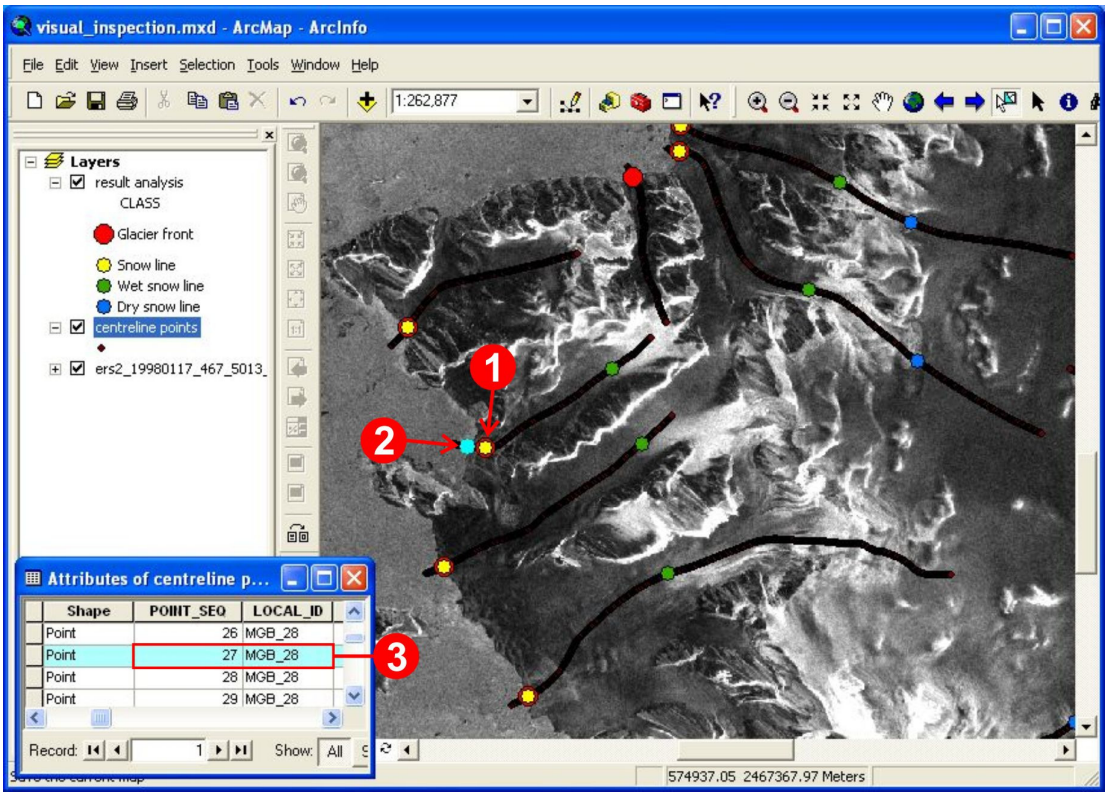

Figure 4.6: *Configuration of the desktop for visual inspection of classification results using the software ArcGIS. The arrows indicate misclassified ice front and snow line (1) and its the correct position (2). The red box (3) shows the local identifier (local_id) and the point number (point_seq) of the misclassified glacier.*

A routine was implemented to validate the classification, correct any eventual misclassification, ingest the resulting data in the corresponding AntPenDB table (*glacier_zones_limits*), and record an analysis report in the table *analysis*. Figure

4.7 illustrates a GUI developed to input the information needed for that. If any error is detected in the glacier frontal position, the local identifier number (*glacier local_id*) of the misclassified glacier and the point number (*point_seq*) corresponding to the correct frontal position has to be informed here. *Point_seq* is the sequence number of points along the glacier centerlines, from glacier fronts to ice divisors. For correction of limits between glacier zones, the code of the boundary to be corrected (2 = snow line, 3 = transient wet snow line, and 5 = dry snow line) is needed in addition to *glacier local_id* and *point_seq*.

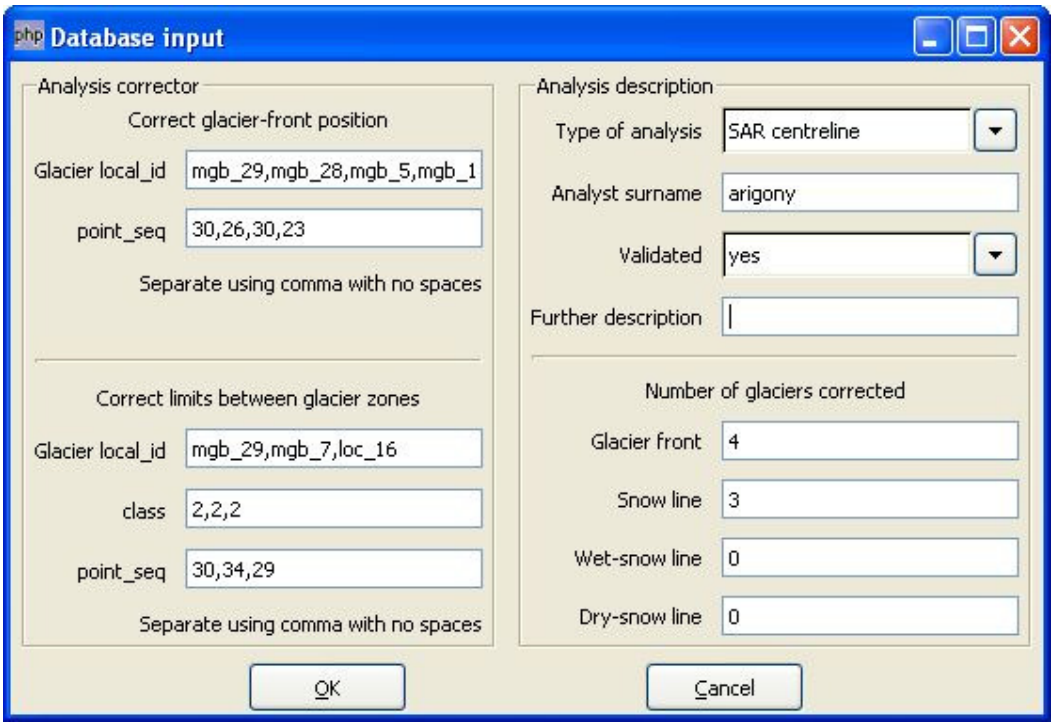

Figure 4.7: *Grafical user interface of the IceTools module for correction of misclassified results and database ingest of final results. It is used to input the data corresponding to the correct position of glacier fronts or glacier zonal boundaries (analysis corrector), and the information to document the analyses (analysis description).*

5 Classification of glaciers surfaces using SAR data

SAR data is available for the Antarctic Peninsula (AP) since 1991, enabling a 15-years record of changes in glacier parameters (chapter 2.2.1). Chapter 4 presented a semi-automatic processing chain developed to enable the processing of these satellite datasets. This chapter presents the glacier zones as detected by SAR sensors, and describes processing steps required specifically for analysing SAR data.

5.1 Backscattering characteristics of snow and ice surfaces

Besides sensor characteristics (e.g., band, polarisation, geometry of acquisition), the backscatter signal recorded on glaciers and ice sheets depends on snowpack parameters like liquid water contend, snow density, stratigraphy, grain size, and surface roughness (Foster et al., 1996; Ramage and Isacks, 1998). The configuration of these parameters at the moment of image acquisition produces: volume scattering (dry snow radar zone and frozen percolation radar zone) (Fahnestock et al., 1993); low surface scattering with radar signal almost completely absorbed by liquid water (wet snow radar zone); and surface scattering of a rough and dense surface (bare ice glacier zone) (Braun et al., 2000). It results in different backscatter values for each radar glacier zone (see table 5.1).

Table 5.1: *Overview on SAR backscatter coefficients (C-band) as reported by several authors for different sites. Modified after Rau (2004).*

Radar glacier zones	σ^0 [dB]	Study area	Author
Dry snow radar zone	-17	Antarctic Peninsula	Wunderle(1996)
	< -8	Greenland	Partington (1998)
	-20 to -14	Antarctic Peninsula	Rau and Saurer (1998)
	-18 to -14	Antarctic Peninsula	Rau et al. (2001)
Frozen percolation radar zone	-2 to 0	James Ross Island	Skvarca et al. (1995)
	-3	Antarctic Peninsula	Wunderle (1996)
	-7 to -3	Coast Range, Canada	Smith et al. (1997)
	-8 to -3	Coast Range, Alaska	Ramage and Isacks (1998)
	-4	Greenland	Partington (1998)
	-6 to -2	Antarctic Peninsula	Rau and Saurer (1998)
	-8 to -3	King George Island	Braun et al. (2000)
Wet snow radar zone	< -17	James Ross Island	Skvarca et al. (1995)
	< -15	Svalbard	Marshall et al. (1995)
	-22 to -11	Coast Range, Canada	Smith et al. (1997)
	-25.5 to -12	Coast Range, Alaska	Ramage and Isacks (1998)
	< -15	Alaska	Partington (1998)
	-17	Antarctic Peninsula	Wunderle (1996)
	-22 to -15	King George Island	Braun et al. (2000), Braun and Rau (2001)
Phase 2 melt radar zone	-8 to -6	Coast Range, Canada	Smith et al. (1997)
	-7.5 to -3	Coast Range, Alaska	Ramage and Isacks (1998)
	-8 to -4	King George Island	Braun et al. (2000)
Bare ice radar zone	-8	Svalbard	Marshall et al. (1995)
	-12 to -10	Coast Range, Canada	Smith et al. (1997)
	-12 to -10	Coast Range, Alaska	Ramage and Isacks (1998)
	-9 to -6	Alaska	Partington (1998)
	-15 to -10	Antarctic Peninsula	Rau et al. (2000)
	-13 to -10	King George Island	Braun et al. (2000)
	-12 to -8	King George Island	Braun and Rau (2001)
	-12	Svalbard	König et al. (2002)
Superimposed ice radar zone	-15	Svalbard	Marshall et al. (1995)
	-7.8 to -4.6	Svalbard	König et al. (2002)

5.2 Glacier zones as detected by SAR sensors

Several authors demonstrate the potential of data from radar sensors to identify distinct zones on glaciers (Jezek et al., 1993; Shi and Dozier, 1993; Fahnestock et al., 1993; Jezek et al., 1994; Forster et al., 1996; Albright et al., 1998; Partington, 1998; Ramage and Isacks, 1998; Rau and Saurer, 1998; Braun et al., 2000; Ramage et al., 2000; Rau et al., 2001; König et al., 2001; Rau and Braun, 2002).

In this context, the concept of radar glacier zones was firstly presented by Foster et al. (1996). Furthermore, a comprehensive classification scheme was proposed by Rau et al. (2001), and is used in this study. Hereby, the radar glacier zones correspond to four main classes:

(1) dry snow radar zone (DSRZ);

(2) frozen percolation radar zone (FPRZ);

(3) wet snow radar zone (WSRZ); and

(4) bare ice radar zone (BIRZ).

As the radar glacier zones depend on actual properties of the snowpack, their boundaries are dynamic on a time scale of days to weeks, showing clear seasonal variations (König et al., 2001). Therefore, these zones do not correspond directly to the glaciological glacier facies described by Paterson (1994). See chapter 2.1 for a comprehensive description of the classical glacier zones and a visual comparison with zones detected by SAR sensors. However, like the boundaries between classical glacier facies (chapter 2.1.6), the position of the limits between radar glacier zones (i.e., snow line, transient wet snow line, and dry snow line) is considered a proxy for information on glacier mass balance and actual or recent meteorological conditions (Forster et al., 1996; Rau et al., 2001).

5.2.1 Dry snow radar zone

Corresponding to the classical dry snow zone (see chapter 2.1.1), the DSRZ is the most stable zone detected by imaging sensors in the microwave region of the electromagnetic spectrum. Nevertheless, studies based on backscatter modelling showed that single strong snow melt events can move its lower limit (i.e., the dry snow line) upwards for a time range of several years (Rau et al., 2001). This zone is characterised by very low backscatter values (Table 5.1). It occurs because of the high penetration of the radar beam (Ulaby et al, 1986) and dominating volume scattering. Variations in sigma nought are expected to be resulting from differences in grain-size (Partington, 1998) caused by regional differences in patterns of snow accumulation and wind compaction (Fahnestock et al., 1993; Jezek, 1999).

5.2.2 Frozen percolation radar zone

In this zone, the successive events of melt-freeze metamorphism generate large snow grains which act as strong scatterers of the radar beam, producing significant volume scattering. In addition, the vertical (e.g., canals, ice glands) and horizontal structures (e.g., ice layers or lenses) occurring in this zone can reach dimensions similar to the wavelength of the SAR, producing strong signal returns (Fahnestock et al., 1993). The FPRZ has the highest values of backscatter (Table 5.1).

5.2.3 Wet snow radar zone

The development of a WSRZ on glaciers is caused by the occurrence of surface melting in the ablation season. As the radar signal is drastically absorbed by liquid water, the penetration depth in the snowpack is diminished to the uppermost centimetres. For example, 2 Vol. % of liquid water in the snow cover reduces the penetration depth of the radar beam to approximately 1 wave length (Ulaby et al., 1986). Hall (1998) gives a penetration depth of 1-4 cm when the liquid water content rises to 4-5% in the snowpack. With the development of the WSRZ, the dominant scattering mechanism changes from volume scattering to low surface scattering with radar signal almost completely absorbed by liquid water. Therefore, the WSRZ is characterised by very low backscatter values (Table 5.1).

5.2.4 Bare ice radar zone

In the BIRZ, the return of the radar signal is dominated by scattering of a rough and dense surface, resulting in low backscatter returns (Table 5.1) (Ramage and Isacks, 1998). The use of the upper boundary of the BIRZ (i.e., snow line) as a proxy for the equilibrium line is most useful from late summer to early winter conditions, when the snow accumulated in the last accumulation season was lost by melting (late summer) or the new fallen snow is transparent to the radar signal (winter). By increasing the volume scattering in the new deposited snow, melt-

freeze cycles can generate higher backscatter values and mask the last year snow line (Braun and Rau, 2001).

5.2.5 Further radar glacier zones

Some authors identified the occurrence of a metamorphosed WSRZ (Smith et al., 1997; Ramage and Isacks, 1998; Braun et al., 2000), called **phase 2 melt radar zone**. Here, the brightness of the return (Table 5.1) is attributed to the roughening of the surface due to wet-snow metamorphism (Smith et al., 1997). As the occurrence of the phase 2 melt radar zone was observed at the AP only once (Braun at el., 2000), it is not considered in this study. However, if this zone occurs, it will be firstly misclassified as frozen percolation radar zone, but will not be considered for the determination of the glacier zonal limits (chapter 4.5).

According to Marshall et al. (1995) and König et al. (2002), an area of superimposed ice (i.e., the **superimposed ice radar zone**) can be identified in SAR data. It corresponds to the high-density refrozen ice zone formed between the wet snow and the BIRZ (Partington, 1998). However, the backscatter values reported by the studies cited above are contradictory (Table 5.1). Marshall et al. (1995) described typical values around -15 dB, which are resulting of the greater degree of smoothness relative to glacier ice. On the other hand, Köning et al. (2002) found values between -7.8 to -4.6 dB. These authors suggested that the higher backscatter values relative to glacier ice are caused by the greater quantity of ice bubbles in the superimposed ice. Because of the needs of concurrent and extensive field data for accurate interpretation of the superimposed ice radar zone, it is not considered in this work. Nevertheless, in case of occurring superimposed ice, it will consist of small patches (F. Rau, personal communication, 2006) which will be eliminated during the post-classification (see chapter 5.5). So, it will not cause problems for the accurate determination of the snow line position.

5.3 Pre-processing of SAR data

This chapter explains the procedures adopted for preparing ERS-1/2 SAR and Envisat ASAR data for classification. It consists of the following parts:

(1) radiometric calibration;

(2) speckle filtering; and

(3) geometric correction (i.e., orthorectification).

The use of IceTools enables batch processing of multiple images. The only exception is the orthorectification of SAR data, because this process requires the interactive input of GCPs. However, as described in chapter 5.3.3, images from the same track and frame are automatically co-registered and GCPs are selected only for the first image analysed. Figure 5.1 shows the GUI used for input of image information used for writing of batch files and automatic processing of radiometric calibration and speckle filtering, using executables from BEST and Erdas IMAGINE respectively.

5.3.1 Radiometric calibration

Radiometric calibration consists of using the ESA Basic Envisat and ERS SAR Toolbox (BEST) (http://earth.esa.int/services/best/) for calculating the backscattering coefficients (sigma nought: σ^0). For this, BEST uses the algorithm developed by Laur et al. (2004):

$$\sigma^{o}_{linear} = \left(\frac{1}{N} \times \sum_{i,j=1}^{i,j=N} DN_{ij}^{2} \right) \times \frac{1}{K} \times \frac{\sin\alpha}{\sin\alpha_{ref}} \tag{3}$$

where σ^0_{linear} is the backscattering coefficient of a distributed target in the image, N is the number of pixels within the area of interest (AOI) (i.e., the group of pixels corresponding to the target), i and j are the range and azimuth locations of the pixels within the distributed target containing N pixels, $DN_{i,j}$ denotes the pixel intensity value corresponding to the pixel at location (i,j), K is the absolute calibration constant, α is the average incidence angle within the distributed target, and α_{ref} the reference incidence angle (i.e., 23°). Here, two assumptions on the

local incident angle (α) were made by Laur et al. (2004): first, a flat terrain is considered, where the incident angle is depending only on the ellipsoid and varies from about 19.5° at near range to about 26.5° at far range; and second, any change in incident angle across a distributed target is neglected.

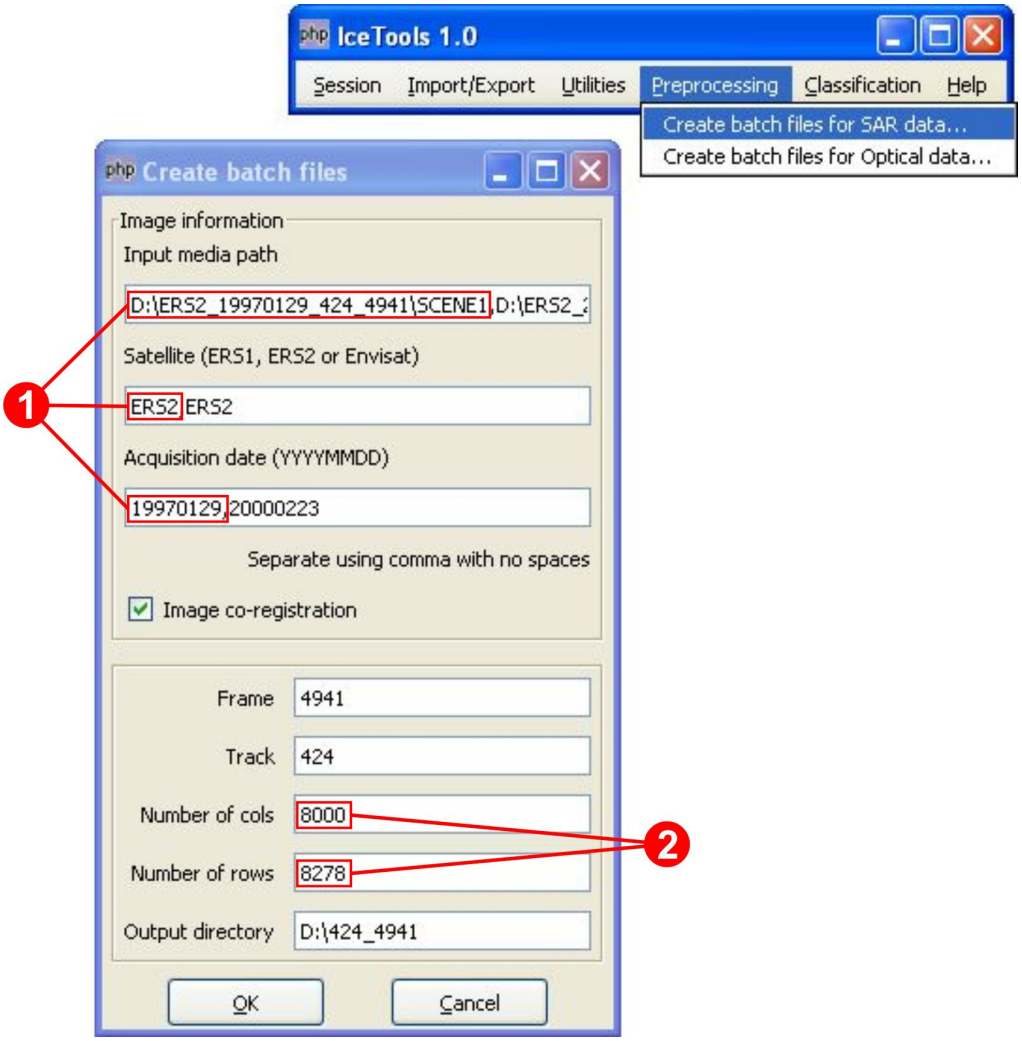

Figure 5.1: *Grafical user interface of the IceTools module for pre-processing of SAR data. (1) indicates the image used as master for co-registering (i.e., the first image in the text entry widget). The number of rows and columns (2) corresponds to the dimensions (in pixels) of this image.*

In the case of ERS-1/2 SAR data, the following additional steps are carried out: (1) correction for variation in the ERS-1 SAR replica pulse power; and (2) correction for saturation in the on-board analogue-to-digital converter (ADC). So, for this kind of data, the following expression is used (Laur et al., 2004):

$$\sigma^{o}_{linear} = \left(\frac{1}{N} \times \sum_{i,j=1}^{i,j=N} DN_{ij}^{2} \right) \times \frac{1}{K} \times \frac{\sin\alpha}{\sin\alpha_{ref}} \times C \times \frac{\mathrm{Pr}\,oduct\,\mathrm{Re}\,plicaPower}{\mathrm{Re}\,ference\,\mathrm{Re}\,plicaPower} \times Powerloss \quad (4)$$

where *C* is the factor that accounts for updating the gain due to the elevation antenna pattern implemented in the processing of ERS SAR data products, *ProductReplicaPower/ReferenceReplicaPower* is the replica pulse power variations correction factor (used for ERS-1 data only), and PowerLoss is the ADC power loss. Finally, the conversion of the sigma nought from linear value to dB is based on the following equation (Rosich and Meadows, 2004):

$$\sigma^{0} = 10 \times \log_{10}\left(\sigma^{0}_{linear}\right) \quad (5)$$

The consistent stability of the ERS-1/2 SAR sensors (Meadows et al., 1998; Laur et al., 2004) and the improved radiometric resolution of Envisat ASAR (ESA, 2006a) enables the direct comparison of calibrated data. Figure 5.2 shows the inter-sensor evaluation of backscatter coefficients from ERS-2 SAR and Envisat ASAR scenes acquired on the same day (Table 5.2). For this comparison, both images were calibrated as described above, and the Envisat ASAR image was subtracted from the ERS-2 SAR. The resulting mean difference (Figure 5.2b) is 1.453 dB, with a standard deviation (SD) of 2.238 dB. Considering that the radiometric resolution of ERS-1/2 SAR and Envisat ASAR sensors are 2.07 and 1.54 dB respectively (ESA, 2006a), the difference found is reasonable. Furthermore, areas with high differences in sigma nought (yellow and red areas in figure 4.3b) correspond to sea (i.e., open water and sea ice), and therefore are subject to changes during the time period between image acquisitions (28 minutes). For analysing areas on glaciers, two test sites (400 x 400 pixels) were chosen on the DSRZ and the FPRZ. In these test areas, the differences are 1.094 dB (SD = 0.826) and 1.469 dB (SD = 1.043) for the DSRZ and the FPRZ respectively.

Table 5.2: *Characteristics of the ERS-2 SAR and Envisat ASAR images used for inter-sensor comparison of backscatter coefficients.*

Platform/Sensor	Acquisition time	Track	Frame	Pass
ERS-2 AMI SAR	15 October 2004 12:47:30	152	4941	Descending
Envisat ASAR	15 October 2004 12:19:03	152	4941	Descending

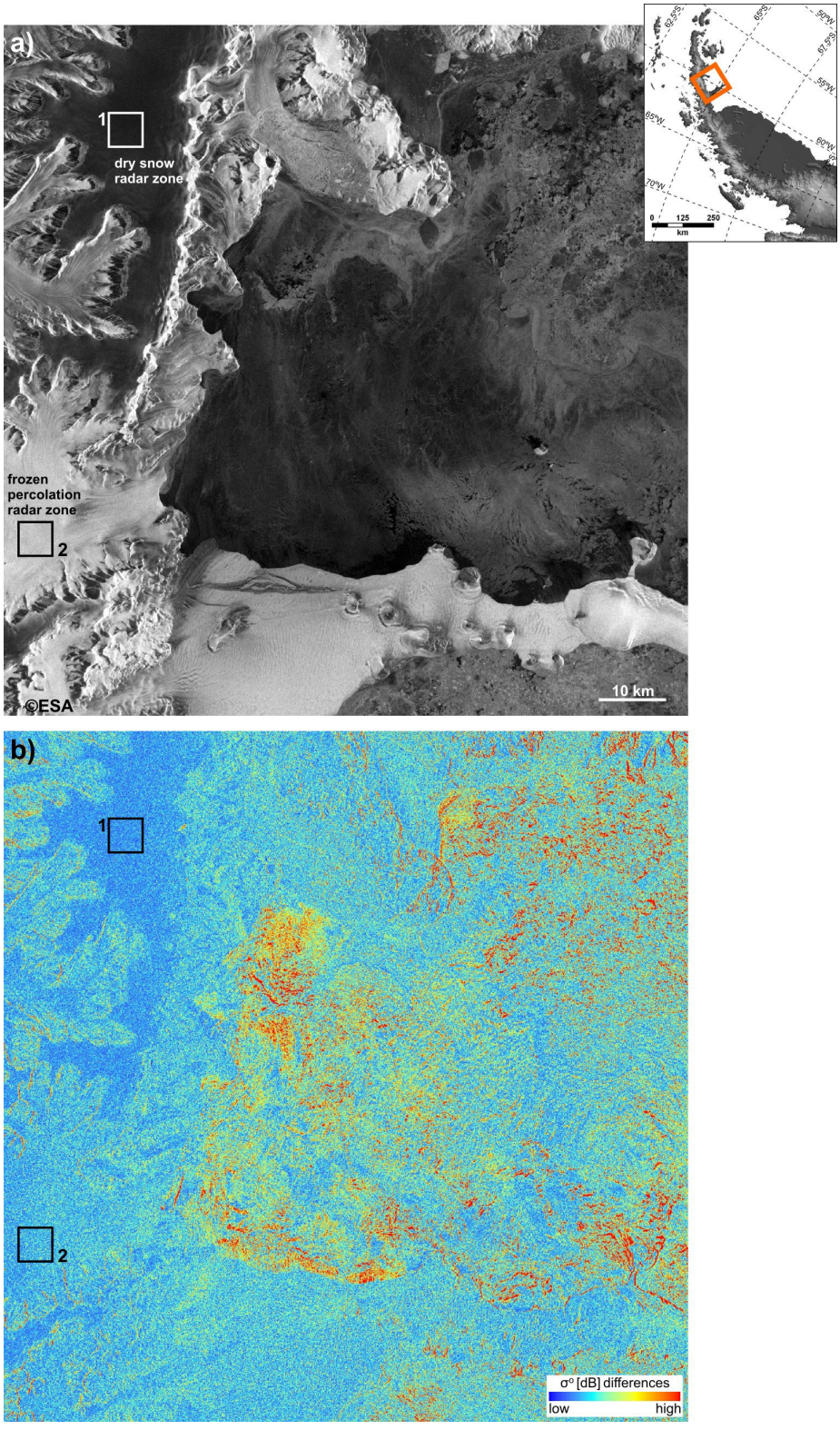

Figure 5.2: *Evaluation of inter-sensor comparability between ERS-2 SAR and Envisat ASAR data acquired on the same day (15 October 2004). a) Envisat ASAR image. b) Difference image (ERS-2 SAR - Envisat ASAR). Hot colours correspond to high differences in values of backscattering coefficient, while cold colours are small variations. The boxes correspond to test areas on the dry snow radar zone (1) and frozen percolation radar zone (2).*

5.3.2 Speckle filtering

Speckle is a characteristic random noise from coherent imaging systems like SAR (Raney, 1998). Therefore, it must be reduced before data can be used for classification. However, the radar image processing programs used to reduce speckle noise also produce changes in the image. The choice of a filter for despeckleling is normally based on characteristics of the targets, subsequent image processing and computational efficiency. In the case of homogeneous areas (e.g., glacier zones), an appropriated speckle filter should preserve the backscattering values, reduce effectively the speckle noise, and preserve edges between the different areas (e.g., at glacier fronts) (Lopes et al., 1990a). Due to the operational orientation of this work, speckle filters chosen for analysis in this chapter are the filters available in BEST (Gamma-MAP) or in Erdas IMAGINE. The speckle filters analysed in this study are:

- Mean filter;
- Median filter (Rees and Satchell, 1997);
- Lee-Sigma filter (Lee, 1983);
- Local Region filter (Nagao and Matsuyama, 1978);
- Lee filter (Lee, 1981);
- Frost filter (Frost et al., 1982); and
- Gamma-MAP filter (Lopes et al., 1990b).

The speckle filters were applied on two ERS-2 SAR image subsets using moving windows with 3 x 3, 5 x 5, and 7 x 7 pixels. The only exception is for the Gamma-MAP algorithm, which can not be applied in BEST with windows smaller than 5 x 5 pixels. To enable the quantitative analysis of filtered images, four homogeneous areas were chosen, two in each subset image (Figures 5.3 and 5.4). These areas consist of 50 x 50 pixels and correspond to the four radar glacier zones as presented in chapter 5.2. Furthermore, the preservation of edges was evaluated by analysing an additional area on a glacier front (Figure 5.4b). There, an AOI was selected on each side of the glacier front (Figure 5.4b). Each AOI corresponds to a

3-pixels wide strip. The test sites were analysed using the following indexes :

- normalised mean (NM);
- coefficient of variation (CV) or speckle index;
- edge gradient; and
- edge noise.

To evaluate the preservation of the mean, the NM (Ndi Nyoungui et al., 2002) was used. NM is the mean backscatter coefficient of an area in each filtered image, normalized to its original mean. The closer to 1 is the NM, the better is the preservation of the mean (Ndi Nyoungui et al., 2002). In homogeneous areas, speckle strength is usually measured with the ratio of the standard deviation to the mean (Lee et al., 1994). It is known as CV or speckle index. For speckle-filtered images, the CV is used to measure the amount of speckle reduction (Lee et al., 1994). The closer to 0 is the value, the better is the speckle reduction. Edge preservation is evaluated by calculating the absolute difference between the mean values of group of pixels in each side of an edge (Lee et al., 1994), known as edge gradient, and the level of speckle noise along both sides of the edge is estimated by the square root of the sum of the two variances (Lee et al., 1994).

A quantitative comparison of the filters is given in tables 5.3 and 5.4. In almost all cases, NM values indicate that all seven filters can preserve the mean in homogeneous areas at an acceptable level (differences in mean values smaller than 5 %). The exception occurs at the frozen percolation radar zone, where only the mean, Lee and Frost filters achieved differences in mean values at the level mentioned above.

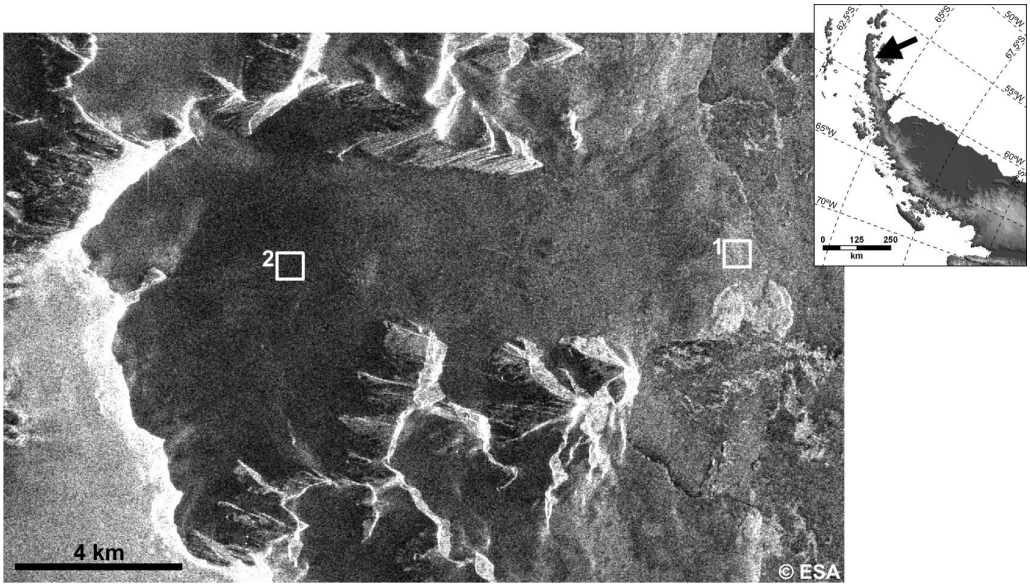

Figure 5.3: *Subset of an ERS-2 SAR image acquired on 26 January 1997 (orbit: 9253, frame: 4923). The white boxes show areas selected for quantitative analysis on bare ice radar zone (1) and wet-snow radar zone (2).*

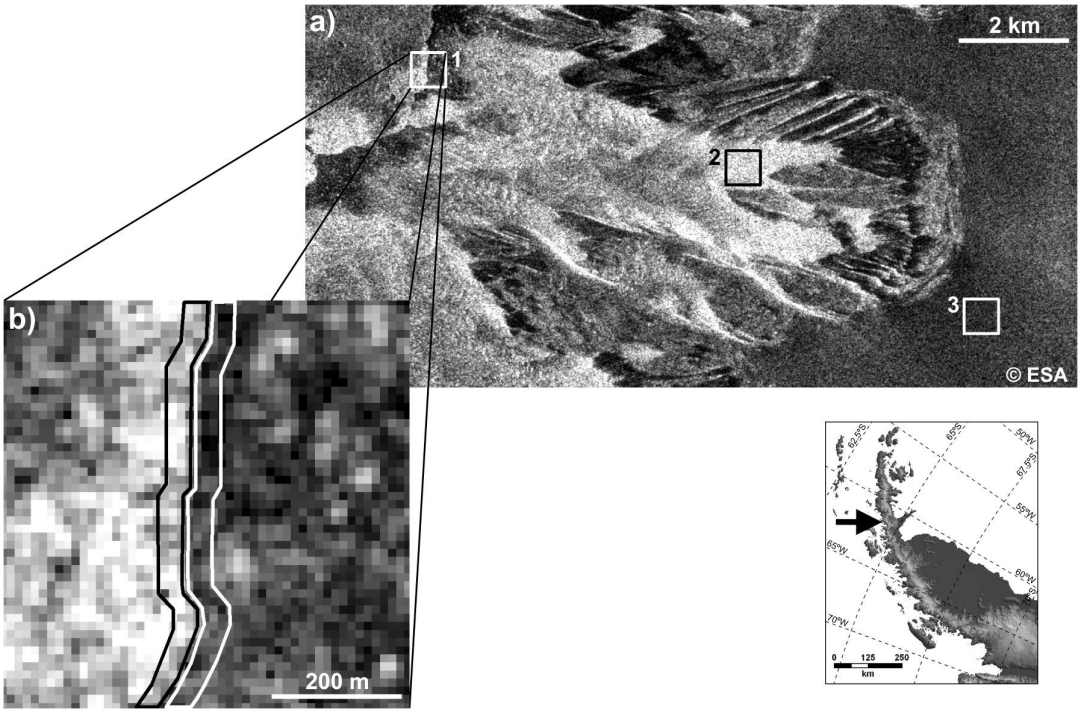

Figure 5.4: *Subset of an ERS-2 SAR image acquired on 16 October 1996 (orbit: 7793, frame: 4941). The three boxes on a) show areas selected for quantitative analysis on the glacier front (1), frozen percolation radar zone (2), and dry snow radar zone (3). The black and white polygons on b) show pixels used for analyses of edge gradient and edge noise.*

Table 5.3: *Comparison of speckle suppression using different filtering algorithms. Based on one pass implementation. NM: normalized mean, CV: coefficient of variation. The closer to 1 is the NM, the better is the preservation of the mean. On the other hand, the closer to 0 is the CV, the better is the speckle reduction. The median 5 x 5 filter yields best overall results.*

Filters	Dry-snow radar zone		Frozen percolation radar zone		Wet-snow radar zone		Bare ice radar zone	
	NM	CV	NM	CV	NM	CV	NM	CV
Original	1.000	-0.170	1.000	-1.182	1.000	-0.135	1.000	-0.297
Mean 3 x 3	1.001	-0.098	1.003	-0.695	1.000	-0.075	1.000	-0.192
Mean 5 x 5	1.001	-0.068	1.002	-0.513	0.999	-0.050	0.999	-0.145
Mean 7 x 7	1.001	-0.055	1.002	-0.428	0.998	-0.038	0.999	-0.123
Median 3 x 3	0.987	-0.105	0.902	-0.809	0.988	-0.079	0.981	-0.203
Median 5 x 5	0.986	-0.071	0.905	-0.587	0.984	-0.052	0.980	-0.152
Median 7 x 7	0.986	-0.057	0.898	-0.485	0.983	-0.040	0.979	-0.127
Lee-Sigma 3 x 3	1.001	-0.098	0.875	-0.864	0.999	-0.075	0.971	-0.222
Lee-Sigma 5 x 5	1.000	-0.114	1.010	-0.773	0.999	-0.050	0.984	-0.165
Lee-Sigma 7 x 7	1.001	-0.055	0.730	-0.811	0.998	-0.038	0.997	-0.129
Local Region 3 x 3	0.984	-0.133	0.884	-1.039	0.987	-0.105	0.977	-0.248
Local Region 5 x 5	0.979	-0.101	0.870	-0.812	0.985	-0.076	0.972	-0.196
Local Region 7 x 7	0.980	-0.082	0.893	-0.654	0.985	-0.061	0.974	-0.161
Lee 3 x 3	1.001	-0.099	0.954	-0.959	1.000	-0.075	0.999	-0.196
Lee 5 x 5	1.001	-0.068	0.984	-0.845	0.999	-0.050	0.999	-0.149
Lee 7 x 7	1.001	-0.055	0.992	-0.800	0.998	-0.038	0.999	-0.127
Frost 3 x 3	1.001	-0.099	0.954	-1.064	0.999	-0.092	0.998	-0.279
Frost 5 x 5	1.001	-0.068	0.987	-0.954	0.999	-0.052	0.996	-0.183
Frost 7 x 7	1.001	-0.055	0.995	-0.856	0.998	-0.038	0.999	-0.128
Gamma-MAP 5 x 5	0.980	-0.105	0.881	-0.878	0.983	-0.085	0.975	-0.212
Gamma-MAP 7 x 7	0.977	-0.095	0.859	-0.850	0.979	-0.073	0.964	-0.202

In terms of speckle suppression, all algorithms yielded positive results. It means that based on analysis of the CV, they effectively reduced the speckle. But generally the mean, median, Lee, and Lee-Sigma filters produced lower values of CV. As expected, CV decreases clearly as the filter window size increase. Nevertheless, due the fact that smoothing is stronger with the increase in window size, it generates loss of information in areas of high-frequency pixels, like edges, lines and points. Finally, the 5 x 5 Gamma-MAP filter performs the best preservation of edges (Table 5.4), followed by the Lee-Sigma filter, but both filters do not reduce the edge noise quite well. Median, Lee, and Frost filters reduce the edge noise, preserving reasonable the edges as well.

The analysis described above shows that median, Lee, and Lee-Sigma filters can be used as effective tools for speckle suppression in SAR images prior to classification of glacier zones. These algorithms not only reduce the speckle, but also preserve the edges between homogeneous areas. However, the better computational efficiency of the median filter (Lee et al., 1994; Ress and Satchell, 1997) confirms it as the most attractive algorithm among these three to be used in a productive processing chain of SAR imagery. Consequently, **the median filter was chosen for speckle reduction**. To effectively reduce the speckle, while at the same time preserving edges, a **window size of 5 x 5** is used.

Table 5.4: *Comparison of preservation of edges in speckle-filtered images using different filtering algorithms. Based on one pass implementation. The closer to the original edge gradient, the better is the preservation of edges. While, the smaller is the edge noise value, the better is the reduction of edge noise.*

Filters	Edge gradient	Edge noise
Original	-10.179	5.293
Mean 3 x 3	-9.083	3.947
Mean 5 x 5	-7.607	3.637
Mean 7 x 7	-6.109	3.233
Median 3 x 3	-9.359	4.016
Median 5 x 5	-8.500	3.523
Median 7 x 7	-7.431	3.220
Lee-Sigma 3 x 3	-9.517	4.077
Lee-Sigma 5 x 5	-9.490	4.163
Lee-Sigma 7 x 7	-7.654	3.728
Local Region 3 x 3	-8.951	5.057
Local Region 5 x 5	-7.279	5.106
Local Region 7 x 7	-5.555	5.170
Lee 3 x 3	-9.436	4.171
Lee 5 x 5	-8.410	3.806
Lee 7 x 7	-7.410	3.457
Frost 3 x 3	-9.565	4.284
Frost 5 x 5	-8.663	3.937
Frost 7 x 7	-7.693	3.616
Gamma-MAP 5 x 5	-10.051	4.739
Gamma-MAP 7 x 7	-4.703	5.742

5.3.3 Geometric correction

The geometric correction of SAR scenes involves geometric operations that make the data usable in conjunction with other geospatial data (e.g., optical imagery, GIS data). First, images from the same track and frame are co-registered. It is done automatically with BEST after the input of data in the IceTools module for pre-processing of SAR imagery (see figure 5.1 and chapter 5.3). The co-

registration of images acquired with the same geometry minimises the requirement of different sets of GCPs for orthorectifying each scene. The last step of the pre-processing of SAR imagery is the orthorectification. For the first image processed in a series of data from the same track and frame, it requires the analyst interaction for selection of suitable GCPs.

The **co-registration** process exactly superimposes one or a set of slave images with respect to a master image. It is performed as follows (ESA, 2005):

(1) an initial registration step is performed using the satellite orbit parameters;

(2) a series of 40 x 40 GCPs is automatically generated on the master image;

(3) using a cross-correlation procedure, GCPs are searched in the slave image. For each GCP on the master image, the search area is restricted to a small image subset (51 x 51 pixels) centred on its corresponding location on the slave image;

(4) a function is computed using a least squares method, which maps the GCPs in the slave image onto the GCPs in the master image; and

(5) finally, a first order polynomial transformation is used to perform the co-registration. Here, only GCPs with small residuals (smaller than 1 pixel) are used. Cubic convolution interpolation is used for image resampling. The common portion of the slave images to be processed corresponds to pixels present in the master image (Figure 5.5).

The **orthorectification** (also called terrain correction) converts the images from sensor to map coordinates and minimises the height introduced distortions that are prevalent in radar images. Here, the GIA Landsat TM mosaic (Chapter 2.3.1) is used as geospatial reference data and the RAMP DEM (Chapter 2.3.2) is the topographic information. This step is done interactively with Erdas IMAGINE and is executed as described below:

(1) using the Generic SAR Node Tool, SAR metadata (e.g., acquisition geometry, orbit parameters, ephemeris) is transferred from an automatically imported image to the pre-processed data. Metadata from the master image is copied to slave images (Steiner, 2002);

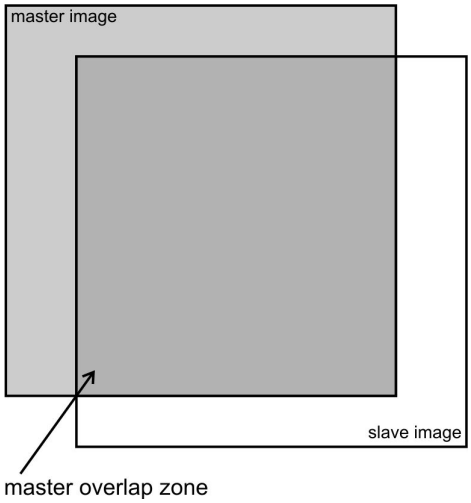

Figure 5.5: *Schematic representation of the portion of slave images used for co-registration (i.e., the master overlap zone).*

(2) with GIA Landsat TM mosaic as reference, GCPs are selected. According to Steiner (2002), 3-5 GCPs are enough to correct for positioning errors of the original satellite orbit parameters. The author found that the further increase in number of GCPs do not necessarily improve the positioning accuracy. By using 5 GCPs, the resulting overall root mean square errors (RMSE) are between 2 and 5 pixels (i.e., 25 to 62.5 m); and

(3) images are resampled using cubic convolution interpolation. This resampling algorithm is used to minimise the small correlation among the neighbour pixels in SAR images (Lee et al., 1994). The spatial resolution of the output data is maintained 12.5 m.

Steiner (2002) shows the occurring errors by using the RAMP DEM with 200 m of spatial resolution and 100 m of vertical accuracy (see chapter 2.3.2 for more details) for orthorectifying ERS-1/2 SAR data. The author demonstrated that at ERS mid range, smooth slopes of less than 20 degrees result in positional errors smaller than ± 313 m (representing about 1.56 pixels of the RAMP DEM). At the AP, these areas correspond to almost the whole region, while regions with slopes of more than 20 degrees are restricted to the stepped transition between the plateau and glacier valleys (Figure 5.6).

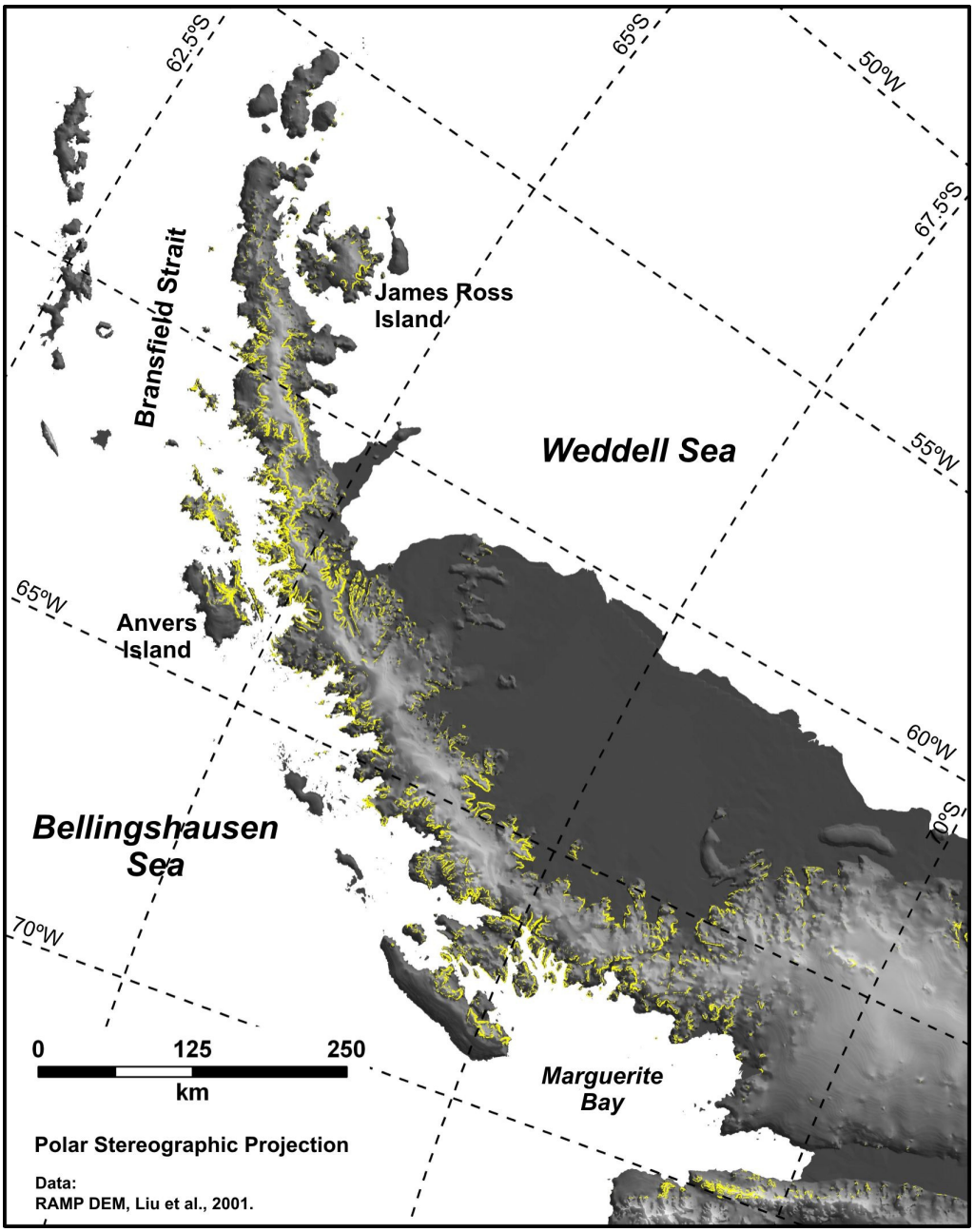

Figure 5.6: *Map of the Antarctic Peninsula showing in yellow areas with slopes of more than 20 degrees. Note that these areas are almost restricted to the transition between the plateau and glacier valleys.*

5.4 Classification of glacier frontal position

For classification of glacier frontal position, two approaches were developed:

- the texture analysis method; and
- the ISODATA method.

The texture method is based on the fact that ice cliffs towards radar sensor generate high backscatter values, while ice cliffs towards opposite directions generate small shadow effects. Therefore, in small segmented images centred on glacier fronts (1000 x 600 m; see chapter 4.3 and figure 5.7), the highest variance values found for a group of pixels should correspond to these features. In this approach, texture images are generated by calculating the variance inside a 9 x 9 moving window and attributing to the central pixel. The maximum variance along the centerline is the glacier front (Figure 5.7). The window size was defined as a compromise between positional accuracy (small windows) and suppression of features like crevasses (large windows). The ISODATA method has its name from the Iterative Self-Organizing Data Analysis Technique (ISODATA) (Lillesand and Kiefer, 2000). Here, this clustering algorithm is used to classify the glacier front images in two classes: *glacier*; and *others* (i.e., sea or sea ice), and the limit between the two classes is considered to be the glacier front (Figure 5.7).

Both methods described above were tested on glaciers selected in chapter 3.5. Summer and winter images were selected from the IPG image database. It resulted in 12 images acquired in summer and 14 in winter (see Appendix, Table A.1), covering 39 and 38 glaciers respectively. The texture approach classified accurately 84.42% of the glaciers (Table 5.5), while ISODATA succeed in 72.73% of the cases.

Table 5.5: *Summary of classification results from the texture and ISODATA approaches used to detect glacier frontal position. The texture method yields best results.*

	Texture				ISODATA			
	Succeed	**Fail**	**Total**	**Classification accuracy (%)**	**Succeed**	**Fail**	**Total**	**Classification accuracy (%)**
Summer	35	4	39	89.74	31	8	39	79.49
Winter	30	18	38	78.95	25	13	38	65.79
Total	65	12	77	84.42	56	21	77	72.73

In order to reduce the time required for analyst-assisted validation of results, both approaches were implemented in the routine for detecting glacier frontal positions. The texture method classifies the glacier fronts, and the ISODATA approach automatically validates the classification results. The computer routine is executed automatically after the generation of glacier front and centerline images (chapter 4.3):

(1) the SAR glacier front images are processed with the texture (variance, 9 x 9 moving window) and the ISODATA (2 classes) algorithms described above;

(2) after that, the pixel values of the texture image are extracted to points along glacier centerlines;

(3) clusters smaller than 500 pixels are eliminated from the classified image (ISODATA), and the resulting classes are also extracted to points;

(4) the point with the highest value of variance and the point at the limit between the two classes are defined as glacier frontal positions respectively for the texture and ISODATA approaches (Figure 5.7);

The last procedures for automatic validation of the classified glacier fronts are done as described in chapter 4.5. Figure 5.7 illustrates the whole process as executed by IceTools.

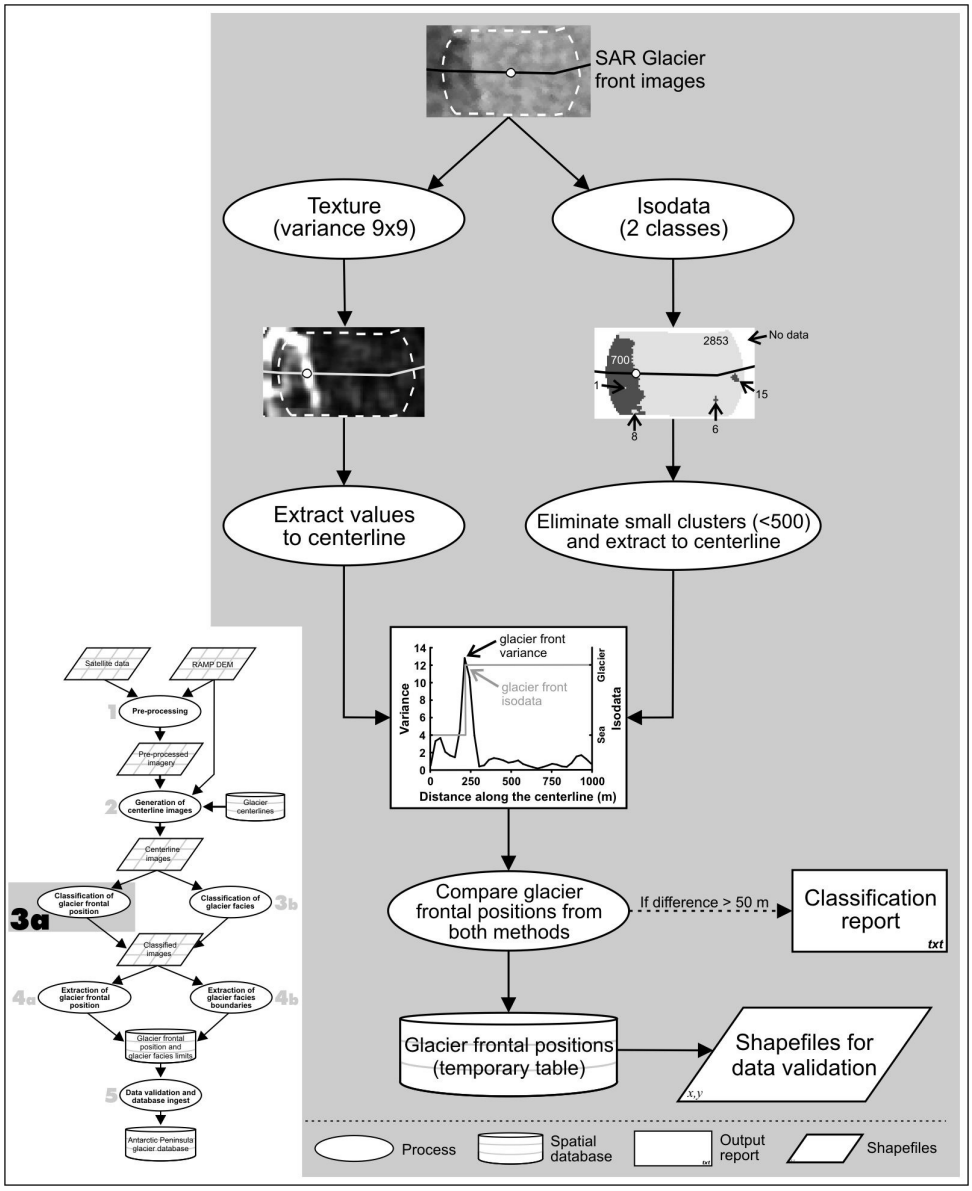

Figure 5.7: *Diagram illustrating the complete processing steps for classification of glacier front by using the texture analysis and ISODATA-based approaches.*

5.5 Classification of radar glacier zones

By using the backscattering characteristics of snow and ice surfaces (see chapter 5.1) and existing knowledge of the regional distribution of glacier facies on the AP, a knowledge-based algorithm was developed for classifying radar glacier zones on the AP (Figure 5.8). It was implemented using the Erdas IMAGINE Spatial Modeler Language (SML).

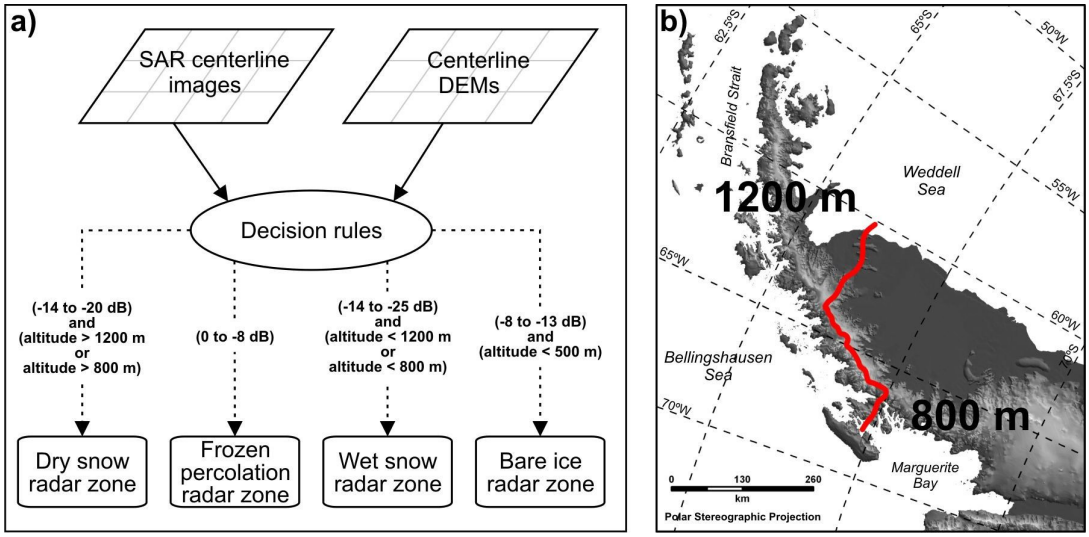

Figure 5.8: *a) Schematic representation of the knowledge-based algorithm developed for classifying radar glacier zones on the Antarctic Peninsula using SAR imagery. b) Map of the Antarctic Peninsula showing the limit (red line) between areas with different thresholds in altitude used to distinguish automatically the dry snow radar zone from the wet snow radar zone.*

Rules for pixel classification (Figure 5.8) were built based on backscattering thresholds determined by Rau et al. (2001), and information found in the literature about the altitudinal distribution of glacier facies on the AP (Simões et al., 1999; Braun et al., 2000; Rau et al., 2001; Rau and Braun, 2002; Skvarca et al., 2004). Using a snow backscatter model at C-band, Rau et al. (2001) validated the empirically derived thresholds in σ^0 used for classifying radar glacier zones on the AP. The difference in dry snow line altitude between the north and the south parts of the peninsula (Rau and Braun, 2002; Rau, 2003), is represented by different thresholds in altitude for this areas (Figure 5.8b). It is used to distinguish automatically the DSRZ from the WSRZ. As the limits of zones on glaciers is greatly influenced by local topographic and meteorological settings (Williams et al., 1991; Ramage and Isacks, 1998), it is expected that some glaciers could need particular information. Therefore, thresholds in altitude were stored for each glacier analysed here (240 at total) in the table *sar_thresholds* of the AntPenDB. If different thresholds are needed for determined glaciers, *sar_thresholds* is updated with the new values.

Using the developed knowledge-based algorithm as core part, a routine for extraction of boundaries between radar glacier zones from segmented SAR data

was built. It is executed automatically after the classification of glacier frontal positions. The workflow is described below and illustrated in figure 5.9:

(1) IceTools queries the AntPenDB and recovers the thresholds in altitude for glaciers in analysis;

(2) then, this program executes the classification of SAR centerline images using the knowledge-based classifier (Figure 5.8). Centerline DEMs are used as source of topographic information; and

(3) after the classification, small patches of less than 2000 pixels are eliminated. It removes high-frequency spatial variance (noise) from classified images, generating more continuous and coherent classes.

Classified imagettes are resulting from the processing steps presented above. Afterwards, they are processed according to the general procedures described in chapter 4.5. Figure 5.9 exemplifies the complete routine developed for classifying and extracting the glacier zonal boundaries.

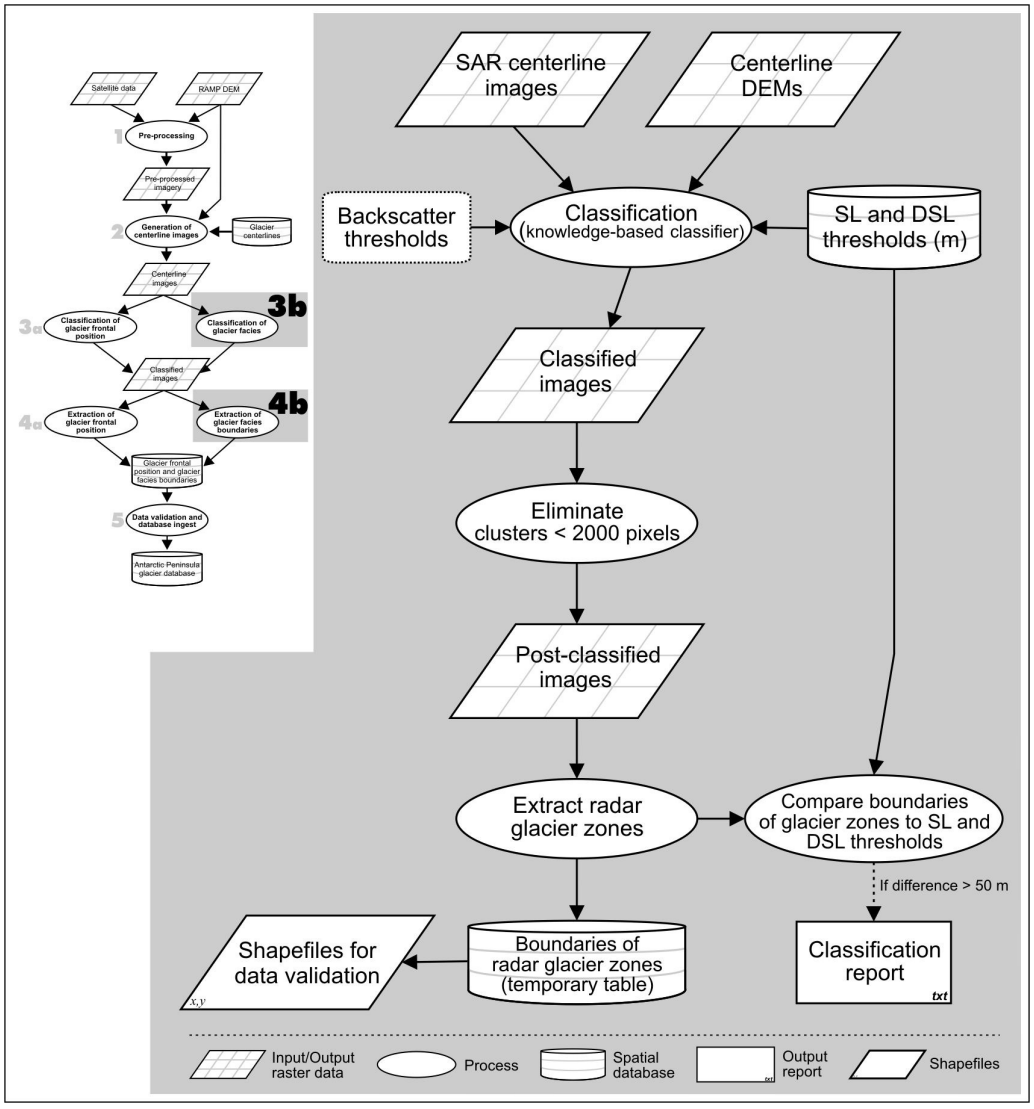

Figure 5.9: *Diagram illustrating the processing steps for extraction of boundaries between radar glacier zones from segmented SAR data.*

6 Classification of glaciers surfaces using optical data

Optical data is available for the Antarctic Peninsula (AP) since 1972, making possible a 34-years record of changes in glacier parameters (chapter 2.2.2). The processing chain described in chapter 4 enables the semi-automatic analysis of these satellite datasets. This chapter presents the glacier zones as detected by optical sensors, and describes specific procedures used in the processing of this kind of data.

6.1 Characteristics of snow and ice reflectance

In the visible (VIS) region of the electromagnetic spectrum, freshly-fallen snow has high values of reflectance (Figure 6.1 and Table 6.1). As snow begins to metamorphose, a reduction of effective volume scattering occurs (Wiscombe and Warren, 1980), slightly decreasing reflectance values (Hall et al., 1988). However, for snow grain sizes between 50 and 1000 µm, the reflectance differences in the VIS do not exceed 0.10-0.15 (Wiscombe and Warren, 1980). Because the low absorption coefficient of ice at these wavelengths (Dozier and Painter, 2004), when a snow grain increases, the probability of a photon passing through that snow grain will be absorbed does not increase much (Dozier, 1989a). Nevertheless, the presence of small impurities in concentration of only 1 part per million by weight can lower snow reflectance between 0.05 and 0.15 in the VIS

(Warren and Wiscombe, 1980).

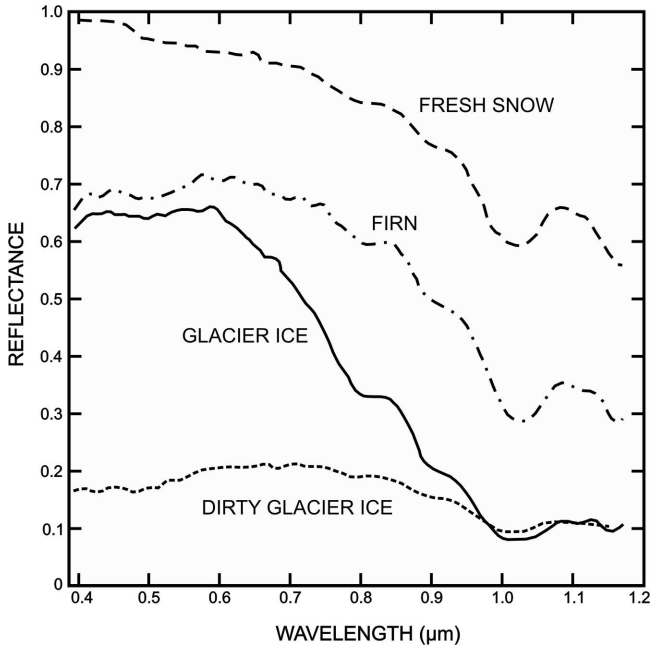

Figure 6.1: *Spectral reflectance curves of fresh snow, firn and ice. After Zeng et al. (1984).*

At near-infrared (NIR) wavelengths ice is slightly absorptive (Dozier, 1989a), and the snow reflectance depends mostly on the size of snow grains (Wiscombe and Warren, 1980). There, values of snow reflectance may fall by a factor of 2 or more for snow-grain sizes between 50 and 1000 μm (Wiscombe and Warren, 1980). As snow melts, clusters of snow grains form in unsaturated wet snow, behaving optically as single grains (Dozier and Painter, 2004). It explains the decrease of reflectance at NIR, as snow melting occurs. The largest sensitivity of snow reflectance to grain size occurs in wavelengths from 1.0 to 1.3 μm (Dozier, 1989b), being larger when atmospheric effects and snow contamination are small (Fily et al., 1997).

At VIS and NIR, snow reflectance is similar to cloud reflectance. It is due to similar refractive indices of ice and water in this region of the electromagnetic spectrum (Winther and Hall, 1999; Green et al., 2002). In the middle-infrared (MIR) region (around 1.65 μm), ice is more absorptive than water, excepting for very small ice crystals (between 1 and 20 μm) as present in ice clouds (Dozier and Marks, 1987). Thus, MIR reflectance of clouds remain very high while values of snow reflectance

fall to near zero (Hall et al., 1988).

Table 6.1: *Overview on snow and ice reflectance as reported from different datasets and study sites.*

Optical glacier zones	Reflectance Green	Reflectance Red	Reflectance Near-infrared	Reflectance Middle-infrared	Sensor	Study area	Author
Dry snow optical zone	b	b	0.73±0.01	0.02±0.00	Landsat TM	Austria	Hall et al. (1988)
	0.85±0.15	0.89±0.13	0.94±0.18	0.05±0.01	Landsat TM	Alaska	Hall et al. (1988)
	0.924	0.922	0.85	0.43	Radiometer	Victoria Land, Antarctica	Zibordi and Maracci (1993)
	a	0.90	0.85	0.07	Radiometer	Vestfold Hills, Antarctica	Boresjö-Bronge and Bronge (1999)
	0.96[d]	a	0.90[d]	a	Pyranometer	Switzerland	Knap et al. (1999)
	a	a	0.86	0.0918	AVIRIS	Arctic	Li et al. (2001)
	0.92-0.94	0.91-0.92	0.84-0.87	0.085-0.16	Radiometer	Terra Nova Bay, Antarctica	Casacchia et al. (2002)
Wet snow optical zone	0.62±0.06	0.52±0.02	0.62±0.07	0.03±0.01	Landsat TM	Austria	Hall et al. (1988)
	0.72±0.05	0.61±0.01	0.63±0.06	0.01±0.00	Landsat TM	Alaska	Hall et al. (1988)
	a	0.81-0.88	0.64-0.67	0.02	Radiometer	Vestfold Hills, Antarctica[c]	Boresjö-Bronge and Bronge (1999)
	a	0.89-0.97	0.67-0.77	0.03-0.06	Radiometer	Vestfold Hills, Antarctica	Boresjö-Bronge and Bronge (1999)
Bare ice optical zone	0.45±0.05	0.44±0.04	0.35±0.02	0.02±0.00	Landsat TM	Alaska	Hall et al. (1988)
	a	0.65-0.77	0.29-0.37	0.02-0.03	Radiometer	Vestfold Hills, Antarctica	Boresjö-Bronge and Bronge (1999)
	0.53-0.66[d]	a	0.44-0.55[d]	a	Pyranometer	Switzerland	Knap et al. (1999)
Bare ice with debris	0.24±0.02	0.23±0.02	0.20±0.02	0.01±0.00	Landsat TM	Austria	Hall et al. (1988)

[a] *No measurement.*
[b] *Data saturation occurred.*
[c] *Highly-metamorphosed snow.*
[d] *Data derived from figures in the respective publications.*

Snow and ice are anisotropic reflectors (Wiscombe and Warren, 1980; Knap and Reijmer, 1998). It means that the upward flux of energy on glaciers is not the same in all directions (Hall et al., 1988). The effects of the snow and ice anisotropy is stronger at NIR wavelengths (Dozier, 1989a; Knap and Reijmer, 1998), resulting in a peak of reflectance in the forward direction (Dozier and Painter, 2004). The higher absorption in NIR than in the VIS explains the higher anisotropy occurring there (Knap and Reijmer, 1998). Photons with longer wavelengths penetrate less deeply into the snow than those with shorter wavelengths (Li et al., 2001), resulting in fewer scattering events at the longer wavelengths (Knap and Reijmer, 1998). This effect is further enhanced by increase in single particle forward scattering with increasing wavelength (Knap and Reijmer, 1998). Furthermore, as grain size or illumination angle increases, the specular component of forward scattering increases as well (Dozier, 1989a; Hall et al., 1992). However, Painter and Dozier (2004) showed that the variability in the hemispherical-directional reflectance factor (HDRF) is negligible for near-nadir sensors.

6.2 Glacier zones as detected by optical sensors

Visible and infrared imagery enables the classification of different zones on glaciers (Hall et al., 1987; Hall et al., 1988; Williams et al., 1991; Boresjö-Bronge and Bronge, 1999; Sidjak and Wheate, 1999; König et al., 2001; Heiskanen et al., 2003), which are usually divided in three main classes (Hall et al., 1987; Hall et al., 1988; Sidjak and Wheate, 1999; Heiskanen et al., 2003):

(1) dry snow optical zone (DSOZ);

(2) wet snow optical zone (WSOZ); and

(3) bare ice optical zone (BIOZ).

In order to point out the contrast to classical glacier facies (chapter 2.1) and radar glacier zones (see chapter 5.2), glacial zoning as detected by optical sensors are denominated optical glacier zones in this study.

Responding to weather conditions, the boundaries of the optical glacier zones

change during the year (König et al., 2001). Furthermore, a new snowfall can hide the boundaries between the optical glacier zones. Therefore, these zones do not correspond to the classical glacier facies as described by Paterson (1994). Due to optical properties of ice crystals, the radiance measured on glaciers at VIS and IR wavelengths depends on properties of a few centimetres (10-20 cm) of the snowpack (Wiscombe and Warren, 1980). Thus, optical glacier zones are determined by superficial properties of glaciers, while the classical glacier facies depend on properties of the entire snowpack from the last accumulation season (Paterson, 1994). Nevertheless, the position of the limits between optical glacier zones (i.e., snow line and transient wet snow line) is considered a proxy for information on glacier mass balance and present or recent meteorological conditions (Williams et al., 1991).

6.2.1 Dry snow optical zone

The DSOZ corresponds to the area of the glacier which is covered by freshly-fallen or slightly metamorphosed snow at the instant of image acquisition. Due to the effective volume scattering occurring in the first centimeters of the snowpack (Wiscombe and Warren, 1980), it is characterized by high reflectance values at VIS and NIR wavelengths. The high absorption coefficient of ice at MIR (Dozier, 1989a) explains the low values of reflectance occurring there. The **dry snow line** depends on measurements which extend below the surface to show the presence or absence of slight wetting in the snowpack (Williams et al., 1991). So, it **can not be detected by optical sensors**.

6.2.2 Wet snow optical zone

This zone includes firn, slush, and snow highly metamorphosed by melting and refreezing cycles (Hall et al., 1988). Here, liquid water reduces the snow reflectance only by increasing the effective grain size (Wiscombe and Warren, 1980), which remains optically with the same size after refrozen. Thus, the development of a WSOZ could correspond to a early state of the snowpack. But

anyway it indicates the area which was highly affected by wet-snow metamorphism. The slush area corresponds to snow completely saturated with water, localized at the inferior portion of the wet snow zone (Williams et al., 1991). The wet snow line, although apparently discernible at the surface, depends on wetting of the entire snowpack deposited during the previous winter (Paterson, 1994). Because the snow reflectance depends on the 10-20 cm of the snowpack (Wiscombe and Warren, 1980), the transient wet snow line located on optical images does not correspond to that defined by Paterson (1994) (Williams et al., 1991).

6.2.3 Bare ice optical zone

The BIOZ corresponds to both ice zones described by Paterson (1994): the bare glacier ice of the ablation area; and the superimposed ice (Figure 2.1). Furthermore, some small patches of firn, wet snow, or debris-covered ice can occur at this zone (Hall et al., 1988). Reflectance on the bare ice zone is slightly lower than the wet-snow reflectance at the VIS, but it is reduced to quite low values at NIR (see figure 6.1 and table 6.1), contrasting well with the reflectance on the wet and dry snow zones. The upper limit of the bare ice zone corresponds to the snow or firn line.

6.3 Pre-processing of optical data

This chapter describes the steps necessary to prepare optical imagery for classification. Basically, it includes:

(1) geometric correction; and

(2) radiometric calibration.

The geometric correction consists of co-registering the scenes to a common spatial reference, requiring the interactive selection of GCPs. However, for data acquired on the same location (path and row), this step is done only for the first image to be processed, and the defined geometric correction model is used for

subsequent imagery. The radiometric calibration converts the data to a common radiometric scale. Using IceTools, it can be done for one or a series of images. Figure 6.2 shows the GUI used for input of image information used for writing of batch files and executing automatically the process.

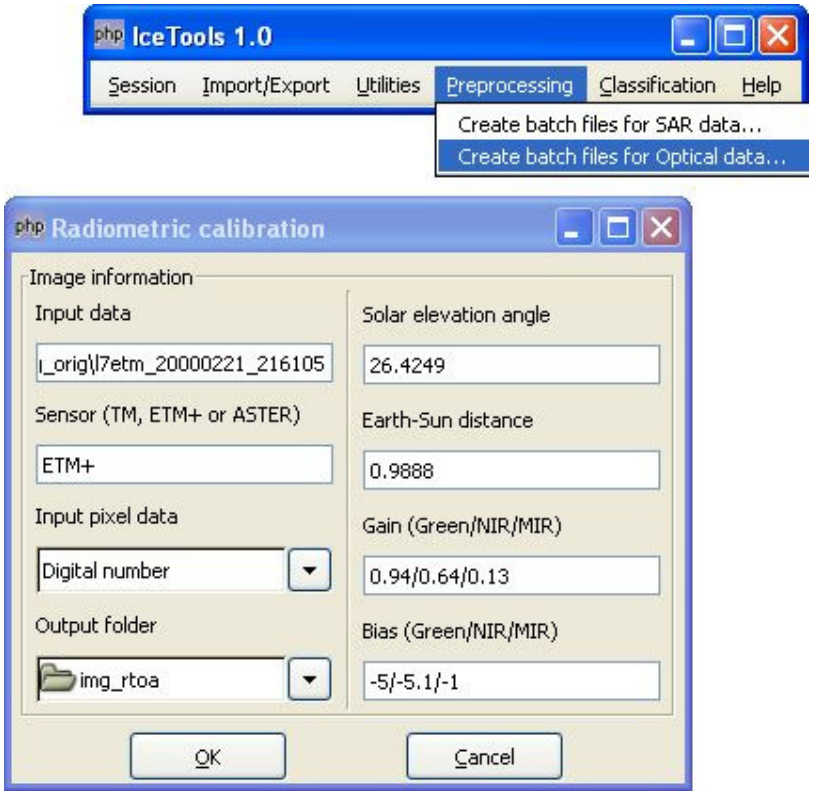

Figure 6.2: *Grafical user interface of the IceTools module for pre-processing of optical data. It enables the input of image information used to prepare batch files and execute the radiometric calibration on a series of scenes.*

6.3.1 Geometric correction

In this step, optical imagery is co-registered to the GIA Landsat TM mosaic (Chapter 2.3.1). Using Erdas IMAGINE, this task is done interactively in the following sequence:

(1) with the GIA Landsat TM mosaic as spatial reference, 25 or 15 GCPs are selected for co-registering TM/ETM+ or ASTER images respectively. As

scenes acquired on a particular path and row can be co-registered using the same set of GCPs, they are selected only for the first image to be processed;

(2) using a second-order polynomial transformation, the new position of each pixel is calculated. RMSE smaller than 30 m are achieved by this process. Whenever higher values of RMSE are found, the location of GCPs has to be improved; and

(3) finally, the images are resampled using the nearest neighbour algorithm. Spatial resolution of output data is maintained in 30 (TM/ETM+) and 15 m (ASTER).

The transformation of pixel row and column numbers to map projections without considering elevation produces shift in pixel positions (Figure 6.3). It is directly depending on terrain elevation and nadir distance. However, this effects will not affect strongly glacier parameters derived from optical data (i.e., glacier frontal position, snow line, and transient wet snow line). The snow line on the AP is found below 500 m altitude (Simões et al., 1999; Braun et al., 2000; Rau et al., 2001; Skvarca et al., 2004), while the transient wet snow line seldom reaches 1200 m (Rau et al., 2001; Rau and Braun, 2002). Furthermore, since the swath width of ASTER is 60 km, positional errors due to terrain effects on this kind of images are smaller than 60 m (Figure 6.3).

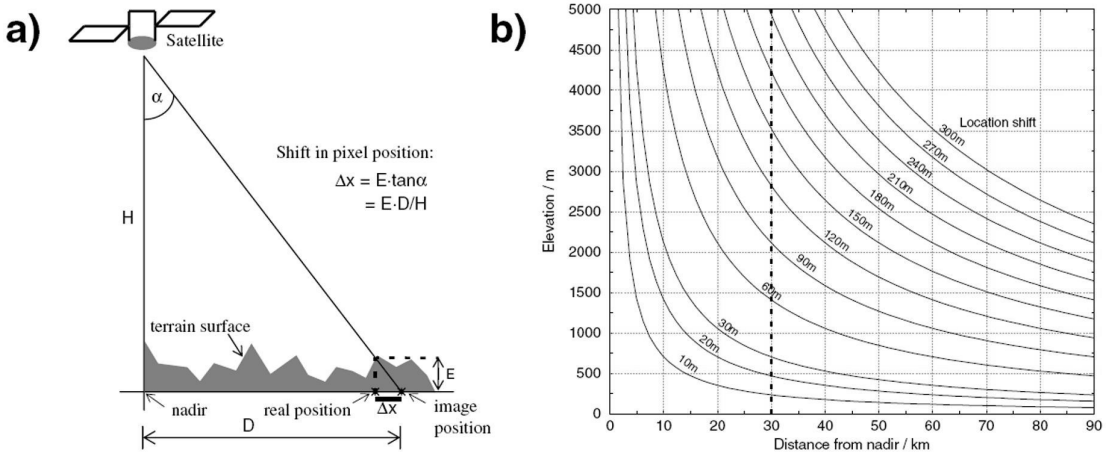

Figure 6.3: *a) Schematic representation of the shift in pixel location by transforming of pixel row and column numbers to a map projection without considering elevation. b) Shift of pixel location as a function of terrain elevation and nadir distance for Landsat TM/ETM+ and Terra ASTER data. The dashed line on b represents the maximum distance from nadir for Terra ASTER imagery. Modified after Paul (2003).*

6.3.2 Radiometric calibration

Spectral information detected by sensors in the VIS and IR regions of the electromagnetic spectrum is recorded as digital number (DN) values. It means, the ground reflectance measured in terms of radiance is offset and scaled during the image acquisition. The radiometric calibration consist of converting the DNs to spectral reflectance at satellite level.

The first step is the conversion from DNs to spectral radiance (W m^{-2} sr^{-1} μm^{-1}) detected at the sensor. ASTER data is imported directly to radiance values. The at-sensor radiance (L_{sat}) from TM/ETM+ data is retrieved as (NASA, 2006):

$$L_{sat} = G \times DN + B \tag{6}$$

where B is the offset value for each band and corresponds to minimum spectral radiance detected at sensor (L_{min}), and G is the sensor gain for each band calculated with a relation between maximum (L_{max}) and minimum radiance (L_{min}) for each band and maximum digital number (255 for 8 bits data) as (Chander and Markham, 2003):

$$G = \frac{\left(L_{\max} - L_{\min}\right)}{255} \tag{7}$$

Finally, spectral reflectance at satellite level (ρ_{sat}) is calculated as (NASA, 2006):

$$\rho_{sat} = \frac{\pi \times d^2 \times L_{sat}}{E_0 \times \cos\theta_z} \tag{8}$$

where d is the Earth-Sun distance in astronomical units, E_0 is the exoatmospheric solar spectral irradiance (W m^{-2} μm^{-1}), and θ_z the solar zenith angle. The value of E_0 for each spectral band are based on data from Iqbal (1980). The ρ_{sat} is the directional-hemispheric reflectance of the Earth-atmosphere system if the angular distribution of the reflected radiation is assumed to be isotropic (Dozier 1989b). The use of ρ_{sat} values instead of digital numbers for analysis of snow and ice surfaces facilitates scene-to-scene comparisons of glaciers (Hall et al. 1988), and enables the development of a multi-sensor approach. Furthermore, by calculating ρ_{sat}, effects of the solar zenith angle on the incoming radiation at a plane surface are corrected.

Besides surface properties, two main factors are responsible for affecting the reflectance detected by optical satellite sensors on glaciers: (1) topographic effects; and (2) atmospheric effects. Topographic effects are caused by different illumination conditions on rough terrain and adjacency effects caused by additional illumination from direct and scattered radiation from adjacent slopes (Li et al., 2002). Atmospheric effects are resulting from scattering and absorption of solar radiation by molecules and aerosols through the sun-surface-satellite paths (Vermote et al., 1997). Both need suitable, supplementary information for accurate correction (Sandmeier and Itten, 1997), which is not available for the AP. However, as demonstrated in chapter 3.2.2, the use of the centerline approach eliminate many areas affected by topographic effects. In addition, Hall et al. (1995) and Paul (2001) demonstrated the possibility of using data without atmospheric correction in operational routines for mapping snow-cover extension and glacier surfaces. Here, the main consequence expected is the underestimation of reflectance values (Hall et al., 1990; Winther and Hall, 1999), when compared with atmospherically-corrected data or field measurements.

6.4 Classification of glacier frontal position

The classification of glacier frontal position is performed with methods presented in chapter 5.4 (i.e., texture analysis and ISODATA classification). The developed algorithms consist of adaptive procedures for detecting glacier frontal positions with different conditions of sea ice, brush ice or open water at the front of glaciers. In this chapter, particular details regarding the use of optical imagery are explained.

Among the channels available from visible and infrared sensors used in this study, the NIR is the most sensitive to snow properties (Boresjö-Bronge and Bronge, 1999; see table 6.1). So this channel is used as input for classifying glacier fronts, enabling class separability in situations when snow-covered sea ice is contiguous to glaciers. Here, small differences in reflectance between sea ice and glacier surface, or shadows and peaks of reflectance at the glacier front are enough to allow the detection of glacier frontal position in segmented imagettes (see chapter 4.3 for comprehensive explanation on creating small images for classification).

To generate variance images used in the texture analyses, the size of moving windows is a compromise between positional accuracy (small windows) and suppression of features (large windows). In addition, it depends on pixel size, because the highest the resolution, the more small features like crevasses and ice fractures will be represented in satellite images. The optimal size for moving windows to be used with TM/ETM+ (30 m spatial resolution) and ASTER data (15 m spatial resolution) are 5 x 5 and 9 x 9 pixels respectively.

Both methods were tested on glaciers selected in chapter 3.5. Two sets of images available at the IPG were used for that: 16 Landsat TM (12) or ETM+ images (4); and 36 ASTER scenes (see Appendix, Table A.2). It covered 54 and 46 glaciers respectively. The resulting glacier fronts were evaluated visually, and the classification accuracy is summarised in table 6.2. The texture approach classified accurately 86% of the glacier fronts, while ISODATA succeed in 70% of the cases. Most of the misclassification (57.9%) occurred when sea ice was contiguous to glacier fronts.

Table 6.2: *Summary of classification results from texture and ISODATA approaches used to detect glacier frontal position using Landsat TM/ETM+ and Terra ASTER data. The texture method yields best results.*

	Texture				ISODATA			
	Succeed	**Fail**	**Total**	**Classification accuracy (%)**	**Succeed**	**Fail**	**Total**	**Classification accuracy (%)**
TM/ETM+	50	4	54	92.59	41	13	54	75.93
ASTER	36	10	46	78.26	29	17	46	63.04
Total	86	14	100	86.00	70	30	100	70.00

The computer routine is executed as described in chapter 5.4. The last procedures for automatic validation of the classified glacier fronts are done as explained in chapter 4.5.

6.5 Classification of optical glacier zones

This step uses the maximum likelihood classifier for categorisation of optical glacier zones. This classification algorithm evaluates quantitatively the mean vector and covariance matrix of spectral classes when classifying an unknown

pixel (Lillesand and Kiefer, 2000), taking into account the reflectance variability of optical glacier zones (Table 6.1). Here, four classes are considered: DSOZ; WSOZ; BIOZ; and clouds. As glacier frontal positions are derived from the algorithm described in chapter 6.4, classes located at the sea surface (e.g., water, sea ice, suspended sediments) are not considered for supervised classification, reducing possible sources of classification errors. Shadows on snow surfaces caused by the topography or clouds are frequently misclassified as ice (Boresjö-Bronge and Bronge, 1999; Sidjak and Wheate, 1999). To overcome this problem, pixels classified as bare ice glacier zone above 500 m altitude or with MIR reflectance higher than 0.05 (i.e., near clouds) are reclassified as shadows, given that there is no record of snow line above this altitude at the AP and ice has small values of reflectance at the MIR wavelength (Hall et al., 1988; Boresjö-Bronge and Bronge, 1999).

To describe the spectral response pattern for optical glacier zones, representative training areas were selected from images on both sides of the AP (Table 6.3). Due to the lack of ground truth data to validate classes observed in reference images, information on snow and ice reflectance from the literature (summarised in table 6.1) was used as ancillary information for visual interpretation. Figure 6.4 shows some examples of training samples selected. In total, 81 areas were delineated (Table 6.4).

Table 6.3: *List of reference images used for selection of training samples for maximum likelihood classification.*

Satellite sensor	Path/Row	Acquisition date	Solar elevation angle (°)	Solar azimuth angle (°)	Side of the Antarctic Peninsula
Landsat 4 TM	215/105	1988.02.29	21.98	61.27	East
Landsat 5 TM	220/108	1986.03.06	16.25	62.99	West
Landsat 7 ETM+	216/105	2000.02.21	26.42	56.45	East
Landsat 7 ETM+	218/105	2001.02.21	26.03	57.00	West
Terra ASTER	218/297	2001.01.04	37.84	52.57	West
Terra ASTER	215/289	2002.01.18	38.16	54.33	East
Terra ASTER	215/290	2002.01.18	37.59	54.39	East

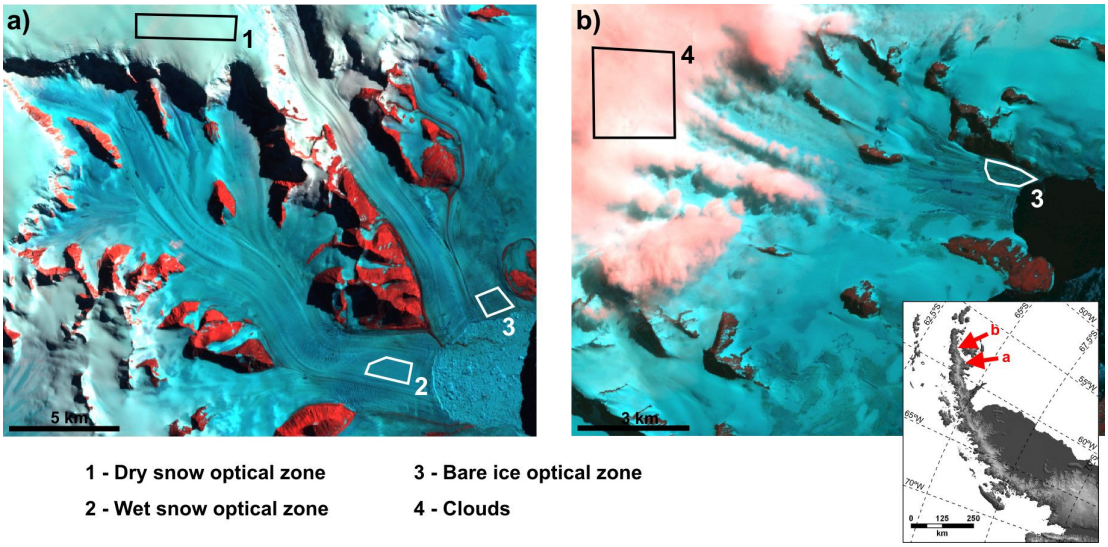

Figure 6.4: *Examples of training samples selected for defining signatures for maximum likelihood classification. The validation of classes interpreted visually was based on table 6.1. a) Subset of a Landsat 7 ETM+ image (path: 216, row: 105) acquired on 21 February 2000. b) Subset of a Terra ASTER image (path: 215, row: 289) acquired on 18 January 2002.*

Table 6.4: *Total number of training samples and pixels selected for spectral analysis.*

Satellite sensor	Classes	Number of training areas	Number of pixels
Landsat TM	Dry snow optical zone	10	55133
	Wet snow optical zone	5	5541
	Bare ice optical zone	6	1694
	Clouds	2	32386
Landsat ETM+	Dry snow optical zone	10	57410
	Wet snow optical zone	12	15368
	Bare ice optical zone	8	2312
	Clouds	2	10729
Terra ASTER	Dry snow optical zone	8	187428
	Wet snow optical zone	6	16920
	Bare ice optical zone	8	10224
	Clouds	4	59675

TM/ETM+ band 1 was not considered for classification because of pixel saturation on glacier surfaces (Dozier, 1989a; Heiskanen et al., 2003). Furthermore, due to the fact that values of snow reflectance fall to near zero at SWIR (Hall et al., 1988), only the middle infrared channel was used in the classification (i.e., bands 5 and 4 from TM/ETM+ and ASTER respectively).

As required for multispectral classification, statistics derived from training samples (Figure 6.5) show good separability of classes in the spectral space. As described by some authors (Hall et al., 1990; Winther and Hall, 1999; Dozier and Painter, 2004), the reflectance at satellite level resulted in smaller values than that derived from field measurements (Figure 6.5). However, the same spectral pattern is observed. The differences in reflectance are interpreted as a product from several factors like as: different surface characteristics; different sensors; and general attenuation by atmospheric effects (Winther and Hall, 1999). Furthermore, variations among reflectance values measured for each optical glacier zone by different sensors are also found in the literature (Table 6.1).

The spectral signatures were tested on glaciers selected in chapter 3.5. Although different training samples are used for classification of TM and ETM+ data, they were selected as complementary datasets, covering together 54 test glaciers. ASTER data available at the IPG covered 46 glaciers. In total, glacier centerline images from 16 Landsat TM/ETM+ images (12 and 4 from each instrument respectively) and 36 ASTER scenes were used for evaluating the classification. Trials were performed with the following band combinations:

(1) green, red, NIR, and MIR; and

(2) red, NIR, and MIR.

Due to similar spectral behaviour of the all classes in the green and red channels (Figure 6.5), the second trial considered only one of them. In that case, the red band was chosen instead of the green because of the saturation occurring frequently on snow surfaces in the last one (Hall et al., 1988).

According to Sidjak and Wheate (1999) and Heiskanen et al. (2003), visual interpretation is the most accurate way to delineate glacier zones using optical imagery. These authors suggest that this is the only way to take topography and glacier features like crevassed fields into account. Nevertheless, a rigorous evaluation of the visually interpreted snow line and transient wet snow line is not possible without ground truth data.

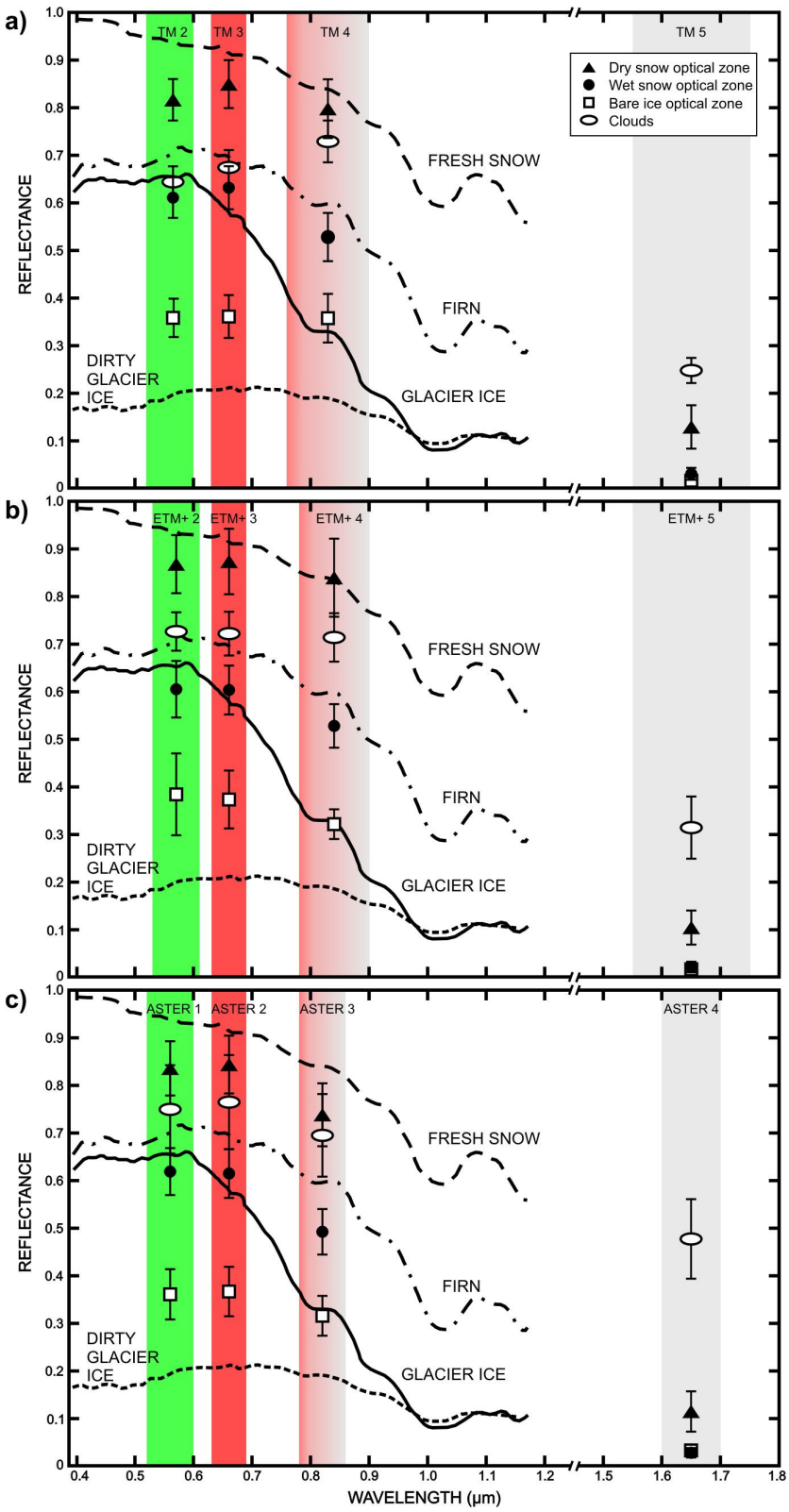

Figure 6.5: *Mean values of at-satellite reflectance from training areas selected from TM (a), ETM+ (b), and ASTER (c) images. Bars indicate one standard deviation. Spectral reflectance curves of fresh snow, firn and ice after Zeng et al. (1984).*

In order to evaluate both combination of bands, classification results were compared against visual interpretation. Results of accuracy assessment are presented in table 6.5. The first trial classified accurately 80% of the glacier surfaces, while the second succeed in 91% of the cases. The use of the green band as input for classification increases the number of cloud pixels being classified as snow, and reduces the ability for discriminating clouds from snow and firn. As observed in early studies (Sidjak and Wheate, 1999), highly fractured ice in crevassed fields and ice falls were sometimes mapped as wet snow optical zone.

Table 6.5: *Summary of classification results from trials used for testing two sets of band combinations for maximum likelihood classification of Landsat TM/ETM+ and Terra ASTER glacier centerline images. The use of red, NIR and MIR yields best results.*

Bands	**Green, Red, NIR and MIR**				**Red, NIR and MIR**			
	Succeed	**Fail**	**Total**	**Classification Accuracy (%)**	**Succeed**	**Fail**	**Total**	**Classification Accuracy (%)**
TM/ETM+	45	9	54	83.33	48	6	54	88.88
ASTER	35	11	46	76.09	43	3	46	93.48
Total	80	20	100	80	91	9	100	91

Due to more accurate results, band combinations used in the second trial (i.e., red, NIR, and MIR) are selected to be used in an operational routine for classification of optical glacier zones along glacier centerlines. The whole classification and post-classification processes were implemented using functions available in the Erdas IMAGINE Spatial Modeler Language (SML). These processes are executed automatically by IceTools after the extraction of glacier frontal positions. The steps are as follows (Figure 6.6):

(1) spectral signatures are selected for the corresponding image to be classified (i.e., TM, ETM+ or ASTER);

(2) maximum likelihood classification is performed for each glacier centerline image;

(3) pixels classified as bare ice glacier zone above 500 m altitude or with MIR reflectance higher than 0.05 are reclassified as no data, reducing the possibility of shadows caused by the topography or clouds being classified as ice. Centerline DEMs are used as source of topographic information; and

(4) for all classes, clusters smaller than 250 (TM and ETM+) and 1000 pixels

(ASTER) are incorporated in the surrounding class. It reduces misclassification due to shadows of clouds and features like snow patches and ice falls.

A set of categorised images is resulting from the classification process described above. To derive the boundaries between the classified glacier zones, a general routine described in chapter 4.5 is used. Figure 6.6 illustrates the whole process of classification and extraction of points representing glacier zonal limits.

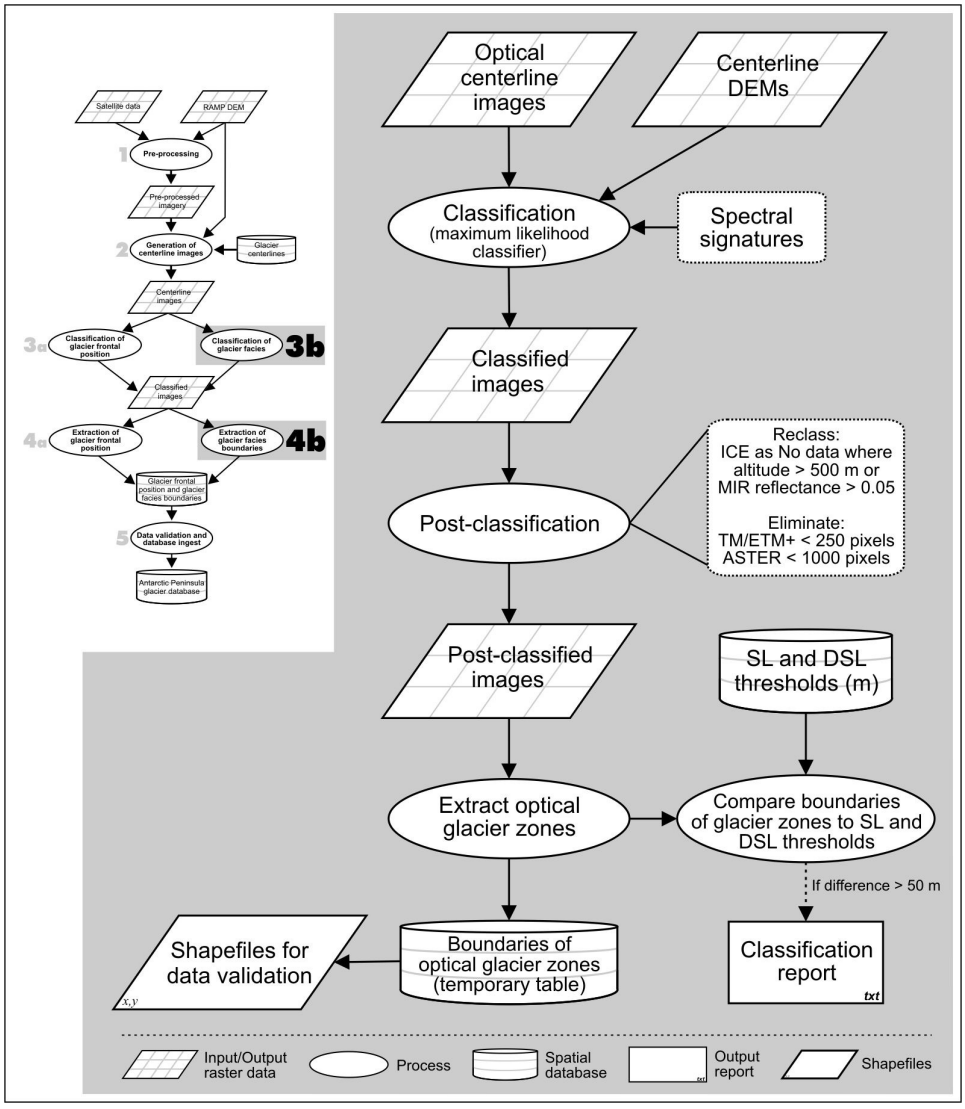

Figure 6.6: *Diagram illustrating the processing steps for extraction of boundaries between optical glacier zones from segmented Landsat TM/ETM+ and Terra ASTER data.*

7 Potential of the method

In this chapter, the potential of the developed centerline approach and its computational implementation (i.e., IceTools) is discussed. This is done by describing the processing time required for a complete analysis of radar and optical scenes, and estimating the time needed to analyse the datasets corresponding to an annual snapshot of the 240 glaciers monitored by the system. Furthermore, a discussion is realised about how the IceTools is prepared for additional datasets.

7.1 Considerations on processing time

The processing time of the developed routines depends on computational power of the workstation used for image analysis, spatial resolution and swath width of the satellite scene as well as the amount and size of glaciers analysed per image. In this work, algorithms were developed and tested using a notebook with an Intel Celeron M processor running at 1500 MHz (Table 7.1). The operational system used is the Windows XP Home Edition. The amount of glaciers to be analysed differs for each scene footprint. Thus, in order to estimate the processing time required for the complete image analysis and validation, about 20 glaciers per image are considered for radar or Landsat TM/ETM+ data, and 10 for Terra ASTER imagery.

As described in chapter 4, IceTools uses components of the following softwares:

PostgreSQL/PostGIS, BEST and Erdas IMAGINE. PostgreSQL/PostGIS can run on a remote server, not demanding resources of the computer were image analyses are carried out. Nevertheless, this software was installed locally for development and tests, showing that also in case of analyses with maximum amount of glaciers per image it does not require more than 10 minutes for executing the SQL statements used in IceTools. System requirements of BEST and Erdas IMAGINE are covered by the computer used (Table 7.1).

Table 7.1: *Configuration of the computer used to develop and test the routines of IceTools, and minimum system requirements to run the software used in its processing chain (Leica Geosystems, 2003; ESA, 2006b).*

	Computer used for development and tests	**System requirements for Erdas IMAGINE 8.7**	**System requirements for BEST 4.0.3**
Processor	Intel Celeron M, 1500 MHz	Intel Pentium 2	Intel Pentium 3, 800 MHz
Random access memory (RAM) (megabytes)	512	256 (512 highly recommended)	256

The most time consuming part of an analysis is the data pre-processing (Table 7.2), including the selection of GCPs for orthorectification (SAR images) or co-registration (optical data). Nevertheless, it is significantly reduced after analysing the first scene of a specific location (i.e., frame and track or path and row). Hereby, GCPs are selected for the first image to be analysed and also used for processing subsequent images. Furthermore, the use of workstations with faster processors reduces the time needed for data pre-processing, generation of centerline images, and classification. The differences in time among the datasets in table 7.2 are due to different algorithms used for image pre-processing and classification of SAR and optical data, and different spatial resolution and swath width of Landsat TM/ETM+ and Terra ASTER images.

Another important point to be considered is that the only processing step which requires a scientist trained in remote sensing and glaciology is the data validation and database ingest. It avoids misclassified results being incorporated to the database. The whole pre-processing and classification steps require a few interactions (Chapter 4.1) which can be done by students with some background in remote sensing.

Table 7.2: *Processing time estimated for carrying out a complete image analysis using the processing chain proposed in chapter 4, and an annual snapshot of the 240 glaciers monitored on the Antarctic Peninsula.*

	Processing step	Estimated time for processing each dataset (minutes)		
		ERS-1/2 SAR and Envisat ASAR	Landsat TM/ETM+	Terra ASTER
Processing of a complete image analysis	Selection of GCPs	20	30	20
	Pre-processing	70	40	30
	Generation and classification of centerline images	45	35	15
	Data validation and database ingest	25	25	15
	Total time for a complete analysis	160	130	80
Processing of a complete snapshot	Pre-processing	2100	800	2400
	Generation and classification of centerline images	1350	700	1200
	Data validation and database ingest	750	500	1800
	Total time for a complete snapshot	4200 (70 hours)	2000 (33.3 hours)	5400 (90 hours)

A complete snapshot of the 240 glaciers monitored on the AP in a determined time is achieved by analysing 30 (ERS-1/2 SAR or Envisat ASAR), 20 (Landsat TM/ETM+), or 80 images (Terra ASTER). Therefore, it requires between 33.3 and 90 hours of processing, depending on the dataset (Table 7.2). Selection of GCPs is not taken into account for this estimation, because it is not a recurring activity. Considering one scientist and one student working on that at two workstations for 6 and 4 hours a day respectively, a complete snapshot can be retrieved in less than two weeks from any dataset. As the pre-processing and classification steps can be programmed to be executed automatically for several files in batch mode, it does not require the full attention of the analysts to run. Thus, these processes can be executed even at night, reducing the two weeks estimated for a snapshot.

7.2 New and improved datasets

Several existing and future satellite datasets have the potential to be analysed with the centerline approach. Table 7.3 summarises the main characteristics of some existing or future satellite sensors identified as possible source of data to derive multi-temporal information on glacier parameters. They will acquired datasets with complementary frequency and polarisation modes (e.g., ALOS PALSAR, Radarsat, Radarsat-2, TerraSAR-X), and improved spatial resolution (e.g., ALOS AVNIR-2, CBERS-3 CCD, TerraSAR-X). Furthermore, even different image modes of Envisat ASAR (i.e., Wide Swath, alternating polarization) can be further investigated.

Table 7.3: *Main characteristics of potential sensors to be used as source of data for centerline approach analyses.*

Platform	Radarsat-1	Radarsat-2	TerraSAR-X	ALOS	CBERS-3
Sensor	SAR	SAR	SAR	PALSAR/ AVNIR-2	PANMUX, MUXCAM
Launch date	Nov. 1995	Mar. 2007	Oct. 2006	Jan. 2006	2008
Scheduled lifetime	5 years, but is still operating	7 years	5 years	3-5 years	3 years
Bands	C (5.6 cm)	C (5.6 cm)	X (3.1 cm)	L (cm) VIS and IR	VIS and IR
Polarisation	HH	Single, dual or multi-polarisation in HH, VV, HV, VH combinations	Single or dual in HH, VV, HV, VH combinations	Single, dual or multi-polarisation in HH, HV, VH, VV combinations (PALSAR)	
Ground resolution (m)	8-100	3-100	1-16	7-100/ 10	5-20
Swath width (km)	45-500	10-500	5-100	30-350/ 70	60-120

The modular structure of the developed methods (chapter 4) enables an unproblematic integration of algorithms from additional datasets. The following compilation describe procedures recommended for adapting the developed routines for new or improved datasets. It is necessary:

- to carry out a comprehensive bibliographic review about the applications of

the sensor or similar sensors for classification of ice and snow surfaces;

- to identify the pre-processing steps necessary to convert the data to common radiometric scale (i.e., backscatter coefficients for SAR data and reflectance values for optical imagery);
- to develop or to adapt algorithms for classifying glacier facies and glacier frontal position using the new dataset;
- to test the method developed for the sample of glaciers selected in chapter 3; and
- to implement the complete processing routine in IceTools.

8 Variations of glacier parameters on the Antarctic Peninsula

A multi-temporal analysis was carried out using algorithms developed in this work. Satellite datasets archived at the IPG and available through an ESA AO project were used for that. This chapter describes the resulting information on changes in boundaries between glacier facies and glacier frontal positions from 1986 to 2005.

8.1 Overview

Satellite data archived at the IPG is available for a preliminary analysis of variations in glacier parameters on the Antarctic Peninsula (AP) north of 70^{o} S. Datasets were selected considering the attempt of covering almost the entire study area for distributed time periods (Figure 8.1). In addition, complementary SAR data was requested within the ESA's CryoSat Data AO Project No. 2658, "Evaluating Cryosat's potential contribution to the quantification of mass balance and mass balance variations on the Antarctic Peninsula". The datasets used for the analysis consisted of 62 ERS-1/2 SAR, 6 Envisat ASAR, and 13 Landsat TM scenes (see Appendix, Tables A.3 and A.4), allowing 6 snapshots of the AP glaciers between 1986 and 2005 (Figure 8.1). TM data corresponds to original images of the GIA Landsat TM mosaic (Bennat et al., 1998), acquired between 1986 and 1989, and was used for the earliest snapshot of the glacier frontal position (Figure 8.1a). The available radar data enabled the coverage of the AP

between 1992 and 2005 (Figure 8.1b-8.1f) and was used for deriving information on both boundaries between glacier facies and position of ice fronts.

Image analyses were carried out using the methods developed within this investigation. Variations in glacier parameters observed in the data resulting from analyses are described in chapters 8.2-8.5. For investigating spatial patterns of changes, the AP was divided in west and east sides, and subdivided in four sectors of latitude: north of 64° S; between 64° S and 66° S; from 66° S to 68° S; and between 68° S and 70° S. The RAMP DEM (Liu et al., 2001; see chapter 2.3.2) was used as source for elevation data. However, to consider altitudinal variations also for changes detected in horizontal distances smaller than the RAMP DEM's original pixel size (200 m), it was resampled to 20 m using bilinear interpolation.

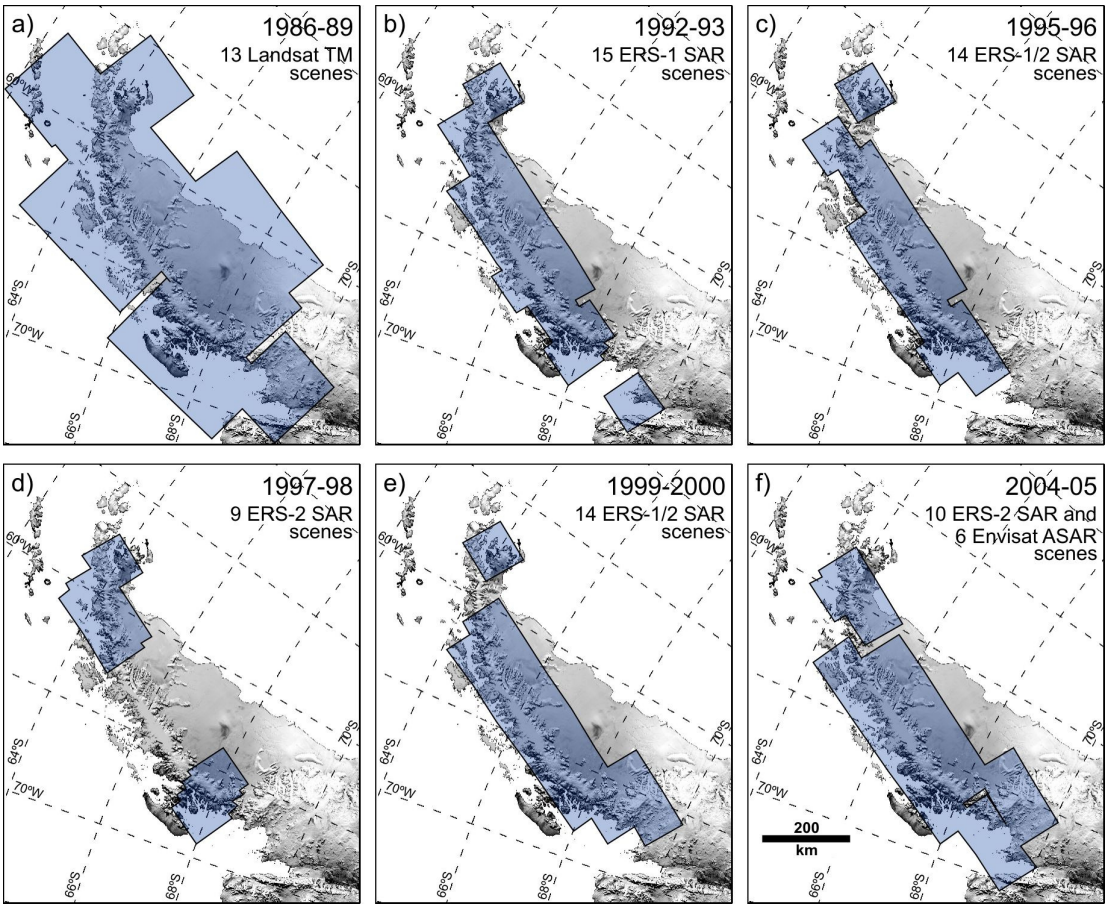

Figure 8.1: *Coverage of the satellite datasets used for multi-temporal analysis.*

8.2 Dry snow line

The occurrence of the dry snow radar zone (DSRZ; see chapters 2.1.1 and 5.2.1 for a comprehensive description about the dry snow zone and the dry snow radar zone respectively) was detected on 97 glaciers at total, being restricted to high areas on the plateaus of the AP (Rau and Braun, 2002). The only sector where no DSRZ was detected is located on the northeastern tip of the AP, where high altitude areas are limited to a small part of the Detroit Plateau.

The interpretation of the spatial and temporal patterns of dry snow line altitude (DSLA, chapter 2.1.6) resulting from this analysis is based on Rau et al. (2001) and Rau (2003). By modelling the backscattering (C-band; VV) for dry snow zones, Rau et al. (2001) found that to move the dry snow line downwards an increase in snow accumulation is necessary. Conversely, the only mechanism that is believed to cause a significant upward shift of the dry snow line is the impact of high temperatures (Rau, 2003).

The distribution of mean values of DSLA as detected for the last snapshot (2004/05) is presented in figure 8.2. On both sides of the AP, mean values of DSLA move downwards as we go south, agreeing with the southward decrease in mean annual surface temperatures as recorded for this region (Morris and Vaughan, 2003). Although the east side of the peninsula is 7°C colder than the west side (King and Turner, 1997), between 64° and 66°S the DSLA is higher in the east side. Mass balance data interpolated

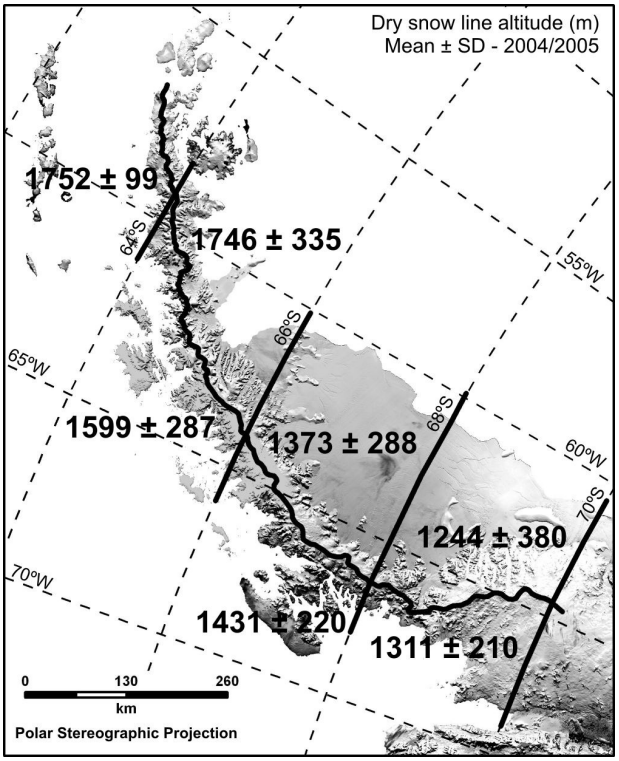

Figure 8.2: *Mean values of dry snow line altitude by sectors along the Antarctic Peninsula. Values in meters (with one standard deviation) as detected for 2004/05. The black lines show the boundaries of sectors used for analysis.*

for the AP (Turner et al., 2002) and changing precipitation patterns (Turner et al., 1997) indicate an increase in accumulation along the west coast of the AP, which may be contributing to maintain this difference. However, long-term continuous observations are needed to evaluate the impact of high temperature events on the DSLA of this sector.

As basis for the statistical analysis, the altitudinal differences of the dry snow line in meters per year were calculated for each glacier. Then, annual changes in DSLA were averaged in sectors along the AP and three time periods between 1992 and 2005 (Figure 8.3), defined based on data availability (Figure 8.1).

Upward changes in the DSLA were detected for all sectors over the period 1992-2005 (Figure 8.3a-g). Considering glaciers flowing to Larsen C Ice Shelf (between 66° and 70°S, Figure 8.3e and g), the observed increase in DSLA agrees with findings from Rau (2003) for the period from 1992 to 2000. This author shows the relationship of detected upward shift in DSLA with increase in high temperature events in San Martin Station during this time period. Here, it seems that over the whole AP extreme events of snow melting are reaching high altitude areas as response to increase in air temperature (Morris and Vaughan, 2003) and duration of warm periods (Torinesi et al., 2003). However, the magnitude and trend of observed changes are not the same for all sectors. While almost all sectors north of 68°S had a positive trend in DSLA, the recorded change shows a slight downward trend in the southern-most parts of the AP (Figure 8.3f-g).

A mean decrease in DSLA was detected on three regions only for the period from 1992 to 1996 (Figure 8.3a, c and d). As high accumulation (Turner et al., 2002) and precipitation records (Turner et al., 1997) coincides with the sectors north of 64°S and between 66° and 68°S, the dry snow line on these areas appears to had reacted to increased accumulation from 1992 to 1996. As almost no precipitation records are available for the east side of the AP, it is difficult to draw conclusions about the east sector between 64° and 66°S.

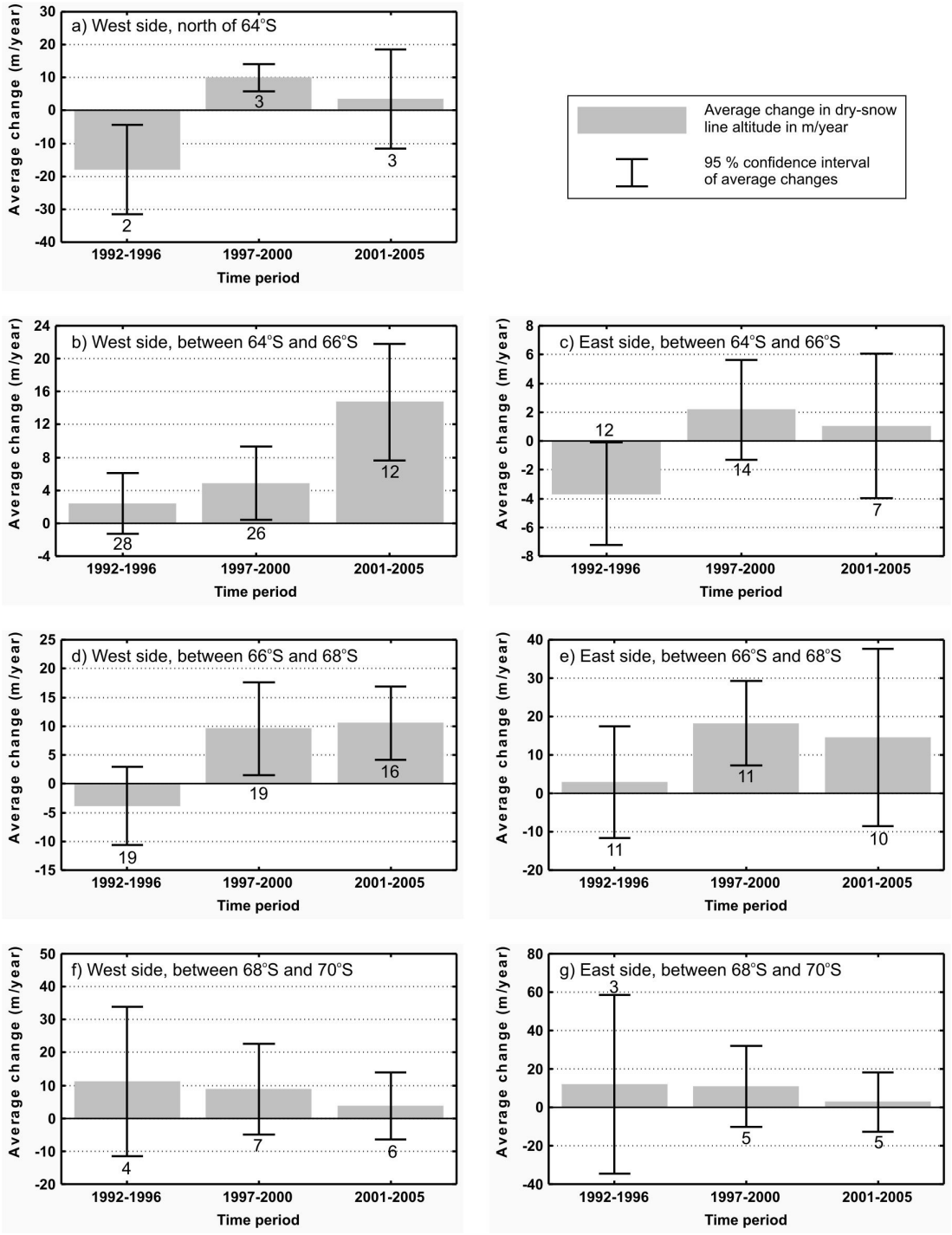

Figure 8.3: *Average change in dry snow line altitude over time (between 1992 and 2005) and by sectors along the Antarctic Peninsula. Negative and positive values correspond to mean downward and upward shifts of the dry snow line respectively, and are relative to the mean dry snow line altitude in the first year of the period. The numbers indicate the sample size of glaciers for each period. Note the different magnitude of change for each sector.*

8.3 Wet snow line

The development of a wet snow radar zone (WSRZ; see chapters 2.1.3 and 5.2.3 for a comprehensive description about the wet snow zone and the wet snow radar zone respectively) was detected on 158 glaciers distributed on both sides of the AP (Figure 8.4), reaching altitudes higher than 1000 m along the whole west coast and on the east coast north of 66°S (Figure 8.5).

In order to analyse the dependency of snow melt on temperature, mean values of the transient wet snow line altitude (WSLA) were compared to surface air temperature at the time of image acquisition. For that, glaciers were divided between the two sides of the AP, the nearest station on the corresponding side was searched for each glacier (Figure 8.4), and available temperature data was obtained from the Antarctic Meteorological Database at the British Antarctic Survey (BAS, www.antarctica.ac.uk/met/metlog).

A clear increase in mean WSLA with the increase in surface air temperature is shown for the west AP north of 68°S (Figure 8.5). It indicates the significance of air temperature as one of the main meteorological parameters influencing the energy input to snow cover on the western Antarctic Peninsula, as observed by Schneider (2000). The high variability in WSLA represented by one standard deviation bars in figure 8.5 indicates local variation in energy balance. Schneider (1998) showed the potential of

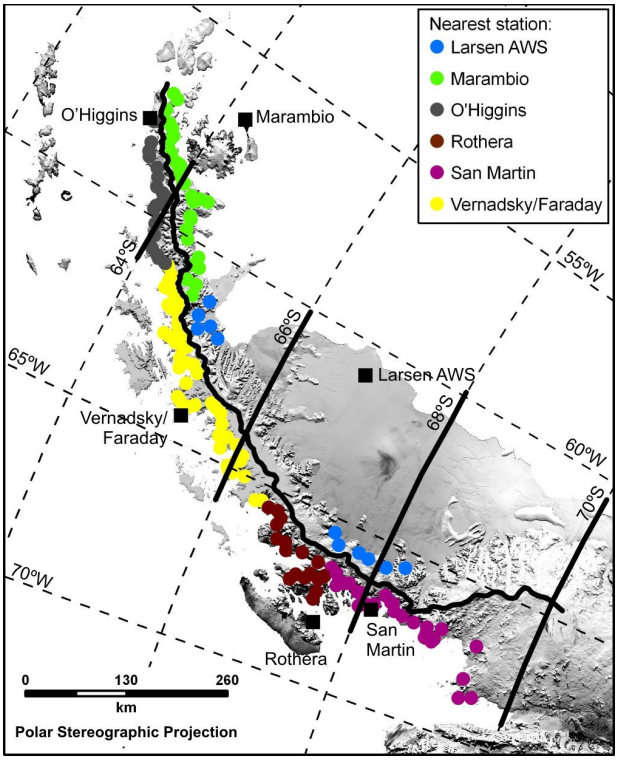

Figure 8.4: *Location of glaciers (coloured circles) where the development of wet snow radar zone was detected. The colours correspond to stations (black boxes) source of temperature data. The black lines show the boundaries of sectors used for analysis.*

these data for monitoring the local effects of weather patterns in a seasonal basis.

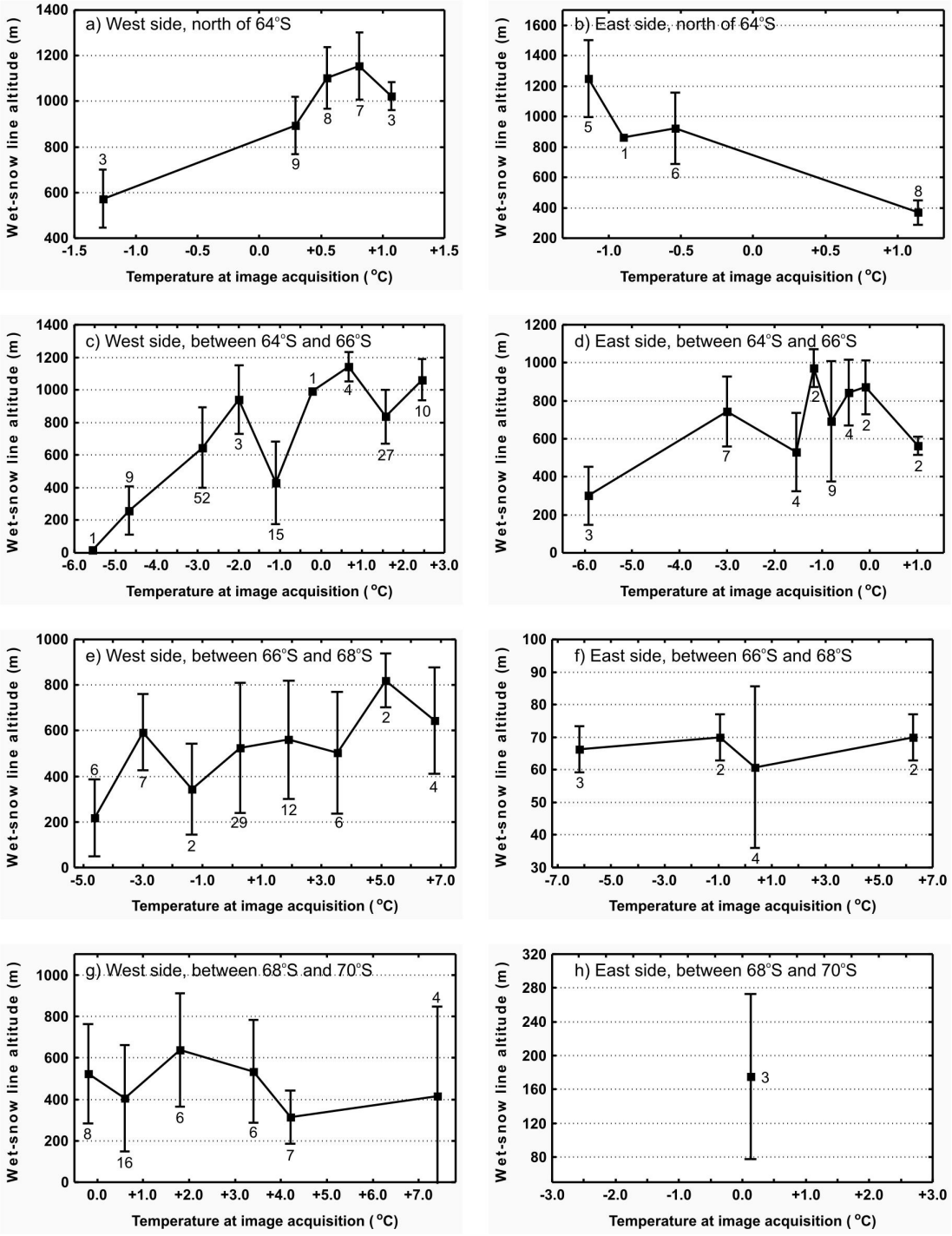

Figure 8.5: *Mean values of wet snow line altitude (m) and one standard deviation bars as detected on sectors of the Antarctic Peninsula. The numbers indicate the sample size of glaciers. Temperature data at the time of image acquisition was obtained from the nearest meteorological station. Source of temperature data: British Antarctic Survey (BAS, www.antarctica.ac.uk/met/metlog).*

Furthermore, several events of surface melting were detected even when the surface air temperatures were negative. This occurred on both sides of the AP, and indicates the occurrence of positive temperatures prior to image acquisition. After the occurrence of positive temperatures, the temperature dropped to below $0^{o}C$ and the snow started to freeze at the surface, although the thermal isolation of the snow layers restrained the heat exchange of the snowpack with the cold air at the surface (i.e., the radiation balance is still positive at the image acquisition; Torinesi et al., 2003). Events of positive air temperature at meteorological stations of reference during the 96 hours prior to image acquisition support this interpretation. A short time period with slightly negative temperatures is not enough to develop large snow grains, ice pipes and layers, which act as strong scatters of the radar beam and increase the volume scattering (Rau et al., 2001). The widespread occurrence of these phenomena indicates that simple models of snow melting or mass balance based on positive degree-days from temperature measured at nearby stations may be underestimating the energy still available for melting in the snowpack. Such models can be improved simply by considering snowpack information derived from SAR data (Schneider, 1998).

Finally, the thermal inversion over the east AP (Morris and Vaughan, 2003) appears to be the phenomenon responsible not only for low temperature records at near surface during melting events in this region, but also for increase in WSLA with the decrease in temperatures observed in figure 8.5b.

8.4 Snow line

The development of a bare ice radar zone (BIRZ; a comprehensive description about the ablation area and the bare ice radar zone is given in chapters 2.1.5 and 5.2.4) was detected on 83 glaciers in total, 53 glaciers along the western side of the Antarctic Peninsula and 30 on the northeastern region. However, as equilibrium line altitude on the west AP is almost at sea level, the development of a bare ice radar zone on glaciers on this area is patchy and irregularly distributed on time. On the other hand, a good time series of observations (Figure 8.6) was documented for 26 glaciers in the east Trinity Peninsula (TPE), and is discussed

here. This region coincides with the area of highest annual positive degree-days (PDDs) in the AP, as modelled by Vaughan (2006).

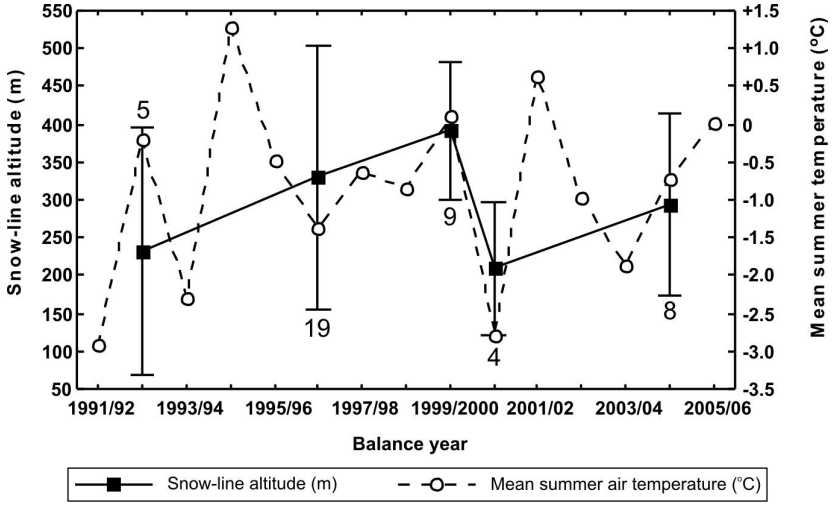

Figure 8.6: *Mean values of snow-line altitude (m) and one standard deviation bars as detected on glaciers at the east side of the Trinity Peninsula. The numbers indicate the sample size of glaciers for each balance year. The circles correspond to mean summer air temperature recorded at Marambio station.*

Mean value of snowline altitude (SLA) calculated for each balance year using only data from glaciers where a BIRZ was detected is depicted in figure 8.6. The maximum value of SLA was 392 ± 91 m for the balance year 1999/2000. This agrees with the lowest value of annual net mass balance (-0.56 m w.e.) recorded for this balance year by Skvarca et al. (2004) for the time series 1999/2000-2002/03 of the Glaciar Bahía del Diablo (Vega Island; 63^{o} 50' S; 57^{o} 25' W). In addition, the mean SLA in the east coast of the TPE shows a good correlation with variations in the mean summer air-temperature (MSAT; December-February) records of Marambio station (Figure 8.6). MSAT's are responsible for glacier-surface melting and run-off (Skvarca and De Angelis, 2003). However, the MSLA (233 ± 163 m) detected for the balance year 1992/93 does not agree with the MSAT recorded for this time period. The lack of precipitation data or field information makes difficult the interpretation of this occurrence, because an event such as a new snow fall followed by snow melting and metamorphism could mask the bare ice zone detectable by SAR sensors. Finally, the set of monitored glaciers can be reacting to the positive trends in annual positive degree-days described by

Vaughan (2006) for the northeast Trinity Peninsula. The good correlation of the SLA with the MSAT shows that the SLA as detected by SAR sensors can be used to test this hypothesis.

8.5 Glacier frontal position

Analyses of glacier frontal position were carried out on 184 glaciers, allowing the detection and estimation of average changes over time (between 1986 and 2005) and by sectors of the Antarctic Peninsula (Figure 8.7). As basis for statistical analysis, the differences in position of ice fronts were calculated for each glacier. Variations smaller than the estimated maximum RMSE resulting from image co-registering and orthorectification (60 m; see chapters 5.3.3 and 6.3.1) were considered as *no change*. Then, positional variations were calculated in meters per year, and annual changes were averaged in sectors along the AP and four time periods (Figure 8.7), defined based on the data availability (Figure 8.1). Due to lack of data available (Figure 8.1), east sectors of the Antarctic Peninsula between 66° and 70°S were not analysed.

Considering the entire period of analysis, recession of ice fronts was detected for 108 glaciers (59%) of the 184 investigated (Figure 8.8a), while 45 glaciers (24%) showed advancing ice fronts (Figure 8.8b), and 31 glaciers (17%) were found to be in a stationary condition. According to morphological classification data from the Antarctic Peninsula glacier inventory (chapter 2.3.3), the 108 retreating glaciers detected here consist in its majority of glaciers with floating termini (45%), ice shelf nourishing glaciers (24%), and tidewater glaciers (18%). Whereas 49% of the advancing glaciers have floating termini and 31% are tidewater glaciers.

The dominance of negative values in figure 8.7 shows the higher magnitude of variations detected for retreating glaciers in comparison with advancing glaciers. The extreme loss of ice represented on figure 8.7d corresponds to the disintegration and further retreat of the ice shelf in Prince Gustav Channel (Skvarca, 1993; Rott et al., 1996) and two sections of the Larsen Ice Shelf: A and B (Skvarca et al., 1999a; Rack and Rott, 2004). In addition, variations observed for the west side of the AP between 68° and 70°S (Figure 8.7f) result from retreat of

remaining parts of the Wordie Ice Shelf (Rignot et al., 2005).

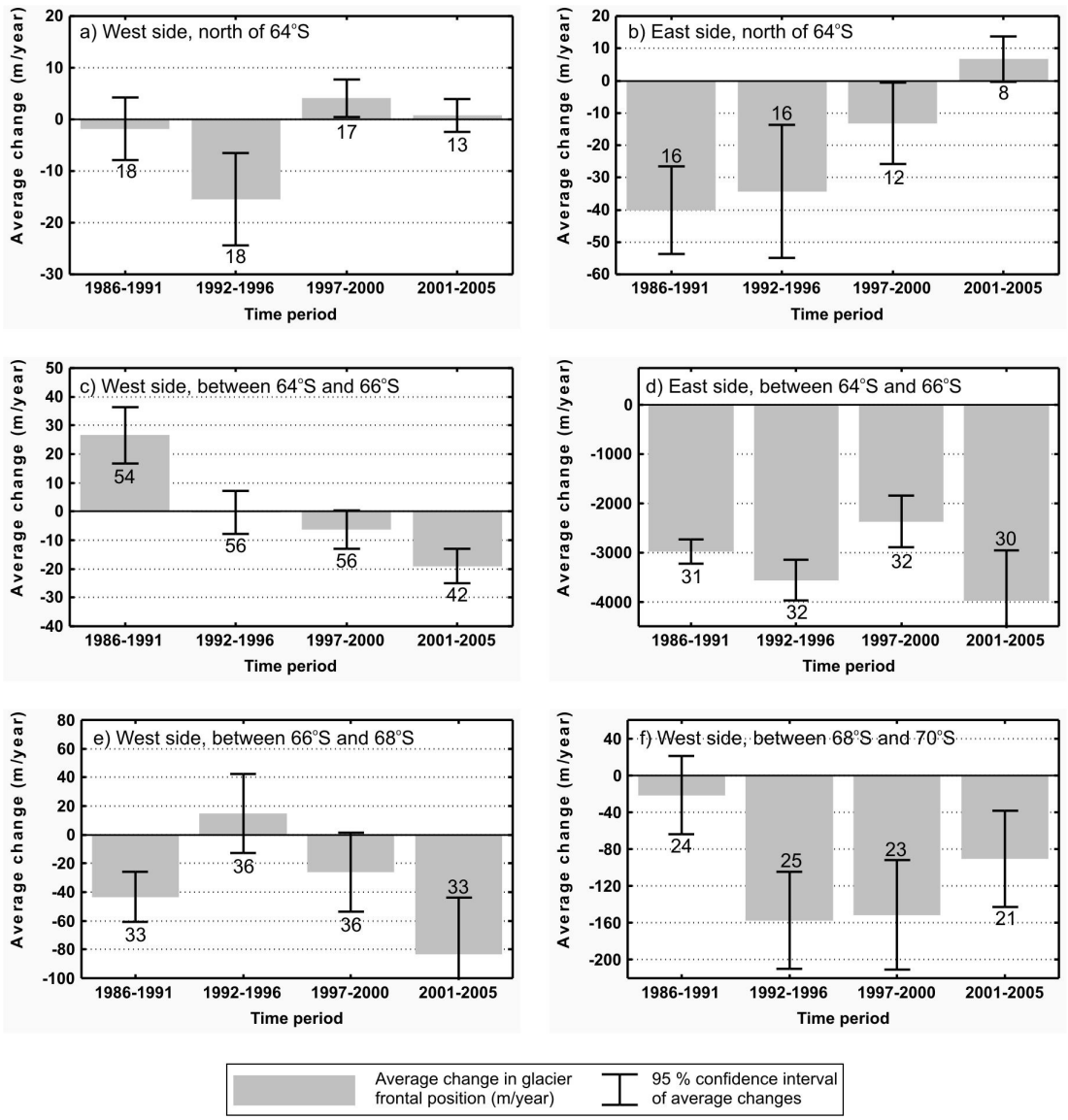

Figure 8.7: *Average change in glacier frontal position over time (between 1986 and 2005) and by sectors of the Antarctic Peninsula. Negative and positive values correspond to glacier retreat and advance respectively, and were measured along the glacier centerlines. The numbers indicate the sample size of glaciers for each period. Due to lack of data available, east sectors of the Antarctic Peninsula between 66° and 70°S were not analysed. Note the different magnitude of change for each sector. The high average change on d corresponds to disintegration and further retreat of the ice shelf in Prince Gustav Channel and two sections of the Larsen Ice Shelf: A and B.*

A clear upward trend is observed in change rates for glaciers on the eastern side of the AP, north of 64°S (Figure 8.7b). In this sector, the rate of ice loss decreased with time and showed an advance between 2001 and 2005. On the western side,

glaciers advanced from 1997 to 2000, also after a period of recession (1992-1996), but revealed stationary ice fronts during the last phase. Vaughan (2006) supposes that the increase in surface melting on the northern AP, caused by rising positive degree-days and duration of warm periods (Torinesi et al., 2003) is doing that more surface meltwater could reach the glacier base, which is known to increase glacier flow speeds (Zwally et al., 2002b). This can be contributing for the advance of ice fronts detected on the northern tip of the AP. However, glacier velocity data is needed to proof this assumption.

On the other hand, the two sectors between 64° and 68°S on the western side of the AP transitioned from advance to retreat and showed an increase in ice loss with time. The increase in retreat rates in this region agree with findings from Cook et al. (2005).

Although the overall pattern of

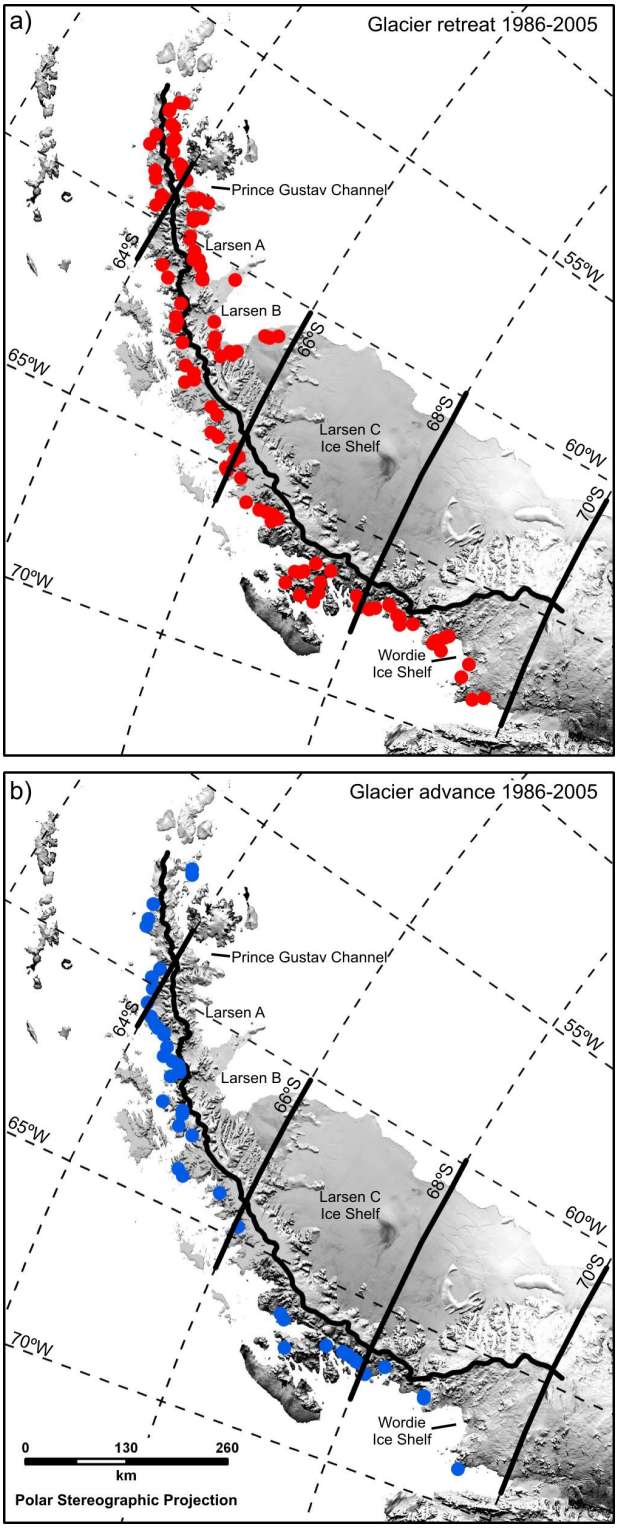

Figure 8.8: *Overall change in glacier frontal position on the Antarctic Peninsula from 1986 to 2005 as detected by the centerline approach. Due to lack of data available, east sectors of the Antarctic Peninsula between 66° and 70°S were not analysed. The black lines show the boundaries of sectors used for analysis.*

changes in glacier frontal position (Figure 8.8) shows a mixed distribution of retreating and advancing ice fronts along the west coast and northeastern tip of the AP, the predominance of ice loss is evident in almost all areas (Figure 8.7), confirming the previously reported trend in glacier recession on the AP detected using methods based on manual digitalisation of ice fronts (Rau et al. 2004; Cook et al., 2005). As suggested by Cook et al. (2005), floating glaciers may be reacting to the progressive atmospheric warming detected on the AP (Vaughan et al., 2003), like do the ice shelves (Morris and Vaughan, 2003; Scambos et al., 2003). However, as they are influenced by other external factors (e.g., oceanic temperature and circulation), it is difficult to distinguish a clear climate signal (Rau et al., 2004). Tidewater glaciers with their fully grounded marine termini are influenced by a complex set of forcings composed by atmospheric temperature, oceanographic parameters and subglacial topography (Van der Veen, 2002), and can not be used directly for understanding influence of short time climate change on ice masses (Pfeffer, 2003).

9 Conclusions and outlook

9.1 Main results

The overall aim of this thesis is the development of methods for semi-automatic extraction of glacier parameters (i.e., boundaries between glacier zones and glacier frontal position) on the Antarctic Peninsula using multi-temporal and multi-sensor remote sensing datasets.

The main results of this work can be summarised as follows:

- A new methodological approach is proposed. The so-called centerline approach simplifies the current methodology based on analyses of entire glacier catchments, facilitating the pre-processing and classification of remote sensing data acquired on glaciers. In addition, this approach enables the integration of satellite data from different sources, and minimises the needs of high resolution DEMs for terrain correction. Furthermore, it can be adapted for deriving further glacier parameters along the centerline (e.g., glacier velocity vectors).

- A multi-sensor processing chain to extract the above mentioned glacier parameters from satellite imagery using the centerline approach is described. Routines are implemented in PHP and PHP-GTK2 to reduce the analyst interaction with image processing software and database system, resulting in an application called IceTools.

- The developed algorithms for the classification of SAR (i.e., ERS-1/2 SAR and Envisat ASAR) and optical imagery (i.e., Landsat TM/ETM+ and Terra ASTER) are explained. The modular structure of the implemented processing chain enables an unproblematic integration of algorithms for classifying datasets from future sensors.

- A preliminary analysis of spatial and temporal distribution of satellite derived glacier parameters on the Antarctic Peninsula shows that climate related boundaries between glacier zones (i.e., the dry snow line and the snow line) as well as glacier fronts have different spatial patterns of change on this region. These patterns vary within the covered time period of the study (1986-2005), confirming the assumption (Rignot and Thomas, 2002) that changes in climatological and glaciological conditions on a relatively short time scale are usual for this region. Furthermore, the widespread persistence of a wet snow radar zone is proved even when the air temperature sinks below 0^{o}C. As a consequence it can be stated that simple models of snow melting or mass balance based on positive degree-days from temperature measured at nearby stations tend to underestimate the energy available for melting in the snow pack.

9.2 Future work

The results of image analyses presented in chapter 8, and the possibility of using the centerline approach in a productive workflow (chapter 7) demonstrated the potential of this method for generating a high-resolution multi-temporal database on glacier parameters for the Antarctic Peninsula. Satellite data will be available for that from several announcement of opportunities (AO's) for the International Polar Year (IPY) 2007-2008 (e.g., ESA IPY AO, DLR TerraSAR-X AO). It is expected to enable: the analysis of impact from extreme events of high temperature and extended warm periods on the dry snow line altitude; the improvement of snow melting and mass balance models based on temperature data; and an improvement in the record of short-time dynamics of ice fronts in a regional scale. Moreover, these products will be a contribution for two official

activities of the IPY 2007-2008: activity No. 34, Impact of climate induced glacial melting on marine and terrestric coastal communities on a gradient along the Western Antarctic Peninsula (ClicOPEN); and activity No. 107, IPY in the Antarctic Peninsula – Ice and Climate (IPY-AP).

The implementation of the processing chain for image analysis is based on a mix of free and proprietary software. Nevertheless, the design of IceTools enables the replacement of proprietary by free software, making it independent from paid software licenses.

Further work will also be concentrated on development of algorithms for new and existing satellite sensor data (see table 7.3). By allowing the monitoring of small glaciers, high-resolution SAR and optical sensors (e.g., TerraSAR-X, Radarsat-2, ALOS, CBERS) should expand the amount of glaciers to be analysed using the centerline approach. Complementary to these datasets, satellite imagery with high temporal resolution (e.g., Envisat ASAR Wide Swath) will enable the extraction of glacier parameters for development of statistical models of snow melting on the Antarctic Peninsula. Furthermore, improved DEMs (e.g., ASTER DEM) will increase the spatial accuracy of derived spatio-temporal patterns of glacier parameters and indicators of climate change.

10 References

ABDALATI W. and K. STEFFEN (1997): Snowmelt on the Greenland ice sheet as derived from passive microwave satellite data. *Journal of Climate* **10** (2), 165-175.

ABRAMS M., S. HOOK and B. RAMACHANDRAN (2002): *ASTER user handbook*. JPL Publication, v. 2, 135 p.

ALBRIGHT T., T. PAINTER, D. ROBERTS, J. SHI, J. DOZIER and E. FIELDING (1998): Classification of surface types using SIR-C/X-SAR, Mount Everest Area, Tibet. *Journal of Geophysical Research* **103** (E11), 25823-25837.

ALLEY R. B., P. U. CLARK, P. HUYBRECHTS and I. JOUGHIN (2005): Ice-Sheet and Sea-Level Changes. *Science* **310** (5747), 456-460.

ASHCRAFT, I. S. and D. G. LONG (2005): Observation and characterization of radar backscatter over Greenland. *IEEE Transactions on Geoscience and Remote Sensing* **43** (2), 225-237.

BARDEL P., A. G. FOUNTAIN, D. K. HALL, and R. KWOK (2002): Synthetic aperture radar detection of the snowline on Commonwealth and Howard Glaciers, Taylor Valley, Antarctica. *Annals of Glaciology* **34**, 177-183.

BENNAT H., H. HEIDRICH, J. GRIMM, J. SIEVERS, H. WALTER and A. WIEDEMANN (1998): Das “Geowissenschaftliche Informationssystem Antarktis“ (GIA) am Institut für Angewandte Geodäsie (IfAG). In GOßMANN H. (ed.): *Patagonien und Antarktis – Geofernerkundung mit ERS-1-Radarbildern*. Petermanns Geographische Mitteilungen, 13-34.

BENSON C. S. (1996): Stratigraphic studies in the snow and firn of the Greenland ice sheet. Snow, Ice and Permafrost Establishment. *Research Report* **70** (Revised edition of 1962 report), 182 p.

BORESJÖ-BRONGE L. and C. BRONGE (1999): Ice and snow-type classification in the Vestfold Hills, East Antarctica, us-ing Landsat-TM data and ground radiometer measurements. *International Journal of Remote Sensing* **20**, 225-240.

BRAUN M. and F. RAU (2001): Using a multi-year data archive of ERS SAR imagery for monitoring snow line positions and ablation patterns on the King George Island ice cap (Antarctica). *EARSeL eProceedings* **1** (1), 281-291.

BRAUN M. and H. GOßMANN (2002): Glacial changes in the areas of Admiralty Bay and Potter Cove, King George Island, Maritime Antarctica. In BEYER L. and M. BÖLTER (eds.): *Geoecology of Antarctic Ice-Free Coastal Landscapes*. Springer Verlag, 75-89.

BRAUN M., F. RAU, H. SAURER and H. GOßMANN (2000): Development of radar glacier zones on the King George Island ice cap, Antarctica, during the austral summer 1996/97 as observed in ERS-2 SAR-data. *Annals of Glaciology* **31**, 357-363.

CALVET J., D. GARCÍA SELLÉS and J. CORBERA (1999): Fluctuaciones de la extensión del casquete glacial de la isla Livingston (Shetland del Sur) desde 1956 hasta 1996. *Acta Geologica Hispanica* **34** (4), 365-374.

CASACCHIA R., R. SALVATORI, A. CAGNATI, M. VALT and S. GHERGO (2002): Field reflectance of snow/ice covers at Terra Nova Bay, Antarctica. *International Journal of Remote Sensing* **23** (21), 4653-4667.

CAVALIERI D. J., C. L. PARKINSON, P. GLOERSEN, J. C. COMISO and H. J. ZWALLY (1999): Deriving long-term time series of sea ice cover from satellite passive microwave multisensor data sets, *Journal of Geophysical Research* **104**, 15803-15814.

CCRS (2002): *Fundamentals of remote sensing* (Canada Centre for remote sensing). URL: http://ccrs.nrcan.gc.ca/resource/tutor/fundam/index_e.php, accessed on 25 October 2006.

CHANDER G. and B. L. MARKHAM (2003): Revised Landsat 5 TM radiometric calibration procedures and post-calibration dynamic ranges. *IEEE Transactions on Geoscience and Remote Sensing* **41** (11), 2674-2677.

COLBECK S. C. (1982): Overview of seasonal snow metamorphism. *Reviews of Geophysics and Space Physics* **20** (1), 45-61.

COLBECK S. C. (1983): Theory of metamorphism of dry snow. *Journal of Geophysical Research* **88** (C9), 5475-5482.

COOK A. J., A. J. FOX, D. G. VAUGHAN AND J. G. FERRIGNO (2005): Retreating glacier fronts on the Antarctic Peninsula over the past half-century. *Science* **308** (5721), 541-544.

DE ANGELIS H. and P. SKVARCA (2003): Glacier surge after ice shelf collapse. *Science* **299** (5612), 1560-1562.

DOAKE C. S. M. and D. G. VAUGHAN (1991): Rapid disintegration of Wordie Ice Shelf in response to atmospheric warming. *Nature* **350**, 328-330.

DOZIER J. and B. MARKS (1987): Snow mapping and classification from Landsat Thematic Mapper data. *Annals of Glaciology* **9**, 97-103.

DOZIER J. (1989a): Spectral signature of alpine snow cover from the Landsat Thematic Mapper. *Remote Sensing of Environment* **28**, 9-22.

DOZIER J. (1989b): Estimation of properties of alpine snow from Landsat Thematic Mapper. *Advances in Space Research* **9** (1), 207-215.

DOZIER J. and T. H. PAINTER (2004): Multispectral and hyperspectral remote sensing of alpine snow properties. *Annual Review of Earth and Planetary Sciences* **32**, 465-494.

DREWRY D. L. and E. M. MORRIS (1992): The response of large ice sheets to climatic change. *Philosophical Transactions of the Royal Socienty London B* **338** (1285), 235-242.

ENGESET R. V. and D. J. WEYDAHL (1998): Analysis of glaciers and geomorphology on Svalbard using multitemporal ERS-1 SAR images. *IEEE Transactions on Geoscience and Remote Sensing* **36** (6), 1879-1887.

ESA (2005): *BEST (Basic Envisat SAR Toolbox) User Manual*. V. 4.0.3, 189 p. URL: ftp://ftp.esrin.esa.it/pub/astbx_ftp/ BEST_SUM_vb402.zip, accessed on 20 August 2006.

ESA (2006a): *Envisat ASAR Product Handbook*. Issue 2.1, 565 p. URL: http://envisat.esa.int/pub/ESA_DOC/ENVISAT/ASAR/asar.ProductHandbook.2_1.pdf.zip, accessed on 20 August 2006.

ESA (2006b): *BEST Software*. URL: http://earth.esa.int/best/software, accessed on 03 October 2006.

FAHNESTOCK M. A., R. A. BINDSCHADLER, R. KWOK and K. C. JEZEK (1993): Greenland ice sheet surface properties and ice dynamics from ERS-1 SAR Imagery. *Science* **262** (5139), 1530-1534.

FAHNESTOCK M. A., W. ABDALATI and C. A. SHUMAN (2002): Long melt seasons on ice shelves of the Antarctic Peninsula: an analysis using satellite-based microwave emission measurements. *Annals of Glaciology* **34**, 127-133.

FILY M., B. BOURDELLES, J.P. DEDIEU and C. SERGENT (1997): Comparison of in situ and Landsat Thematic Mapper derived snow grain characteristics in the Alps. *Remote Sensing of Environment* **59**, 452-460.

FORSTER R. R., B. L. ISACKS and S. DAS (1996): Shuttle imaging radar (SIR-C/X-SAR) reveals near surface properties of the South Patagonian Icefield. *Journal of Geophysical Research* **101** (E10), 23169-23180.

FROST V. S., J. A. STILES, K. S. SHANMUGAN and J. C. HOLTZMANN (1982): A model for radar images and its application to adaptive digital filtering of multiplicative noise. *IEEE Transactions on Pattern Analysis and Machine Intelligence* **4**, 157-166.

GLOERSEN, P.,W. J. CAMPBELL, D. J. CAVALIERI, J. C. COMISO, C. L. PARKINSON and H. J. ZWALLY (1992): *Arctic and Antarctic sea ice, 1978–1987: Satellite passive-microwave observations and analysis*. NASA Special Publication 511, 290 p.

GREEN R. O., J. DOZIER, D. A. ROBERTS and T. H. PAINTER (2002): Spectral snow reflectance models for grain size and liquid water fraction in melting snow for the solar reflected spectrum. *Annals of Glaciology* **34**, 71-73.

HALL D. K. (1998): Remote sensing of snow and ice using imaging radar. In HENDERSON F. M. and A. J. LEWIS (eds.): *Principles and applications of imaging radar. Manual of remote sensing*. 3rd edition, Vol. 2, John Wiley & Sons Inc., 677-704.

HALL D. K., J. P. ORMSBY, R. A. BINDSCHADLER and H. SIDDALINGAIAH (1987): Characterization of snow and ice zones on glaciers using Landsat Thematic Mapper data. *Annals of Glaciology* **9**, 104-108.

HALL D. K., A. T. C. CHANG and H. SIDDALINGAIAH (1988): Reflectances of glaciers as calculated using Landsat-5 Thematic Mapper data. *Remote Sensing of Environment* **25**, 311-321.

HALL D. K., R. A. BINDSCHADLER, J. L. FOSTER, A. T. C. CHANG and H. SIDDALINGAIAH (1990): Comparison of in situ and satellite derived reflectances of Forbindels Glacier, Greenland. *International Journal of Remote Sensing* **11** (3), 493-504.

HALL D. K., J. L. FOSTER and A. T. C. CHANG (1992): Reflectance of snow as measured in situ and from space in sub-Arctic areas in Canada and Alaska. *IEEE Transactions on Geoscience and Remote Sensing* **30** (3), 634-637

HALL D. K. , G. A. RIGGS and V. V. SALOMONSON (1995): Development of methods for mapping global snow cover using moderate resolution imaging spectroradiometer data. *Remote Sensing of Environment* **54**:127-140.

HALL D. K. , G. A. RIGGS, V. V. SALOMONSON, N. DIGIROMAMO and K. J. BAYR (2002): MODIS snow-cover products. *Remote Sensing of Environment* **83**,181-194.

HEISKANEN J., K. KAJUUTTI, M. JACKSON, H. ELVEHØY and P. PELLIKKA (2003): Assessment of glaciological parame-ters using Landsat satellite data in Svartisen, northern Norway. *EARSeL eProceedings* **2** (1), 34-42.

HENDERSON F. M. and A. J. LEWIS (1998): *Principles and applications of imaging radar. Manual of remote sensing*. 3rd edition, Vol. 2., John Wiley & Sons Inc., 866 p.

IQBAL M. (1980): *An introduction to solar radiation*. Academic Press, 390 p.

JEZEK K. C. (1999): Glaciological properties of the Antarctic ice sheet from RADARSAT-1 synthetic aperture radar imagery. *Annals of Glaciology* **29**, 286-291.

JEZEK K. C., M. R. DRINKWATER, J. P. CRAWFORD, R. BINDSCHADLER and R. KWOK (1993): Analysis of synthetic aperture radar data collected over the southwestern Greenland ice sheet. *Journal of Glaciology* **39** (131), 119-132.

JEZEK K.C., P. GOGINENI and M. SHANABLEH (1994): Radar measurements of melt zones on the Greenland ice sheet. *Geophysical Research Letters* **21** (1), 33-36.

JPL (2001): ASTER Higher-Level Product User Guide. v. 2, JPL D-20062. URL: http://asterweb.jpl.nasa.gov/content/03_data/04_Documents/ASTERHigherLevelUserGuideVer2May01.pdf, accessed on 25 October 2006.

JPL (2006): ASTER – Advanced Spaceborne Thermal Emission and Reflection Radiometer. URL: http://asterweb.jpl.nasa.gov, accessed on 25 October 2006.

KÄÄB A., C. HUGGEL, F. PAUL, R. WESSELS, B. RAUP, H. KIEFFER and J. KARGEL (2003): Glacier monitoring from ASTER imagery: accuracy and applications. *EARSeL eProceedings* **2** (1), 43-53.

KING J. C. (1994): Recent climate variability in the vicinity of the Antarctic Peninsula. *International Journal of Climatology* **14**, 357-369.

KING J. C. and S. A. HARANGOZO (1998): Climate change in the western Antarctic Peninsula since 1945: observations and possible causes. *Annals of Glaciology* **27**, 571-575.

KING J.C. and TURNER J. (1997): *Antarctic meteorology and climatology*. Cambridge Atmospheric and Space Science Series, Cambridge University Press, 409 p.

KNAP W. H. and C. H. REIJMER (1998): Anisotropy of the reflected radiation field over melting glacier ice: Measurements in Landsat TM Bands 2 and 4. *Remote Sensing of Environment* **65**, 93-104.

KNAP W. H., B. W. BROCK, J. OERLEMANS and I. C. WILLIS (1999): Comparison of Landsat-TM derived and ground-based albedos of Haut Glacier d'Arolla,

Switzerland. *International Journal of Remote Sensing* **20** (17), 3293-3310.

KÖNIG M., J. G. WINTHER and E. ISAKSSON (2001): Measuring snow and glacier ice properties from satellite. *Reviews of Geophysics* **39** (1), 1-27.

KÖNIG M., J. WADHAM, J. G. WINTHER, J. KOHLER and A.-M. NUTTALL (2002): Detection of superimposed ice on the glaciers Kongsvegen and midre Lovénbreen, Svalbard, using SAR satellite imagery. *Annals of Glaciology* **34**, 335-342.

KWOK R., J. C. CURLANDER and S. S. PANDER (1987): Rectification of terrain induced distortions in radar imagery. *Photogrammetric Engineering and Remote Sensing* **53** (5), 507-513.

LAUR H., P. BALLY, P. MEADOWS, J. SANCHEZ, B. SCHÄTTLER, E. LOPINTO and D. ESTEBAN (2004): *Derivation of the backscattering coefficient σ° in ESA ERS SAR PRI products*. ESA/ESRIN, ESTN-RS-PM-HL09, Issue 2, Rev. 5f, 53 p.

LEE J. S. (1981): Speckle Analysis and Smoothing of Synthetic Aperture Radar Images. *Computer Graphics and Image Processing* **17**, 24-32.

LEE J. S. (1983): Digital image smoothing and the sigma filter. *Computer Vision, Graphics, and Image Processing* **24**, 255-269.

LEE J. S., I. JURKEVICH, P. DEWAELE, P. WAMBACQ and A. OOSTERLINK (1994): Speckle filtering of synthetic aperture radar images: a review. *Remote Sensing Reviews* **8**, 313-340.

LEICA GEOSYSTEMS (2003): *Erdas IMAGINE configuration guide for Windows*. Leica Geosystems LLC, 106 p.

LEWIS A. and F. HENDERSON (1998): Radar Fundamentals: The Geoscience Perspective. In HENDERSON F. M. and A. J. LEWIS: *Principles and applications of imaging radar. Manual of remote sensing*. Vol. 2., 3rd edition, John Wiley & Sons Inc., 131-182.

LI W., K. STAMNES, B. CHEN and X. XIONG (2001): Snow grain size retrieved from near-infrared radiances at multiple wavelengths. *Geophysical Research Letters* **28** (9), 1699-1702.

LI X., T. KOIKE and G. CHENG (2002): Retrieval of snow reflectance from Landsat data in rugged terrain. *Annals of Glaciology* **34**, 31-37.

LILLESAND T. M. and R. W. KIEFER (2000): *Remote sensing and image interpretation*. 4th Edition, John Wiley & Sons Inc., 724 p.

LIU H., K. C. JEZEK and B. LI (1999): Development of Antarctic digital elevation model by integrating cartographic and remotely sensed data: A geographic information system based approach. *Journal of Geophysical Research* **104**, 23199-23213.

LIU H., K. JEZEK, B. LI and Z. ZHAO (2001): *RADARSAT Antarctic Mapping Project digital elevation model version 2*. National Snow and Ice Data Center, Boulder. URL: http://nsidc.org/data/nsidc-0082.html, accessed on 25 October 2006.

LOPES A., R. TOUZI and E. NEZRY (1990a): Adaptive speckle filters and scene heterogeneity. *IEEE Transactions on Geoscience and Remote Sensing* **28**, 992-1000.

LOPES A., E. NEZRY, R. TOUZI and H. LAUR (1990b): Maximum A Posteriori Speckle Filtering and First Order Textural Models in SAR Images. *Proceedings of the International Geoscience and Remote Sensing Symposium* (IGARSS), College Park, Maryland, May 1990, 3, 2409-2412.

LUCCHITA B. K. and C. E. ROSANOVA (1998): Retreat of northern margins of George VI and Wilkins Ice Shelves, Antarctic Peninsula. *Annals of Glaciology* **27**, 41-46.

MARSHALL G. J., W. G. REES. and J. A. DOWDESWELL (1995): The discrimination of glacier facies using multi-temporal ERS-1 SAR data. In ASKNE J. (ed.): *Sensors and Environmental Applications of Remote Sensing*. Balkema, Rotterdam, 263-269.

MARSHALL G. J., V. LAGUN and T. A. LACHLAN-COPE (2002): Changes in Antarctic Peninsula tropospheric temperatures from 1956 to 1999: A synthesis of observations and reanalysis data. *International Journal of Climatology* **22** (3), 291-310.

MEADOWS P., H. LAUR and B. SCHÄTTLER (1998): The Calibration of ERS SAR Imagery for Land Applications. In BORGEAUD M. and T. D. GUYENNE (ed.): *Retrieval of Bio- and Geo-Physical Parameters from SAR Data for Land Applications. Proceedings of the second International Workshop*, October 21-

23, 1998, ESTEC, Noordwijk, ESA SP-441, 35-42.

MORRIS E. M. and D. G. VAUGHAN (2003): Spatial and temporal variation of surface temperature on the Antarctic Peninsula and the limit of viability of ice shelves. In DOMACK E., A. LEVENTER, A. BURNETT, R. BINDSCHADLER, P. CONVEY and M. KIRBY (eds.): *Antarctic Peninsula Climate Variability: Historical and Paleoenvironmental Perspectives*. Antarctic Research Series Volume 79, American Geophysical Union, 61-68.

MÜLLER F. (1962): Zonation in the accumulation area of the glaciers of Axel Heiberg Island, N.W.T., Canada. *Journal of Glaciology* **4** (33), 302-311.

NAGAO M. and T. MATSUYAMA (1978): Edge preserving smoothing. *Computer Graphics and Image Processing* **9**, 394-407.

NASA (2006): *Landsat 7 science data users handbook*. URL: http://ltpwww.gsfc.nasa.gov/IAS/handbook/handbook_toc.html, accessed on 25 October 2006.

NDI NYOUNGUI A., E. TONYE and A. AKONO (2002): Evaluation of speckle filtering and texture analysis methods for land cover classification from SAR images. *International Journal of Remote Sensing* **23** (9): 1895-1925.

PAINTER T. H. and J. DOZIER (2004): The effect of anisotropic reflectance on imaging spectroscopy of snow properties. *Remote Sensing of Environment* **89**, 409-422.

PARK B.-K., S.-K. CHANG, H. I. YOON and H. CHUNG (1998): Recent retreat of ice cliffs, King George Island, South Shetland Islands, Antarctic Peninsula. *Annals of Glaciology* **27**, 633-635.

PARKINSON C. L. (2002): Trends in the length of the Southern Ocean sea-ice season, 1979–99. *Annals of Glaciology* **34**, 435-440.

PARTINGTON K. C. (1998): Discrimination of glacier facies using multi-temporal SAR data. *Journal of Glaciology* **44** (146), 480-488.

PATERSON W. S. B. (1994): *The physics of glaciers*. Elsevier Science Ltd., 480 p.

PAUL F. (2001): Evaluation of different methods for glacier mapping using Landsat TM. *EARSeL eProceedings* **1** (1), 239-245.

PAUL F. (2003): *The new Swiss glacier inventory 2000: application of remote sensing and GIS*. Unpublished PhD Thesis, Universität Zürich, 194 p.

PEEL D. A. (1992): Spatial temperature and accumulation rate variations in the Antarctic Peninsula. In MORRIS E. M. (ed.): *The contribution of Antarctic Peninsula ice to sea level rise*. British Antarctic Survey Ice & Climate Special Report 1, 11-15.

PFEFFER W. T. (2003): Tidewater glaciers move at their own pace. *Nature* **426** (6967), 602.

RACK W. and H. ROTT (2004): Pattern of retreat and disintegration of Larsen B Ice Shelf, Antarctic Peninsula. *Annals of Glaciology* **39**, 505-510.

RAMAGE J. M. and B. L. ISACKS (1998): Seasonal Changes in Alaskan Radar Glacier Zones. *Proceedings of the Final ADRO Symposium*, 13th-15th of October 1998, Montreal, CD-ROM.

RAMAGE J. M., B. L. ISACKS and M. M. MILLER (2000): Radar glacier zones in southeast Alaska, U.S.A.: field and satellite observations. *Journal of Glaciology* **46** (153), 287-296.

RANEY R. K. (1998): Radar Fundamentals: Technical Perspective. In HENDERSON F. M. and A. J. LEWIS: *Principles and applications of imaging radar. Manual of remote sensing*. Vol. 2., 3rd edition, John Wiley & Sons Inc., 9-130.

RAU F. (2003): The upward shift of the dry snow line on the northern Antarctic Peninsula. *EARSeL eProceedings* **2** (1), 113-121.

RAU F. and M. BRAUN (2002): The regional distribution of the dry snow zone on the Antarctic Peninsula north of 70º South. *Annals of Glaciology* **34**, 95-100.

RAU F. and H. SAURER (1998): Investigations into snow cover dynamics on two glaciers in the central Marguerite Bay (Antarctic Peninsula) using ERS and RADARSAT SAR imagery. *Proceedings of the Final ADRO Symposium*, 13th-15th of October 1998, Montreal, CD-ROM.

RAU F., M. BRAUN, H. SAURER, H. GOßMANN, G. KOTHE, F. WEBER, M. EBEL and D. BEPPLER (2000): Monitoring multi-year snow cover dynamics on the Antarctic Peninsula. *Polarforschung* **67**(1/2), 27-40.

RAU F., M. BRAUN, M. FRIEDRICH, F. WEBER and H. GOßMANN (2001): Radar glacier zones and its boundaries as indicators of glacier mass balance and climatic variability. *EARSeL eProceedings* **1** (1), 317-327.

RAU F., F. MAUZ, H. DE ANGELIS, R. JAÑA, J. ARIGONY-NETO, P. SKVARCA, S. VOGT, H. SAURER and H. GOßMANN (2004): Variations of glacier frontal positions on the Northern Antarctic Peninsula. *Annals of Glaciology* **39**, 525-530.

RAU F., F. MAUZ, S. VOGT, S. J. S. KHALSA and B. RAUP (2005): *Illustrated GLIMS Glacier Classification Manual*. GLIMS Guides and Tutorials. 36 p. URL: http://www.glims.org/MapsAndDocs/assets/GLIMS_Glacier-Classification-Manual_V1_2005-02-10.pdf, accessed on 25 October 2006.

RAUP B. and S. J. S. KHALSA (2003): *A Method for Transferring GLIMS Analysis Products from Regional Centers to NSIDC*. URL: http://www.glims.org/MapsAndDocs/datatransfer/data_transfer_specification.html, accessed on 25 October 2006.

RAYMOND C., B. WEERTMAN, L. THOMPSON, E. MOSLEY-THOMPSON, D. PEEL, and R. MULVANEY (1996): Geometry, motion and mass balance of Dyer Plateau, Antarctica. *Journal of Glaciology* **42**, 510-518.

REES W. G. and M. J. F. SATCHELL (1997): The effect of median filtering on synthetic aperture radar images. *International Journal of Remote Sensing* **18** (13), 2887-2893.

REINIGER K.-D and A. ZIMMER (2000): The German Antarctic receiving station within the international ground segment for remote sensing. *Polarforschung* **67** (1/2), 3-6.

REYNOLDS J. M. (1981): The distribution of mean annual temperatures in the Antarctic Peninsula. *British Antarctic Survey Bulletin* **54**, 123-133.

RIGNOT E. and R. H. THOMAS (2002): Mass balance of polar ice sheets. *Science* **297** (5586), 1502-1506.

RIGNOT E., G. CASASSA, P. GOGINENI, W. KRABILL, A. RIVERA and R. H. THOMAS (2004): Accelerated ice discharge from the Antarctic Peninsula following the collapse of Larsen B ice shelf. *Geophysical Research Letters* **31** (18), L18401, doi:10.1029/2004GL020697.

RIGNOT E., G. CASASSA, P. GOGINENI, P. KANAGARATNAM, W. KRABILL, H. PRITCHARD, A. RIVERA, R. H. THOMAS, J. TURNER and D. VAUGHAN (2005): Recent ice loss from the Fleming and other glaciers, Wordie Bay, West Antarctic Peninsula. *Geophysical Research Letters* **32** (07), L07502, doi:10.1029/2004GL021947.

ROSICH B. and P. MEADOWS (2004): *Absolute calibration of ASAR level 1 products generated with PF-ASAR*. ESA/ESRIN, ENVI-CLVL-EOPG-TN-03-0010, Issue 1, Rev. 5. 26 p.

ROTT H., P. SKVARCA and T. NAGLER (1996): Rapid collapse of northern Larsen Ice Shelf, Antarctica. *Science* **271** (5250), 788-792.

ROTT H., W. RACK, T. NAGLER and P. SKVARCA (1998): Climatically induced retreat and collapse of northern Larsen Ice Shelf, Antarctic Peninsula. *Annals of Glaciology* **27**, 86-92.

ROTT H., W. RACK, P. SKVARCA and H. DE ANGELIS (2002): Northern Larsen Ice Shelf, Antarctica: further retreat after collapse. *Annals of Glaciology* **34**, 277-282.

SANDMEIER S. and K. I. ITTEN (1997): A physically-based model to correct atmospheric and illumination effects in optical satellite data of rugged terrain. *IEEE Transactions on Geoscience and Remote Sensing* **35** (3), 708-717.

SAURER H. and H. GOßMANN (2002): *Quantification and detection of regional disparities of glacial phenomena on the Antarctic Peninsula*. Application for funding by the Deutsche Forschungsgemeinschaft. 34 p.

SCAMBOS T. A., C. HULBE, M. FAHNESTOCK and J. BOHLANDER (2000): The link between climate warming and break up of ice shelves on the Antarctic Peninsula. *Journal of Glaciology* **46**, 516-530.

SCAMBOS T. A., C. HULBE and M. FAHNESTOCK (2003): Climate-induced ice shelf disintegration in the Antarctic Peninsula. In DOMACK E., A. LEVENTER, A. BURNETT, R. BINDSCHADLER, P. CONVEY and M. KIRBY (eds.): *Antarctic Peninsula Climate Variability: Historical and Paleoenvironmental Perspectives*. Antarctic Research Series Volume 79, American Geophysical Union, 77-92.

SCAMBOS T. A., J. A. BOHLANDER, C. A. SHUMAN and P. SKVARCA (2004): Glacier acceleration and thinning after ice shelf collapse in the Larsen B embayment, Antarctica. *Geophysical Research Letters* **31**(18), L18402, doi:10.1029/2004GL020670.

SEIDEL K. and J. MARTINEC (2004): *Remote sensing in snow hydrology: runoff modelling, effect of climate change*. Springer Verlag, 150 p.

SCHNEIDER C. (1998): Zur raumzeitlichen Differenzierung der Energiebilanz und des Zustandes der Schneedecke auf zwei Gletschern der Marguerite Bay, Antarktische Halbinsel. *Freiburger Geographische Hefte* **56**, 251 p.

SCHNEIDER C. (2000): Energy and mass balance at the surface in the wet snow zone of Northeast Glacier, Antarctic Peninsula. *Polarforschung* **67** (1/2), 65-75.

SHEPHERD A., D. WINGHAM, T. PAYNE and P. SKVARCA (2003): Larsen Ice Shelf Has Progressively Thinned. *Science* **302** (5646), 856-859.

SHI J. and J. DOZIER (1993): Measurements of snow - and glacier-covered areas with single-polarization SAR. *Annals of Glaciology* **17**, 72-76.

SIDJAK R. W. and R. D. WHEATE (1999): Glacier mapping of the Illecillewaet icefield, British Columbia, Canada, using, Landsat TM and digital elevation data. *International Journal of Remote Sensing* **20**, 273-284.

SIMÕES J.C., U. F. BREMER, F. E. AQUINO and F. A. FERRON (1999): Morphology and variations of glacial drainage basins in the King George Island ice field, Antarctica. *Annals of Glaciology* **29**, 220-224.

SINGH, P. and V. P. SINGH (2001): *Snow and glacier hydrology*. Water science and technology library 37, Kluwer Academic Publishers, 742 p.

SKVARCA P. (1993): Fast recession of the northern Larsen Ice Shelf monitored by space images. *Annals of Glaciology* **17**, 317-321.

SKVARCA P. and H. DE ANGELIS (2003): Impact assessment of regional climatic warming on glaciers and ice shelves of the northeastern Antarctic Peninsula. In DOMACK E., A. LEVENTER, A. BURNETT, R. BINDSCHADLER, P. CONVEY and M. KIRBY (eds.): *Antarctic Peninsula Climate Variability: Historical and Paleoenvironmental Perspectives*. Antarctic Research Series Volume 79,

American Geophysical Union, 69-78.

SKVARCA P., W. RACK, H. ROTT and T. IBARZÁBAL Y DONÁNGELO (1998): Evidence of recent climatic warming on the eastern Antarctic Peninsula. *Annals of Glaciology* **27**, 628-632.

SKVARCA P., W. RACK and H. ROTT (1999a): 34 year satellite time series to monitor characteristics, extent and dynamics of Larsen B Ice Shelf, Antarctic Peninsula. *Annals of Glaciology* **29**, 255-260.

SKVARCA P., W. RACK, H. ROTT and T. IBARZÁBAL Y DONÁNGELO (1999b): Climatic trend and the retreat and disintegration of ice shelves on the Antarctic Peninsula: an overview. *Polar Research* **18** (2), 151-157.

SKVARCA P., H. DE ANGELIS and E. ERMOLIN (2004): Mass balance of 'Glaciar Bahía del Diablo', Vega Island, Antarctic Peninsula. *Annals of Glaciology* **39**, 209-213.

SMITH L. C., R. R. FORSTER, B. L. ISACKS and D. K. HALL (1997): Seasonal climatic forcing of alpine glaciers revealed with orbital synthetic aperture radar. *Journal of Glaciology* **43** (145), 480-488.

STAMMERJOHN S. E. and R. C. SMITH (1997): Opposing southern ocean climate patterns as revealed by trends in regional sea ice coverage. *Climatic Change* **37**, 617-639.

STARK P. (1994): Climatic warming in the central Antarctic Peninsula area. *Weather* **49** (6), 215-220.

STEINER R. (2002): *Geometrische Terrainkorrektur satellitengestützter SAR-Szenen mit ERDAS Imagine 8.5*. Unpublished Diplom thesis (MSc. equivalent), Institut für Physiche Geographie - Albert-Ludwigs-Universität Freiburg, 100 p.

THOMPSON L. G., D. A. PEEL, E. MOSLEY-THOMPSON, R. MULVANEY, J. DAI, P. N. LIN, M. E. DAVIS and C. F. RAYMOND (1994): Climate since AD 1510 on Dyer Plateau, Antarctic Peninsula: evidence for recent climate change. *Annals of Glaciology* **20**, 420-426.

TORINESI O., M. FILY and C. GENTHON (2003): Interannual variability and trend of the Antarctic Ice Sheet summer melting period from 20 years of spaceborne

microwave data. *Journal of Climate* **16**, 1047-1060.

TURNER J., T. A. LACHLAN-COPE, J. P. THOMAS and S. R. COLWELL (1995): Synoptic origins of precipitation over the Antarctic Peninsula. *Antarctic Science* **7** (3), 327-337.

TURNER J., S. R. COLWELL and S. HARANGOZO (1997): Variability of precipitation over the coastal western Antarctic Peninsula from synoptic observations. *Journal of Geophysical Research* **102** (D12), 13999-14007.

TURNER J., S. LEONARD, T. A. LACHLAN-COPE and G. J. MARSHALL (1998): Understanding Antarctic Peninsula precipitation distribution and variability using a numerical weather prediction model. *Annals of Glaciology* **27**, 591-596.

TURNER J., T. A. LACHLAN-COPE, G. J. MARSHALL, E. M. MORRIS, R. MULVANEY and W. WINTER (2002): Spatial variability of Antarctic Peninsula net surface mass balance, *Journal of Geophysical Research* **107** (D13), 4173, doi:10.1029/2001JD000755.

TRYFOS P., (1996): *Sampling methods for applied research: test and cases*. John Wiley and Sons Inc., 440 p.

ULABY F. T., R. K. MOORE and A. K. FUNG (1986): *Microwave remote sensing: active and passive. Volume III: from theory to applications*. Artech House, Remote Sensing Series 4, 1120 p.

VAN DEN BROEKE M. (2005): Strong surface melting preceded collapse of Antarctic Peninsula ice shelf. *Geophysical Research Letters* **32**, L12815, doi:10.1029/2005GL023247.

VAN DER VEEN C. J. (2002): Calving glaciers. *Progress in Physical Geography* **26**, 96-122.

VAUGHAN D. G. (1992): The ice shelves of the Antarctic Peninsula: changing climate and sea level. In MORRIS E. M. (ed.): *The contribution of Antarctic Peninsula ice to sea level rise*. British Antarctic Survey Ice & Climate Special Report 1, 35-44.

VAUGHAN D. G. (2006): Recent trends in melting conditions on the Antarctic Peninsula and their implications for ice-sheet mass balance and sea level.

Arctic, Antarctic, and Alpine Research **38** (1): 147-152.

VAUGHAN D. G. and C. S. M. DOAKE (1996): Recent atmospheric warming and retreat of ice shelves on the Antarctic Peninsula. *Nature* **379** (6563), 328-331.

VAUGHAN D. G., G. J. MARSHALL, W. M. CONNOLLEY, C. PARKINSON, R. MULVANEY, D. A. HODGSON, J. C. KING, C. J. PULDSEY and J. TURNER (2003): Recent rapid regional climate warming on the Antarctic Peninsula. *Climatic Change* **60**, 243-274.

VERMOTE E., D. TANRÉ, J. L. DEUZÉ, M. HERMAN and J. J. MORCETTE (1997): Second simulation of the satellite signal in the solar spectrum, 6S: an overview, *IEEE Transactions on Geoscience and Remote Sensing* **35** (3), 675-686.

WARREN S.G. and W.J. WISCOMBE (1980): A model for the spectral albedo of snow. II. Snow containing atmospheric aerosols. *Journal of the Atmospheric Sciences* **37** (12), 2734-2745.

WILLIAMS R. S., D. K. HALL and C. S. BENSON (1991): Analysis of glacier facies using satellite techniques. *Journal of Glaciology* **37** (125),120-128.

WINTHER J.-G. and D. K. HALL (1999): Satellite-derived snow coverage related to hydropower production in Norway: present and future. *International Journal of Remote Sensing* **20** (15/16), 2991-3008.

WISCOMBE W. J. and S. G. WARREN (1980): A model for the spectral albedo of snow. I. Pure snow. *Journal of the Atmospheric Sciences* **37** (12), 2712-2733.

WUNDERLE S. (1996): Die Schneedeckendynamik der Antarktischen Halbinsel und ihre Erfassung mit aktiven und passiven Fernerkundungsverfahren. *Freiburger Geographische Hefte* **48**, 172 p.

ZENG Q., M. CAO, X. FENG, F. LIANG, X. CHEN and W. SHENG (1984): A study of spectral reflection characteristics for snow, ice and water in the north of China. In GOODISON B. E. (ed.): *Proceedings of Hydrological Aplications of Remote Sensing and Remote Data Transmission*. IAHS Publication No. 145, 451-462.

ZIBORDI G. and G. MARACCI (1993): Reflectance of Antarctic surfaces from multispectral radiometers: the correction of atmospheric effects. *Remote Sensing of Environment* **43**, 11-21.

ZWALLY H. J., J. C. COMISO, C. L. PARKINSON, D. J. CAVALIERI, and P. GLOERSEN (2002a): Variability of Antarctic sea ice 1979–1998. *Journal of Geophysical Research* **107** (C5), 3041, doi:10.1029/2000JC000733.

ZWALLY H. J., W. ABDALATI, T. HERRING, K. LARSON, J. SABA and K. STEFFEN (2002b): Surface melt-induced acceleration of Greenland ice-sheet flow. *Science* **297** (5579), 218-222.

Appendix

Table A.1: *SAR data used to test the texture and ISODATA approaches for classification of glacier frontal position.*

Platform/Sensor	Acquisition date	Track	Frame	Pass
ERS-1 AMI SAR	27 February 1994	18	5877	Ascending
ERS-2 AMI SAR	26 January 1997	381	4923	Descending
ERS-2 AMI SAR	30 January 1997	433	5859	Ascending
ERS-2 AMI SAR	17 February 1997	195	4923	Descending
ERS-2 AMI SAR	20 February 1997	476	5859	Ascending
ERS-2 AMI SAR	26 February 2000	476	4941	Descending
ERS-2 AMI SAR	26 February 2000	467	4959	Descending
ERS-2 AMI SAR	26 February 2000	467	4977	Descending
ERS-2 AMI SAR	26 February 2000	467	4995	Descending
ERS-2 AMI SAR	23 February 1997	276	5787	Ascending
ERS-1 AMI SAR	18 January 1995	1554	5769	Ascending
ERS-2 AMI SAR	23 February 1997	276	5769	Ascending
ERS-1 AMI SAR	18 July 1992	109	4905	Descending
ERS-1 AMI SAR	29 October 1996	109	4923	Descending
ERS-2 AMI SAR	17 November 1996	381	4923	Descending
ERS-2 AMI SAR	16 October 1996	424	4941	Descending
ERS-1 AMI SAR	15 October 1995	195	4923	Descending
ERS-1 AMI SAR	08 July 1992	467	4941	Descending
ERS-1 AMI SAR	08 July 1992	467	4959	Descending
ERS-1 AMI SAR	08 July 1992	467	4977	Descending
ERS-1 AMI SAR	08 July 1992	467	4995	Descending
ERS-1 AMI SAR	30 July 1992	281	4995	Descending
ERS-1 AMI SAR	19 August 1993	276	5787	Ascending
ERS-2 AMI SAR	27 June 1997	47	5769	Ascending
ERS-2 AMI SAR	07 November 1995	4	5769	Ascending
ERS-2 AMI SAR	04 November 1996	195	5031	Descending

Table A.2: *Optical data used to test the texture and ISODATA approaches for classification of glacier frontal position.*

Platform/Sensor	Acquisition date	Path	Row
Landsat TM	18 February 1986	220	107
Landsat TM	18 February 1986	220	108
Landsat TM	01 March 1986	217	106
Landsat TM	01 March 1986	217	107
Landsat TM	01 March 1986	217	108
Landsat TM	06 March 1986	220	108
Landsat TM	12 January 1988	215	107
Landsat TM	28 January 1988	215	108
Landsat TM	29 February 1988	215	105
Landsat TM	20 February 1989	218	109
Landsat TM	26 November 1989	219	105
Landsat TM	26 November 1989	219	106
Landsat ETM+	29 January 2000	215	104
Landsat ETM+	21 February 2000	216	105
Landsat ETM+	21 February 2000	216	106
Landsat ETM+	21 February 2001	218	105
Terra ASTER	29 December 2002	214	289
Terra ASTER	26 September 2001	217	288
Terra ASTER	26 September 2001	217	289
Terra ASTER	26 September 2001	217	290
Terra ASTER	20 October 2003	217	290
Terra ASTER	20 October 2003	217	289
Terra ASTER	20 October 2003	217	295
Terra ASTER	20 October 2003	217	296
Terra ASTER	20 October 2003	217	297
Terra ASTER	22 November 2001	216	290
Terra ASTER	22 November 2001	216	291
Terra ASTER	22 November 2001	216	292
Terra ASTER	22 November 2001	216	293
Terra ASTER	22 November 2001	216	294
Terra ASTER	22 November 2001	216	295
Terra ASTER	22 November 2001	216	296
Terra ASTER	22 November 2001	216	298
Terra ASTER	24 January 2003	220	291
Terra ASTER	24 January 2003	220	292
Terra ASTER	18 December 2002	217	294
Terra ASTER	18 December 2002	217	295

Terra ASTER	25 February 2001	214	296
Terra ASTER	25 February 2001	214	298
Terra ASTER	04 January 2001	218	293
Terra ASTER	04 January 2001	218	294
Terra ASTER	04 January 2001	218	295
Terra ASTER	04 January 2001	218	296
Terra ASTER	04 January 2001	218	297
Terra ASTER	13 October 2003	214	297
Terra ASTER	28 September 2001	215	296
Terra ASTER	25 December 2002	218	298
Terra ASTER	25 December 2002	218	299
Terra ASTER	25 December 2002	218	300
Terra ASTER	25 February 2001	214	298
Terra ASTER	05 October 2001	216	299
Terra ASTER	05 October 2001	216	300

Table A.3: *SAR data used for multi-temporal analysis of variations in glacier parameters.*

Platform/Sensor	Acquisition date	Track	Frame	Pass
ERS-2 AMI SAR	29 October 1996	109	4923	Descending
ERS-1 AMI SAR	13 February 1993	109	4923	Descending
ERS-2 AMI SAR	03 October 2000	109	4923	Descending
ERS-2 AMI SAR	15 October 2004	152	4923	Descending
ERS-2 AMI SAR	17 February 1997	195	4923	Descending
ERS-2 AMI SAR	04 November 1996	195	4923	Descending
ERS-1 AMI SAR	15 October 1995	195	4923	Descending
ERS-2 AMI SAR	26 January 1997	381	4923	Descending
ERS-2 AMI SAR	12 January 2005	424	4923	Descending
ERS-1 AMI SAR	05 July 1992	424	4923	Descending
ERS-2 AMI SAR	29 January 1997	424	4923	Descending
ERS-2 AMI SAR	15 October 2004	152	4941	Descending
ERS-2 AMI SAR	17 February 1997	195	4941	Descending
ERS-2 AMI SAR	06 October 2005	238	4941	Descending
ERS-1 AMI SAR	05 July 1992	424	4941	Descending
ERS-2 AMI SAR	23 February 2000	424	4941	Descending
ERS-2 AMI SAR	16 October 1996	424	4941	Descending
ERS-2 AMI SAR	29 January 1997	424	4941	Descending
ERS-2 AMI SAR	26 February 2000	467	4941	Descending
ERS-1 AMI SAR	08 July 1992	467	4941	Descending

ERS-2 AMI SAR	06 October 2005	238	4959	Descending
ERS-2 AMI SAR	16 October 1996	424	4959	Descending
ERS-2 AMI SAR	23 February 2002	424	4959	Descending
Envisat ASAR	06 July 2005	424	4959	Descending
ERS-1 AMI SAR	05 July 1992	424	4959	Descending
ERS-1 AMI SAR	08 July 1992	467	4959	Descending
ERS-2 AMI SAR	26 February 2000	467	4959	Descending
ERS-2 AMI SAR	19 October 1996	467	4959	Descending
ERS-1 AMI SAR	27 July 1992	238	4977	Descending
ERS-2 AMI SAR	06 October 2005	238	4977	Descending
ERS-2 AMI SAR	16 October 1996	424	4977	Descending
ERS-2 AMI SAR	23 February 2000	424	4977	Descending
ERS-1 AMI SAR	05 July 1992	424	4977	Descending
Envisat ASAR	03 November 2004	424	4977	Descending
ERS-2 AMI SAR	26 February 2000	467	4977	Descending
ERS-2 AMI SAR	19 October 1996	467	4977	Descending
ERS-1 AMI SAR	08 July 1992	467	4977	Descending
ERS-2 AMI SAR	06 October 2005	238	4995	Descending
ERS-1 AMI SAR	05 July 1992	424	4995	Descending
ERS-2 AMI SAR	16 October 1996	424	4995	Descending
ERS-2 AMI SAR	23 February 2000	424	4995	Descending
Envisat ASAR	03 November 2004	424	4995	Descending
ERS-1 AMI SAR	08 July 1992	467	4995	Descending
ERS-2 AMI SAR	19 October 1996	467	4995	Descending
ERS-2 AMI SAR	26 February 2000	467	4995	Descending
ERS-1 AMI SAR	24 July 1992	195	5013	Descending
ERS-2 AMI SAR	02 February 1998	195	5013	Descending
ERS-1 AMI SAR	15 October 1995	195	5013	Descending
ERS-2 AMI SAR	05 February 1998	238	5013	Descending
ERS-2 AMI SAR	07 March 1996	238	5013	Descending
ERS-1 AMI SAR	18 January 1993	238	5013	Descending
ERS-2 AMI SAR	06 October 2005	238	5013	Descending
ERS-2 AMI SAR	18 February 1998	424	5013	Descending
Envisat ASAR	03 November 2004	424	5013	Descending
ERS-1 AMI SAR	09 November 1999	424	5013	Descending
ERS-2 AMI SAR	26 February 2000	467	5013	Descending
ERS-2 AMI SAR	17 January 1998	467	5013	Descending
ERS-1 AMI SAR	03 February 1993	467	5013	Descending
ERS-2 AMI SAR	19 October 1996	467	5013	Descending
Envisat ASAR	03 August 2004	109	5031	Descending

ERS-2 AMI SAR	03 October 2000	109	5031	Descending
ERS-2 AMI SAR	31 January 2005	195	5031	Descending
ERS-1 AMI SAR	28 January 1996	195	5031	Descending
ERS-1 AMI SAR	09 November 1999	424	5031	Descending
ERS-2 AMI SAR	03 October 2000	109	5049	Descending
Envisat ASAR	03 August 2004	109	5049	Descending
ERS-2 AMI SAR	31 January 2005	195	5049	Descending
ERS-1 AMI SAR	24 July 1992	195	5049	Descending

Table A.4: *Optical data used for multi-temporal analysis of variations in glacier parameters.*

Platform/Sensor	Acquisition date	Path	Row
Landsat TM	01 March 1986	217	105
Landsat TM	28 January 1989	217	104
Landsat TM	12 January 1988	215	107
Landsat TM	28 January 1988	215	108
Landsat TM	26 November 1989	219	105
Landsat TM	26 November 1989	219	106
Landsat TM	01 March 1986	217	106
Landsat TM	01 March 1986	217	107
Landsat TM	01 March 1986	217	108
Landsat TM	18 February 1986	220	108
Landsat TM	18 February 1986	220	107
Landsat TM	20 February 1989	218	109
Landsat TM	29 February 1988	215	105